

UNIVERSITY OF NAPLES FEDERICO II

SCHOOL OF DOCTORATE IN INDUSTRIAL ENGINEERING



International PhD Program

NOVEL TECHNOLOGIES FOR MATERIALS, SENSORS AND
IMAGING

XXV Cycle

*Hybrid organic/inorganic nanostructured systems
obtained by self-assembly of block-copolymers*

by

Gianpaolo Chieffi

Supervisors:

Prof. Antonio Aronne

Prof. Claudio De Rosa

Coordinator:

Prof. Luciano Lanotte

Abstract

An amphiphilic polystyrene-*b*-poly(ethylene-oxide) (PS-*b*-PEO) diblock copolymer (BCP) was used as template for the incorporation of metal oxide nanoparticles, namely TiO₂ or Nb₂O₅ using the sol-gel method. This study was aimed to the preparation of neat BCP and hybrid thin films by spin-coating. The hydrophilic sol-gel precursor of the metal oxides was selectively incorporated into hydrophilic PEO domains of BCP organized in a hexagonal array of vertical cylinders embedded in the PS matrix. Removal of polymer matrix by heat-treatment produced a nearly periodic array of TiO₂ or Nb₂O₅ nanoparticles reminiscent of original hexagonal nanostructure.

A novel solvent annealing procedure was developed in order to improve the morphological order of the neat copolymer and of the hybrid materials.

BCP/TiO₂ hybrid and heat treated thin films were used as conductometric sensors to detect soot nanoparticles (PM 0.1 and 0.01).

Table of Contents

Table of contents	ii
1 Block copolymer and sol-gel technique for fabrication of hybrid nanocomposites	1
1.1 Block copolymers as templates for inorganic material patterning	1
1.2 Block copolymer architecture and general principles	3
1.3 Morphologies	5
1.4 Methodologies to align and orient on long-range scale the morphologies of block copolymers	8
1.4.1 Application of external fields	9
1.4.2 Use of template	12
1.4.3 Specific surface interactions	13
1.5 Applications of BCPs	15
1.5.1 Nanocomposites	19
1.6 The sol-gel technology	22
1.6.1 Sol-gel chemistry	23
1.7 Description of the thesis work	26
Bibliography of Chapter I	28
2 Materials and methods	35
Experimental part	35
2.1 Analyzed sample	35
2.2 Thermal and structural analysis	37
2.2.1 Thermal analysis	37
2.2.2 Wide angle X-ray scattering (WAXS)	38
2.2.3 Fourier transform infrared spectroscopy	38
2.3 Morphological analysis	39

2.3.1 Transmission electron microscopy (TEM)	39
2.3.2 Atomic Force Microscopy (AFM)	40
2.3.3 Scanning electron microscopy (SEM)	42
2.4 Thin film deposition technique: spin-coating	45
2.5 Profilometry	47
2.6 Preparation process of neat and hybrid materials	49
Bibliography of Chapter II	51
3 Ordering of nanostructured BCP based hybrid thin films over large areas	53
3.1 Characterization of the neat block copolymer (SEO)	53
3.1.1 Thermal analysis	53
3.1.2 Wide angle X-ray scattering (WAXS)	56
3.1.3 Morphological analysis of the neat SEO	58
3.2 Synthesis and characterization of TiO ₂	63
3.2.1 Applications of TiO ₂	63
3.2.2 The structure of TiO ₂ surfaces	66
3.2.3 Nanostructured TiO ₂	68
3.2.4 Synthesis and characterization of TiO ₂	70
3.2.5 Morphological analysis of TiO ₂ films obtained from TTIP solution	75
3.3 Hybrid materials	77
3.4 Heat-treated materials	83
3.5 PEO-TiO ₂ thin films materials	87
3.6 Adhesion tests of the heat-treated hybrid films	89
3.7 Solvent annealing: a methodology to improve on long range scale the cylindrical morphology of the neat SEO and of the hybrid materials	90
3.7.1 Solvent annealing on the neat SEO by exposure to solvent vapors in a closed vessel	94

3.7.2 Solvent annealing on the neat SEO and on the hybrid samples directly in the spin-coating chamber	95
3.7.3 A new tool for improving the lateral order of neat and hybrid materials: Rapid Solvent Annealing method	106
3.8 Preparation of hybrid and heat-treated thin films PS- <i>b</i> -PEO/Nb ₂ O ₅	111
Bibliography of Chapter III	119
4 BCP/TiO₂ hybrid and heat-treated materials as soot sensors	125
4.1 Conductivity for soot sensing	125
4.2 Conductometric soot sensor: experimental setup	128
4.2.1 Soot deposition	129
4.2.2 Electrical measurements	133
Bibliography of Chapter IV	141
5 Conclusions	143
Appendices	147

Acknowledgements

I più doverosi ringraziamenti vanno ai Prof. Antonio Aronne, alla Prof.ssa Finizia Auriemma, al Prof. Claudio De Rosa e al Prof. Pasquale Pernice per avermi continuamente supportato durante lo svolgimento di questo stimolante progetto interdisciplinare.

Vorrei ringraziare anche il Dr. Rocco Di Girolamo che ha seguito questo lavoro di ricerca e ha saputo consigliarmi egregiamente durante questo triennio, nonostante la distanza.

Non posso dimenticare il lavoro instancabile di Guido Celentano, persona squisita e sempre disponibile, grazie al quale i tediosi problemi burocratici venivano risolti in breve tempo.

Un grazie speciale va ad alcune persone che hanno fatto parte della mia esperienza di quasi un anno all'Università di Santiago de Compostela. Al Prof. Massimo Lazzari per la sua accoglienza e per avermi subito fatto integrare nel suo gruppo. Alla Dr. Marina Nieto Suárez per la sua disponibilità e per avermi fatto sentire a mio agio in un paese straniero. Sono stato fortunato ad aver conosciuto il Dr. Manuel Gómez García e aver condiviso con lui tante illuminanti chiacchierate scientifiche.

Ricordo con grande piacere le discussioni, i consigli, l'entusiasmo che mi hanno saputo trasmettere per tutto quello che fosse scienza. Grazie a loro ho capito ancor di più quanto sia fondamentale nella vita cercare di investire il proprio tempo abbinando la propria occupazione alle proprie inclinazioni d'animo.

Ringrazio il personale tecnico del CACTUS: Ramiro Barreiro Pérez, Mercedes Rivas Cascallar e Raquel Antón Segurado. La gran parte delle immagini di microscopia e quindi il cuore del mio lavoro di tesi è stato ottenuto lì con loro. Le tantissime ed estenuanti ma allo stesso tempo utili ore spese vicino agli strumenti si sono rivelate piacevoli grazie alla loro esperta compagnia.

Aver vissuto e lavorato così vicino alla "*fine della terra*" è stata una di quelle esperienze di vita che non baratterei mai per nulla al mondo.

Durante gli ultimi mesi di ricerca ho avuto il grande piacere di poter lavorare con la Dr. Carmela Bonavolontà e l'Ing. Mario Commodo. Grazie a loro ho potuto ampliare le mie conoscenze scientifiche e gli sono grato di avermi aiutato a non demordere quando i risultati tardavano ad arrivare. Oltre ai ringraziamenti "accademici" non posso dimenticare il contributo morale e affettivo delle persone che hanno accompagnato il mio percorso scientifico.

Vorrei ringraziare i miei genitori, tutta la mia famiglia e gli amici più cari. La sola consapevolezza dell'immensa fiducia che tutti loro hanno costantemente riposto in me ha alimentato il motore della mia passione, della mia dedizione e della voglia di fare sempre meglio.

Grazie a mio nonno e al suo esempio. Bastava una telefonata o più semplicemente un'occhiata per farmi ricordare quale fosse la mia strada.

Sono fiero di aver svolto questo dottorato nell'università statale più antica del mondo, in una cornice stupenda quale la città di Napoli. Sebbene la sua fama sia oggi vittima di pregiudizi ingenerosi rimarrà eternamente per me *alma mater* e motivo di orgoglio.

“ὁ τοίνυν κόσμος συνέστη περικεκλασμένωι σχήματι ἐσχηματισμένος τὸν τρόπον τοῦτον ἑ τῶν
ἀτόμων σωμάτων ἀπρονόητον καὶ **τυχαίαν** ἔχόντων τὴν κίνησιν συνεχῶς τε καὶ τάχιστα
κινουμένων, εἰς τὸ αὐτὸ πολλὰ σώματα συνηθροίσθη [καὶ] διὰ τοῦτο ποικιλίαν ἔχοντα καὶ
σχημάτων καὶ μεγεθῶν.”

Ὁ Λεύκιππος, Μέγας διάκοσμος, (5th cent. B.C.)

*“Sed ne mens ipsa necessum
intestinum habeat cunctis in rebus agendis
et devicta quasi cogatur ferre patique,
id facit exiguum **clinamen** principiorum
nec regione loci certa nec tempore certo.”*

Titus Lucretius Carus, *De rerum natura*, II, 216-224, 284-293, (1st cent. B.C.)

*“As part of the reality whose connections are expressed by quantum theory, the laws of
nature do not lead to a complete determination of what is happening in space and time, the
events are rather submitted to the **fate**.”*

Werner Heisenberg, *Über quantenmechanische Kinematik und Mechanik*, *Mathematische
Annalen*, (20th cent. A.C.)

CHAPTER I

Block copolymer and sol-gel technique for fabrication of hybrid nanocomposites

1.1 Block copolymers as templates for inorganic material patterning

At the present time, block-copolymer-based materials have attracted much attention in view of their potential applications, since the self-assembly capacity of this kind of materials with nanoscale periodicity allows the creation of nanopatterned structures. Several studies have reported the use of block-copolymers (BCPs) as templates for the synthesis of nanostructured materials because of their ability to control both the size and the spatial organization by varying their composition and molecular weight.

The main research activity of this PhD thesis was addressed to design a *sol-gel synthesis* (versatile and cheap) of hybrid organic/inorganic nanocomposites taking advantage of the *self-assembly* capability of the block copolymers in order to obtain a nanostructuring of the final material optimizing the long-range order at micrometric scale.

This first chapter is focused and highlights the strengths and the potential of these two key points:

- ❖ The ordering of *block copolymers* in thin films, the methodologies involved in the improvement of their orientation on long-range scale and the emerging potential applications.
- ❖ The reactions and the chemistry behind the *sol-gel technique* and its advantages: the low process temperature, the high control of purity, composition, microstructure and textural properties of the final material.

In the recent literature many examples concerning the preparation of hybrid and inorganic nanostructured materials using BCPs as template are present.

Gold nanoparticles prepared by reduction of gold salt precursors selectively form within the poly (4-vinylpyridine) (P4VP) lamellae of a PS–P4VP diblock film (with PS = polystyrene), leading to a lamellar morphology with lamellae oriented parallel to the substrate,¹ and selective inclusion of Au nanoparticles inside P4VP domains. In a similar way, a palladium salt precursor was selectively reduced within PS lamellae to produce Pd nanoparticles.² In a

PS–PIOH [poly(styrene-*block*-hydroxylated isoprene)] film with PIOH forming spheres in the PS matrix, Pd or Co nanoparticles formed in the PIOH domains.² Block copolymer nanostructures can also be used to template the patterning of pre-formed gold nanoparticles.^{3,4} Passivated gold or palladium nanoparticles were shown to selectively decorate PS domains in a stripe pattern formed by an asymmetric PS–PMMA diblock copolymer.^{3,4} In the case of the palladium nanoparticles, electroless plating of copper was subsequently performed, to produce semicontinuous copper nanostructures.⁴ The approach has been extended to pattern terpyridine-functionalized gold nanoparticles, followed by cross-linking with iron ions to create nanoparticles arranged according to the nanostructured stripe or dot pattern block copolymer template.⁵ It has also been observed that selective decoration can be achieved using evaporated metals (in which case nanoparticles form by aggregation in the polymer).⁶⁻⁹ Examples of nanoparticle patterning⁸ at the surface of a diblock copolymer via this route are illustrated in Figure 1.1 that shows TEM images of gold at the surface of a PS–PMMA diblock.

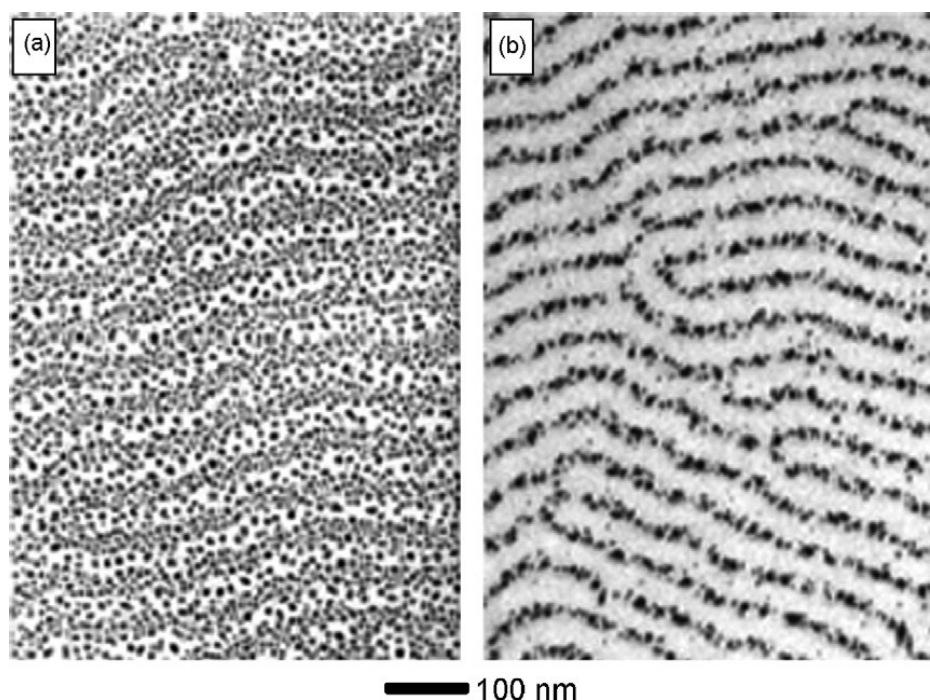


Figure 1.1: Examples of gold nanoparticle arrays templated by a stripe pattern formed at the surface of a polystyrene–poly(methyl methacrylate) diblock copolymer by vapor deposition of gold. The gold selectively wets polystyrene domains.⁸

Part (a) of Figure 1.1 was obtained directly after evaporation of 30Å of gold. Figure 1.1b shows the improvement in selectivity that can be obtained by additional annealing (180 °C, 1min).

Mesoporous silica and titania have been templated using thin films of PS–P2VP diblocks forming PS cylinders.¹⁰ The P2VP domains were chemically cross-linked and then swollen with silica or titania precursors for sol–gel synthesis. The PS cylinders were then oxidised to remove the block copolymer template, generating mesoporous materials.

The sol-gel method that has been one of the fundamental key-points in this PhD thesis (the chemistry of the process is described in Paragraph 1.6) is widely employed as one of the simplest fabrication protocol for synthesizing nanoparticles with well-defined sizes. However, all parameters must be strictly controlled, since a small change in one of the parameters, such as temperature, reaction time, or concentration, can significantly influence the results.¹¹

1.2 Block copolymer architecture and general principles

In the last decades block copolymers have generated a huge interest in the field of nanotechnologies¹²⁻²⁹ thanks to their capability to form by self-assembly structures with periodicity at nanometric scale. These are polymeric materials where macromolecules of two or more different homopolymers are chemically linked between them to form complex macromolecules with linear architecture (di-, tri-, multiblock copolymers) or not linear (*mixed arm, starblock, o graft copolymers*) (Figure 1.2).

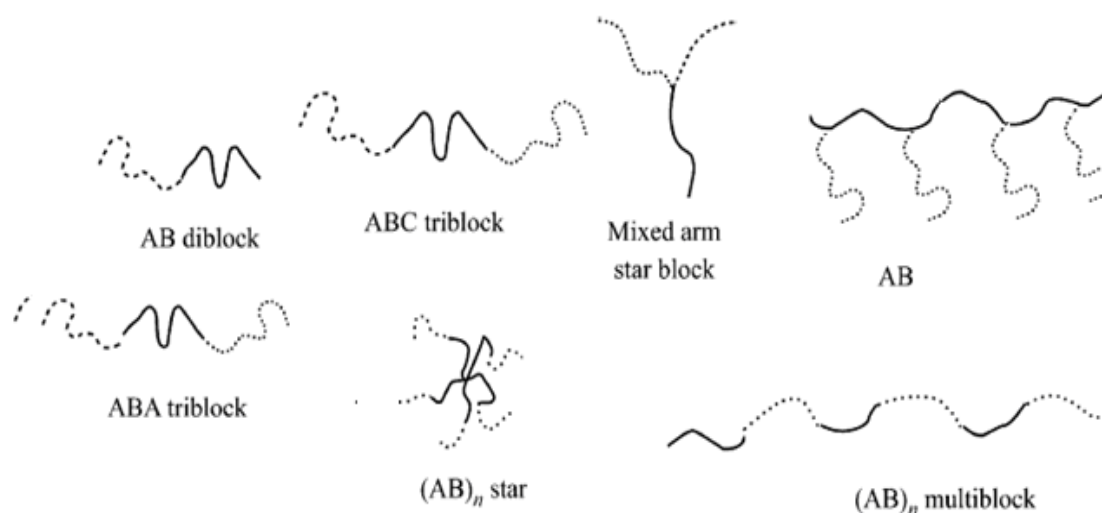


Figure 1.2: Linear or not linear architectures of block copolymers.

If different polymeric blocks are chemically incompatible, phase separation with spontaneous segregation of different macromolecules in diverse microdomains (Figure 1.3) is obtained. The formed microdomains are not arranged in a random manner. They are arranged according to regular disposition giving rise to the formation of periodical structures.

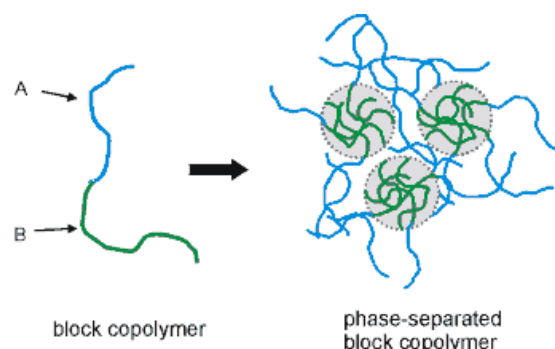


Figure 1.3: “*Self-assembly*” scheme in BCPs due to phase separation.

This “*self-assembly*” phenomenon determines the spontaneous formation of nanostructures³⁰ and is associated to the competition between the tendency to phase separation, due to blocks incompatibility, and the chemical connectivity; periodical structures are formed as a result of the need to minimize the contact area between incompatible microdomains that results minimized. The minimization of area at the interfacial region between the domains entails an interfacial energy diminution so that even if from an entropic point of view the individual polymeric chains prefer a *random-coil* conformation, in the case of block copolymers, the macromolecules tend to assume more extended conformations at the interface between the blocks in order to permit to the similar blocks to organize themselves in microstructures that minimize the ratio (exposed surface)/(volume).³¹

The periodicity and the dimensions of such regular domains depends from the length of the blocks and therefore from the molecular masses.

1.3 Morphologies

Different morphologies are achieved depending on the chemical nature of the blocks and their relative molecular masses. The fundamental variables that define the type of nanostructure formed by *self-assembly* are the Flory-Huggins interaction parameter χ representing the degree of incompatibility of the blocks, and the volume fraction of the blocks ϕ , depending from the relative length of the blocks.³¹ In Figure 1.4 the classical microstructures found for di- and tri- block copolymers are reported.^{12,31}

For di-block copolymers the component with the lowest molecular mass is separated creating spheres (see Figure 1.4a) when its volume fraction is lower than 20% and cylinders for values of volume fraction comprised between 21 and 33%. Alternating lamellar structures are obtained for symmetrical blocks copolymers with similar molecular masses and with a volume fraction around 50%. Additionally structures with a bicontinuous network (*double gyroid* and *double diamond*) are achieved in a narrow range of composition (volume fraction between 33 and 37%).^{12,31}

For tri-block copolymers the combination of different sequences ABC, ACB, BAC, of overall composition and molecular mass provides an enormous quantity of parameters that permits the creation of new morphologies (Figure 1.4 b). The most interesting feature of these systems is that the spontaneously created self-assembled microdomains packed themselves in ordered structures reminiscent of those ones of the crystalline materials. The spheres are packed in body centered-cubic structures and the cylinders in hexagonal lattice.

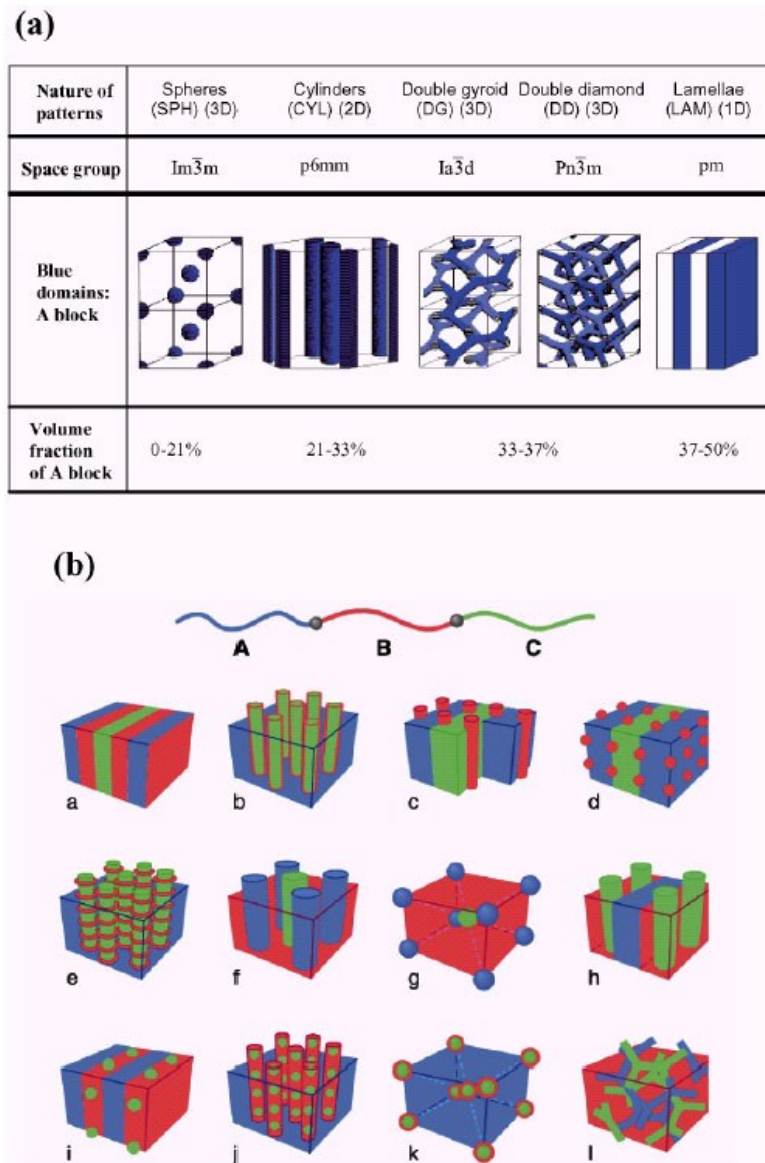


Figure 1.4: Microstructures generated by *self-assembly* in di-block copolymers AB (a) and tri-blocks ABC (b) as a function of the volume fraction of the minority component.

From this point of view block copolymers represent a class of amorphous materials able to organize themselves in similar structures of those of crystalline materials, with the strong difference that the dimensions of the repetitive units and the periodicity are not of the order of angstrom, as in the crystals, but of nanometers. The dimensions of the microdomains where polymeric blocks are segregated (spheres, cylinders and lamellae) and also the periodicity of the microstructure depend from the length of the blocks and consequently form the molecular masses of the blocks. This fact permits tuning the dimensions of microdomains and the periodicity in a wide range, from tens to hundreds nanometers, adjusting the molecular masses of the blocks.

It is important to underline that when temperature changes it is possible to observe either transitions from one nanostructure to another (order-order transition), or transition from an ordered nanostructured state to a disordered one (order-disorder transition).^{12,31,32} The temperature at which the transition from an ordered structure to a disordered one is called ODT (*Order Disorder Temperature*).³³

These last comments can be better understood referring to the phase diagram of block copolymers that, as the common diagram of low molecular mass molecules, identify the regions of stability of the different phases. In these diagrams the product χN is reported (where N is the sum of the molecular weights of the individual polymeric blocks of the copolymer) in function of the volume fraction ϕ (symbolized as f). The dependence of the different nanostructured phases from the temperature is intrinsically contained in the χ parameter that depends from T according to a law of inverse proportionality.³³

As an example in Figure 1.5 the phase diagram of the block copolymer poly(isoprene-*b*-polystyrene) (PI-*b*-PS)³³ is reported. A first transition order-order of the component of lower molecular mass is observed, from a cylindrical nanostructure to a bicontinuous nanostructure with the increase of temperature and so with a diminution of χN , for values of f_{PI} of 0.38. Successively an order-disorder transition is experienced from an ordered bicontinuous nanostructure to a system where blocks are completely miscible.

Block copolymers found their application, nowadays considered classical, as thermoplastic elastomer. Only recently they aroused great interest in the field of nanotechnologies.^{12-15,34} In fact, the possibility to manipulate, by chemical synthesis, the molecular architecture and the molecular weights of the blocks, makes these systems an ideal tool to design nanostructures for specific applications, as the creation of ordered patterns on the thin films surface, of great interest for the electronic and optoelectronic industries.

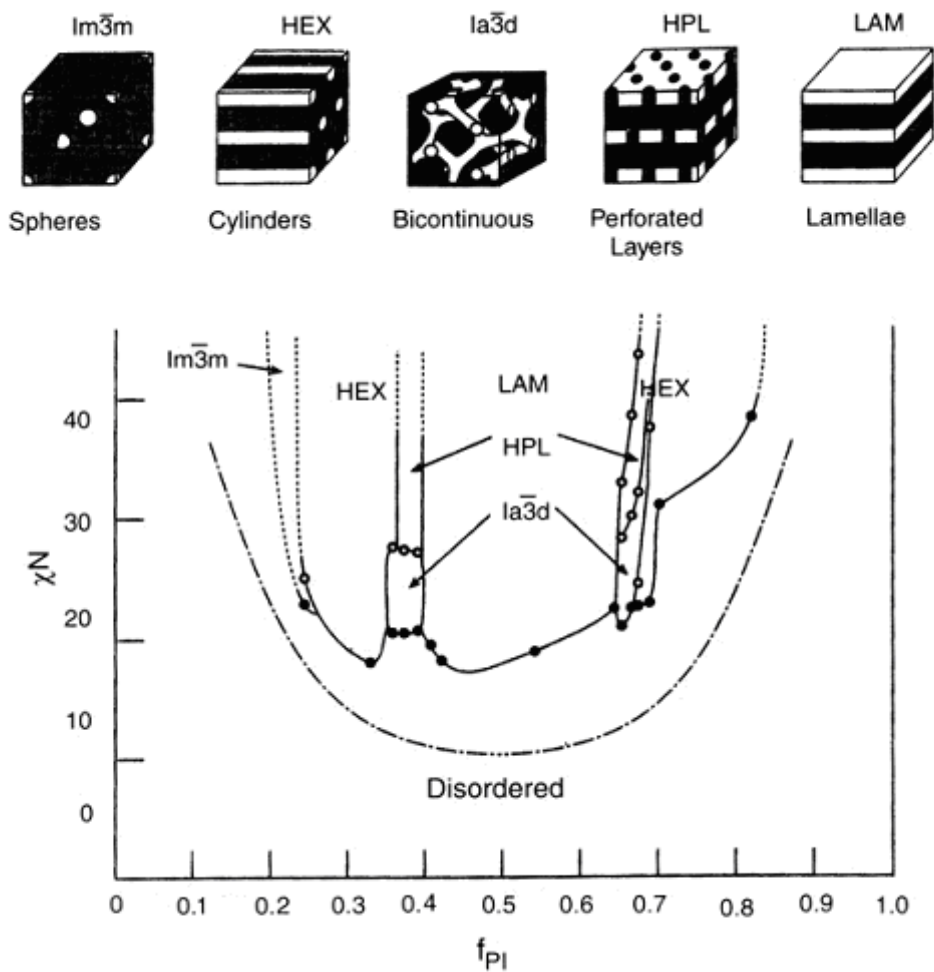


Figure 1.5: Phase diagram of PI-*b*-PS block copolymer.

The molecular architectures that could be developed by the classical anionic polymerization procedures vary from the linear di-block,³⁵ to the linear tri- or multi-block,³⁵ to more complex geometries as the star nanostructure.³⁶ All these geometries permit to create patterns on the thin films surface hardly practicable with the traditional lithography techniques.

1.4 Methodologies to align and orient on long-range scale the morphologies of block copolymers

The development of BCPs requires the preparation of thin films with thicknesses ranging from a few tens of nanometers (in some cases down to thicknesses of less than the corresponding equilibrium period of the BCP) to several micrometers.

Films with low surface roughness may be produced by spin-coating or dip-coating from relatively dilute solutions, i. e., approximately 1–5% by weight, onto solid substrates with uniform flatness.

In thin films the self-assembled BCPs morphologies are influenced not only by molecular weights, polydispersity and composition but also by other variables such as the selectivity of the solvent for one block, surface–interfacial interactions and the interplay between structure periodicity and film thickness, which can cause significant deviations from the predicted phases in the bulk state.

Independently of the casting techniques, even for a film prepared taking all the precautions, it is not possible to obtain a perfectly ordered morphology over a large area. In order to achieve orientation and periodic nanostructured order over macroscopic area an optimization of the preparation method is necessary. As discussed below, the optimization process can be carried out using different strategies.³⁷

1.4.1 Application of external fields

Since the first macroscopic alignment of cylindrical domains of an industrial tri-block copolymer (a PS-*b*-PB-*b*-PS, Kraton 102, with PB = polybutadiene) by extrusion carried out by the Keller group in the early 1970s,^{38,39} several mechanical flow fields have been proposed to control BCP alignment even though the success of these attempts was limited. In the 1990s research interests returned massively toward alignment strategies of BCP nanostructures by identification of weak external fields due the increased availability of BCPs with different architectures and chemical compositions. Particularly in recent years, most investigations moved from bulk materials to thin films, due to their nanotechnological potential, with a special focus on the use of electric fields.

The principal techniques that have been employed to control the BCP long-range order are:

- ❖ **Mechanical flow fields** as extrusion,^{38,39} compression,⁴⁰⁻⁴³ flows involving oscillatory shear⁴⁴⁻⁵⁴ and other steady shear techniques,⁵⁵⁻⁵⁸ up to techniques that combine different flow fields⁵⁹⁻⁶³ have been successfully applied to induce alignment in BCPs.

❖ **Static electric fields** have been widely used in copolymer melts to macroscopically orient lamellar or cylindrical morphologies,⁶⁴⁻⁷¹ with most of the investigations being focused on PS-*b*-PMMA (with PMMA = polymethylmethacrylate) (see Figure 1.6). Morphologies parallel to the substrate can be obtained using an in-plane field. A uniaxial orientation along the field and perpendicular to the substrate is instead induced with the BCP sandwiched between the electrodes. As initially proposed by Russell and coworkers, a convenient procedure consists in the preparation of films between two Kapton sheets coated on one side with Al, with the film thickness controlled through Kapton spacers. Kapton is a commercially available polyimide with excellent mechanical properties that allows further manipulation after alignment of the domains⁷² and facilitates sample characterization, such as for microtoming.

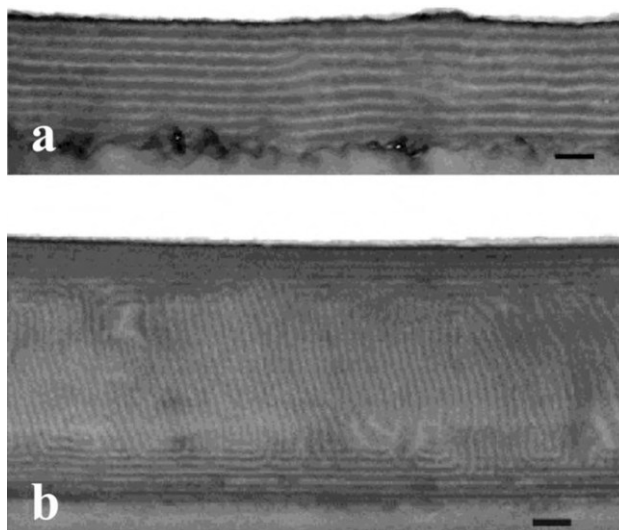


Figure 1.6: Cross-sectional TEM of ≈ 300 nm (a) and ≈ 700 nm (b) symmetric PS-*b*-PMMA films between Kapton electrodes annealed at 170 °C under ≈ 40 V μm^{-1} electric field for 6 and 16 h, respectively. The scale bar represents 100 nm (reproduced from Xu et al.)⁶⁹

❖ A further alignment approach is available for materials that exhibit anisotropic susceptibility due to an anisotropic molecular structure. **Magnetic field** induced orientation has been achieved for liquid crystalline diblock copolymers with a dielectric diamagnetic isotropy, possibly through the magnetic alignment of LC mesogens^{73,74} and also for BCPs with a crystallizable block through an accurate control of the crystallization process.⁷⁵ Magnetic fields also offer the ability to apply

very high fields without the risks of electric fields, associated with the danger and limit of electric breakdown.

- ❖ The observation of lamellar and cylindrical microdomains in thin films perpendicular to the surface as a result of **solvent evaporation** was first reported by Turturro and coworkers⁷⁶ and then investigated in more detail by Kim and Libera for a similar triblock copolymer.^{77,78} On the basis of these and other studies on either spun-cast or solution-cast films from solutions in a good solvent for all the blocks, a reasonable mechanism of orientation was proposed (Figure. 1.7). At the beginning of film deposition the T_g of the swollen film is still well below room temperature, thus allowing free chain mobility. With the decrease in the solvent concentration, the BCP undergoes a transition from the disordered to the ordered state and, as the diffusion of the solvent produces a gradient of concentration along the thickness of the thin film, the ordering front rapidly propagates from the air surface to the substrate. The consequent decrease of T_g below room temperature, for at least one block, locks in the structures, which, due to the high directionality of the solvent gradient, are highly oriented normal to the surface. This behavior has been reported so far for films with thickness less than one-half micron, as for instance in the case of PS-PB systems,^{76,79} polystyrene-*block*-poly(ethylene oxide) (PS-*b*-PEO)^{80,81} polystyrene-*b*-polyferrocenyldimethylsilane (PS-*b*-PFS).⁸² However this mechanism holds to any BCPs having the T_g of one block above room temperature.

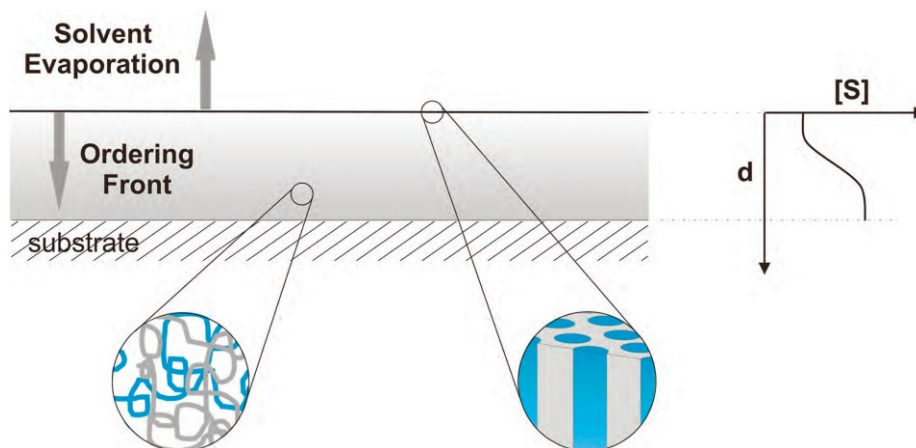


Figure 1.7: Schematic of the solvent evaporation in a diblock copolymer thin film.⁷⁹ The diffusion produces a gradient in the concentration of the solvent, [S], as a function of depth, d, which induces an ordering front from the film surface to the substrate.

1.4.2 Use of template

The combination of top-down strategies to fabricate patterns that direct the bottom-up organization of organic or inorganic building blocks is an approach often used in the micrometer and, to a minor extent, in the nanometer regime. Also, in the case of BCPs, the long-range order and orientation may be induced if self-assembly is forced to occur into/onto a guide, either topographically or chemically patterned, or in other 2D- or 3D-confinements. An innovative fabrication strategy that employs advanced lithographic techniques has been developed, by Nealey and coworkers, to produce perfect periodic domain ordering.^{83,84} As reported in Figure 1.8, in the first fundamental step of this procedure a self-assembled monolayer (SAM) is precisely patterned throughout the photoresist using extreme ultraviolet interferometric lithography.^{85,86} Following the conversion of the topographic pattern to a chemical pattern and the photoresist removal, a symmetric PS-*b*-PMMA is spin-coated onto the chemically patterned substrate and, as the modified regions present polar groups that preferentially wet the PMMA block, the self-assembly results in lamellae oriented perpendicular to the substrate.

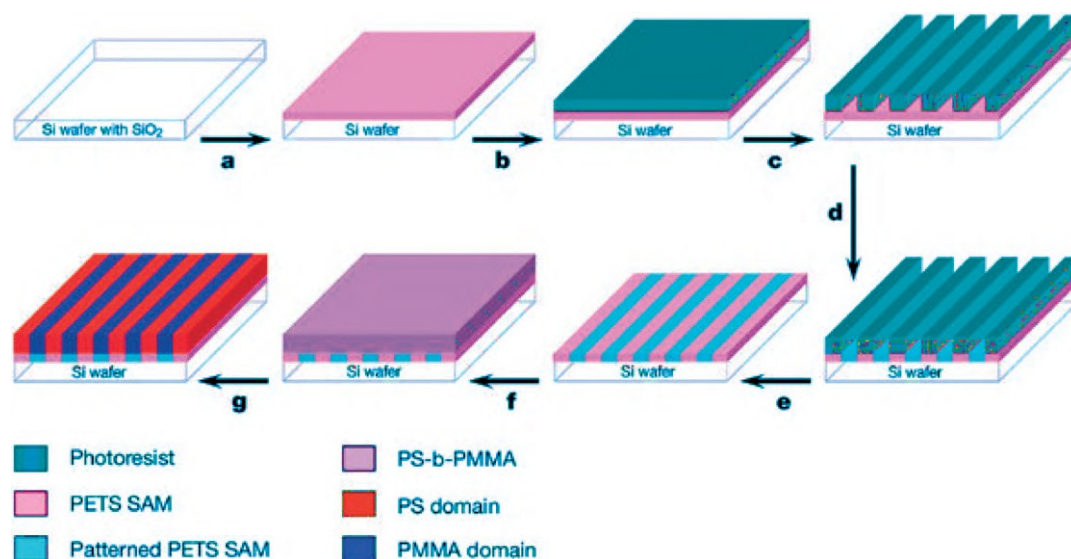


Figure 1.8: Schematic representation of the fabrication process of chemically nanopatterned surfaces that template the self-assembly of symmetric PS-*b*-PMMA ($M_n = 104\,000$). SAM of phenylethyltrichlorosilane is deposited onto a silicon wafer (a). Photoresist is then spin-coated (b) and patterned with alternating stripes and spaces by ultraviolet interferometric lithography (c). The topographic pattern is converted into a chemical pattern by irradiation with soft X-rays in the presence of oxygen (d). After the photoresist removal (e), a toluene solution of PS-*b*-PMMA is spin-coated onto the patterned SAM (f). Thermal annealing (g) facilitated surface-directed self-assembly.

1.4.3 Specific surface interactions

The control of the orientation of the microdomains in the microstructure of the BCPs can be obtained through a bias field induced by surface interactions. Different types of interactions can be established depending on the nature of the surface and of the BCP.

- ❖ The simplest interaction of a BCP film deposited on a substrate is the **preferential wetting** of one block at an interface to minimize interfacial and surface energies. As a consequence, a parallel orientation of microdomains, lamellae and cylinders is often induced at the interface and this orientation tends to propagate throughout the entire film.^{24,87-98} The microstructure can be altered by variation of the film thickness on the substrate and preferential interactions of blocks with the substrate.^{96,97} Symmetric boundary conditions are established when one of the blocks preferentially interacts with both the substrate and the air surface,⁹¹ while asymmetric conditions pertain when one block is preferentially wetted by the substrate and the other block by the superstrate.
- ❖ **Epitaxy** is defined as the oriented growth of a crystal on the surface of a crystal of another substance (the substrate). The growth of the crystals occurs in one or more strictly defined crystallographic orientations defined by the crystal lattice of the crystalline substrate.⁹⁹⁻¹⁰¹ The resulting mutual orientation is due to a 2D or, less frequently, a 1D-structural analogy, with the lattice matching in the plane of contact of the two species.⁹⁹ The term epitaxy, literally meaning “on surface arrangement”, was introduced in the early theory of organized crystal growth based on structural matching. Discrepancy between atomic or molecular spacings is measured by the quantity $100(d - d_0)/d_0$, where d and d_0 are the lattice periodicities of the adsorbed phase and the substrate, respectively. In general 10–15% discrepancies are considered as an upper limit for epitaxy to occur in polymers.¹⁰¹ Inorganic substrates were first used for the epitaxial crystallization of polymers.^{102,103} Successive studies have demonstrated the epitaxial crystallizations of polyethylene (PE) and linear polyesters onto crystals of organic substrates, such as condensed aromatic hydrocarbons (naphthalene, anthracene, phenanthrene, etc.), linear polyphenyls and aromatic carboxylic acids.^{104,105} In the case of PE, a unique orientation of the crystals grown on all the substrates is observed, with different contact planes depending on the substrate.¹⁰⁶ An example of an epitaxial relationship between PE crystals and an

organic substrate is shown in Figure 1.9, with the substrate constituted by a crystal of benzoic acid¹⁰⁷ (monoclinic structure with $a = 5.52 \text{ \AA}$, $b = 5.14 \text{ \AA}$, $c = 21.9 \text{ \AA}$ and $\beta = 97^\circ$, with a melting temperature of $123 \text{ }^\circ\text{C}$). A clear match between the PE interchain distance (the b -axis of PE equal to 4.95 \AA) and the b -axis periodicity of benzoic acid crystal (5.14 \AA), and between the c -axis periodicity of PE (2.5 \AA) and the a -axis of benzoic acid crystal (5.52 \AA), produces the crystallization of PE onto preformed crystals of benzoic acid with lamellae standing edge-on, that is, normal to the surface of benzoic acid crystal. The PE polymer chains lie flat on the substrate surface with their chain axis parallel to the substrate surface and parallel to the a -axis of benzoic acid crystal, and the b -axis of PE parallel to the b -axis of BA crystal.¹⁰⁷ The (100) plane of PE is in contact with the (001) exposed face of benzoic acid.

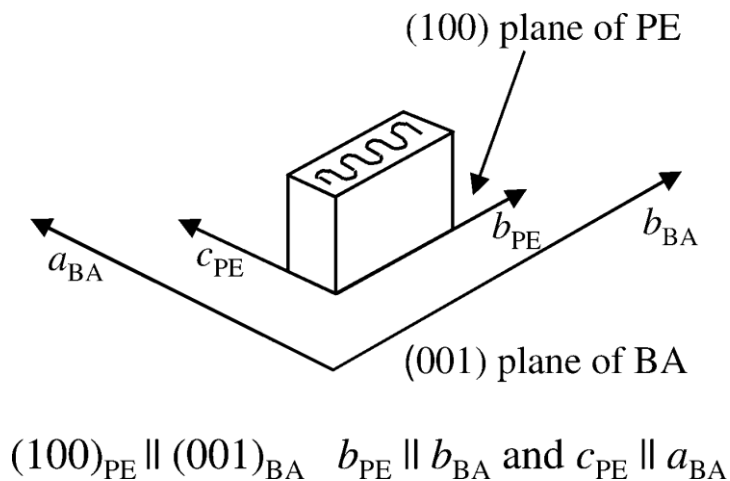


Figure 1.9: PE lamella oriented edge-on on the (001) face of a BA crystal substrate after epitaxial crystallization. The (100) plane of PE is in contact with the (001) plane of BA, and b - and c -axes of PE are parallel to b and a -axes of BA, respectively.

Epitaxy carries out an industrial relevance because works as basis of the nucleating activity for many nucleating and clarifying agents. It is also an ideal tool to design thin films with long-range order as for optoelectronic devices.¹⁰⁸

- ❖ **Directional solidification.** In many cases substrates can be melted and act as solvents for the polymer but only in their melt state. In this case, a small quantity of the substrate is melt together with the polymeric film between two glass slides (preferably two thin ones to minimize the thermal inertia during quenching). During the

quenching, substrate crystallizes at first, then the polymer crystallizes on the substrate surface. This process is observed frequently when the polymer and the substrate have similar melting temperature, and form an eutectic.¹⁰⁹ The possible epitaxial crystallization of the polymer brings a further specificity to the entire process.¹⁰⁸

- ❖ **Graphoepitaxy** is a process whereby an artificial surface topography of a crystalline or amorphous substrate influences and controls the orientation of the crystal growth in thin films.¹¹⁰⁻¹¹³ Graphoepitaxy has been used, often in combination with epitaxy, to obtain high orientation of polymeric crystals onto substrates constituted by films of other polymers.¹¹⁴⁻¹¹⁸

1.5 Applications of BCPs

Self-assembly of block copolymers into highly regular morphologies has been investigated by chemists for several decades but it is only in the last twenty years that multidisciplinary groups have focused their research efforts on the use of BCPs as a tool for nanomaterial fabrication, following a wider scientific and technological trend towards miniaturization. It has been discussed above that relatively simple processing of self-assembled BCPs in bulk or in solution permits the creation of individual polymeric nano-objects with different shapes, such as spheres, hollow spheres, fibers, and tubes. A better tailoring of intrinsic properties and control of dimensions of such objects, as well as optimization of fabrication methods currently available do not appear too difficult challenges. However their use for practical applications, as chemical or biological sensors or for encapsulation purposes, e.g., as carriers, is possibly hindered by the limited efforts so far focused on the development of efficient and reliable fractionation techniques.¹¹⁹⁻¹²⁰ Moreover, a tremendous, almost unexplored potential is likely to reside in the development of processes based on the controlled pyrolysis of polymeric nano-objects, as well as of self-assembled BCP film as whole,¹²¹ to yield nanostructured carbons.

Many polymer systems have been successfully employed as templates for nanofabrication. BCPs systems are polymeric materials that play a crucial role, because of the variety of tunable matrices at nanoscale level that they offer. Sophisticated procedures using 2D-ordered morphologies from di-block copolymer films have been employed to achieve at continuous arrays of metallic or semiconducting objects. These processes often imply the eventual

removal of one of the blocks, and use the film as a mask for subsequent deposition steps, or etching through the film, to transfer the BCP motif pattern to a substrate. As shown by Park et al., it is possible to use thin film of a block copolymer (polystyrene-*b*-polybutadiene) as a mask to transfer patterns on a semiconductive substrate.^{122,123} In Figure 1.10 the step of this process are schematically reported.

A nanostructured thin film of controlled thickness is deposited on a silicon nitride substrate that can be used as a positive mask removing the minority block of polybutadiene by selective ozonation. Otherwise using a not selective physical method (CF_4) it is possible to realize a pattern constituted from holes embedded on the substrate of the semiconductor. A negative mask can be realized using the same block copolymer that generates ordered points rather than holes. In this case the minority block is treated with osmium tetroxide (OsO_4) in order to slow down the etching rate changing the process selectivity.

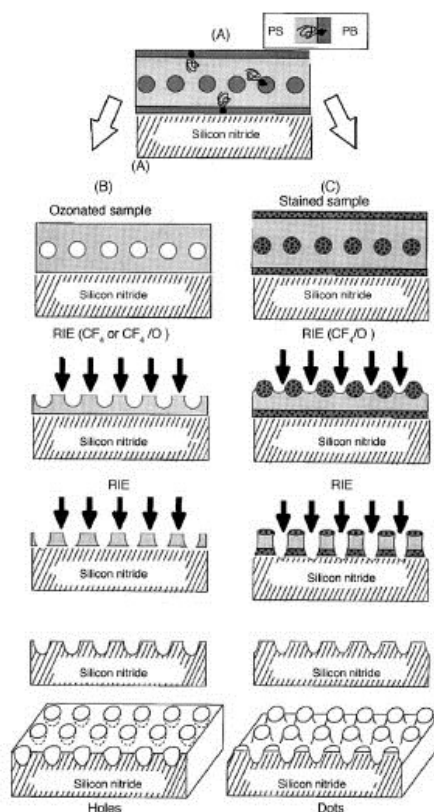


Figure 1.10: Fabrication process of silicon nitride dots (C) and holes (B) arrays via a nanolithography template consisting of a uniform monolayer of hexagonally ordered PB spheres in a PS matrix (cross-sectional view in A). PB wets the interfaces with the air and the silicon nitride substrate due to preferential interactions.

Block copolymer have been used recently to develop periodical structure in order to realize photonic band-gap materials.¹²⁴⁻¹³⁴

In a photonic crystal a periodic series of dielectrics with different refraction indexes, or eventually of a medium alternated with the vacuum, produces the formation of a photonic energy-gap: photons with energy values inner to the forbidden gap will be not able to pass through the crystal and will be reflected or confined over there. The effect is evident as much as the difference between the refraction indexes results substantial. Photonic crystals could have numerous application as: dichroic filters, laser diodes, high quality mirrors etc..

The first example of photonic crystal realized employing block copolymers was of one-dimensional type and has been realized using a thin film of block copolymer with a lamellar morphology (Figure 1.11a).¹²⁴⁻¹²⁶

The ordered lamellar structure was formed spontaneously thanks to the separation phase process and the optical properties reported in Figure 1.11b show a remarkable variation of the reflectance.

Photonic crystals realized using block copolymers generally present a small difference of dielectric contrast between the two phases. Realizing hybrid nanocomposites it is possible tuning the dielectric constant of one of the phases by selective inclusion of metallic nanoparticles in a targeted block.¹²⁸

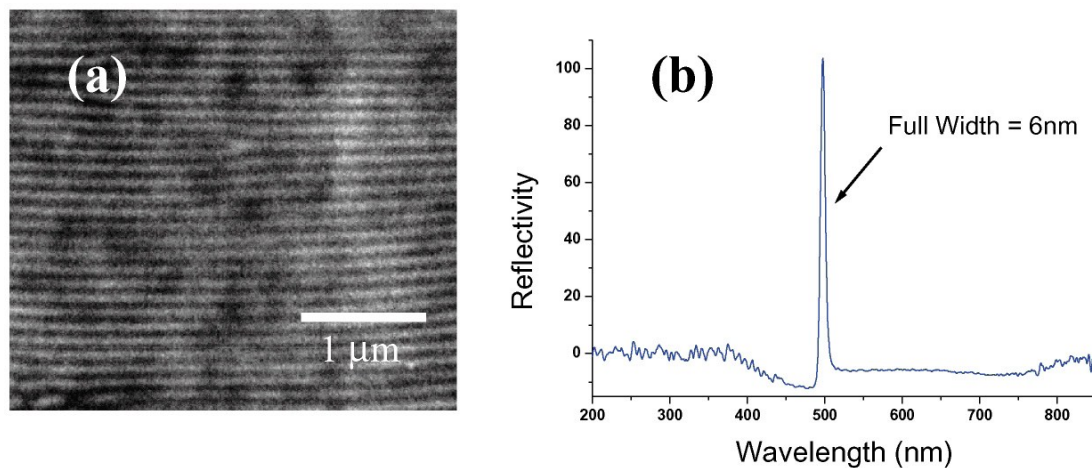


Figure 1.11: (a) SEM micrograph of a lamellar morphology obtained from a poly(styrene-*b*-isoprene) block copolymer treated with OsO₄.¹²⁷ (b) Reflectance spectrum characterized by a 6 nm large peak indicating a low dielectric contrast between the two phases.

Hashimoto et al.¹³⁵ showed that it is possible to employ block copolymers as precursors for the fabrication of nanostructured networks and membranes. The employed nanostructured

matrix has been realized from a blend constituted by a poly(styrene-*b*-isoprene) BCP and an homopolymer (polystyrene). The role of the homopolymer was of tuning the volume fraction of polystyrene, thus obtaining the desired microstructure. After the achievement of the nanostructure the domains of polyisoprene were removed by ozonolysis to reach a structure formed from nanochannels (Figure 1.12). Afterwards the surface of the nanochannels was covered by nickel enabling the employment of this material in the field of catalysis.

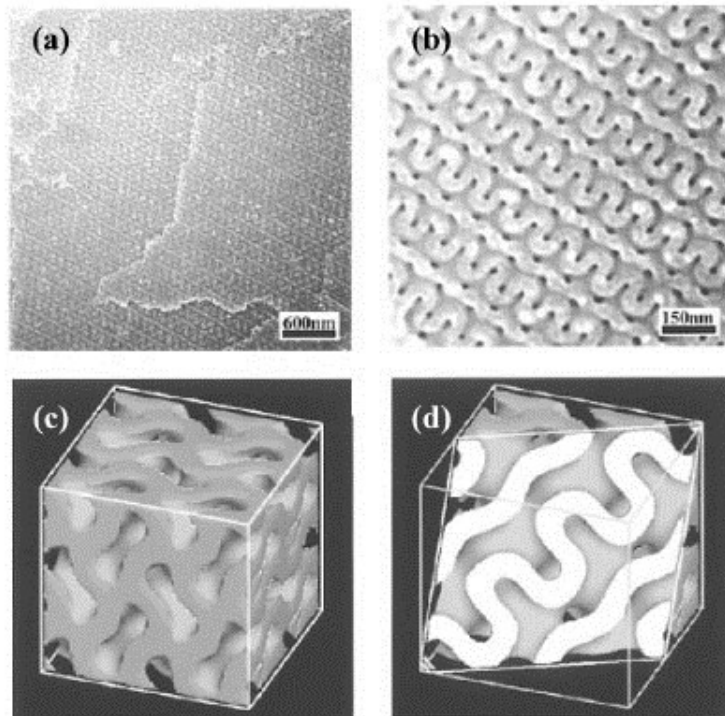


Figure 1.12: SEM micrographs showing bicontinuous nanochannels of polyisoprene in a matrix of polystyrene at different magnification (a) and (b). In (c) and (d) are reported the three-dimensional reconstructions of the matrix.

Besides the applications in the field of catalysis block copolymers can be used as membranes. At the present time this typology of membranes is produced for track-etching of polymeric films¹³⁶ and is characterized by a low density of nanopores packed in irregular structures. Using a block copolymer cylindrical morphology ordered in a hexagonal lattice, it is possible to obtain membranes with an high density of nanopores through the selective removal of the minority block. The advantage of this approach derives from the ultrafiltration conducted at higher rates. For example membranes with nanochannels regularly distributed with diameters of 20-30 nm were prepared starting from poly(2-cinnamoyloxyethyl methacrylate)-*b*-

poly(*tert*-butyl acrylate) (PCEMA-*b*-PtBA) for selective elimination of the minority component (PtBA) by hydrolysis¹³⁷⁻¹³⁸ (Figure 1.13).

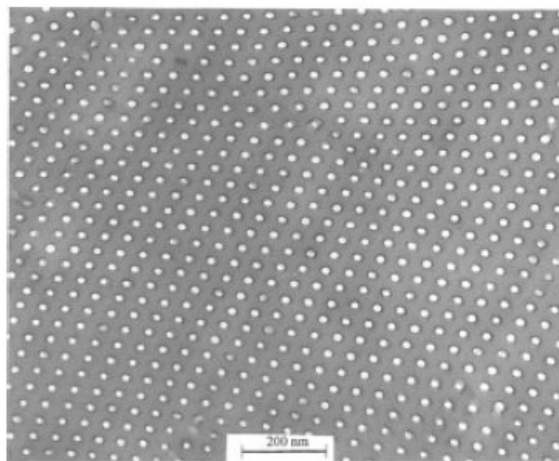


Figure 1.13: TEM image of a film of PCEMA-*b*-PtBA after the selective elimination of the cylindrical microdomains of PtBA by hydrolysis.

1.5.1 Nanocomposites

Within the present PhD thesis special emphasis to BCP-based nanocomposites is devoted. Nanocomposites represent a class of composite materials constituted by a polymeric matrix and nanoparticles (called *nanofillers*). By nanoparticles it is intended particles having at least one dimension on the scale of nanometers.

A great potentiality of block copolymers is represented by the possibility to use ordered nanostructures formed through self-assembly as matrices (*hosts*) for the inclusion of guest molecules (*guests*) and the dispersion of different kind of nanoparticles, in order to obtain nanocomposites with unique physical properties. Different microdomains of the so generated nanostructures from block copolymers (lamellae, spheres or cylinders) act as hosts to sequester selectively the nanofillers (*guests*) of appropriate chemical and geometrical affinity.³⁴

The great innovation of this field of research consists in the employment of nanostructured block copolymers as a matrix, instead of homopolymers. The use of BCP offers the unique

opportunity to control the spatial and orientation distribution of the nanofillers. In other terms the nanoparticles, able to induce specific properties, are not randomly distributed in the polymeric matrix but sequestered in the ordered microdomains and consequently in an ordered manner all over the matrix. This behavior permits a better control over the final physical properties of the nanocomposites. In Figure 1.14 it is shown a TEM image of a thin film of a nanocomposite based on a lamellar block copolymer where gold nanoparticles are included only in specific layers of the nanostructure.³⁴

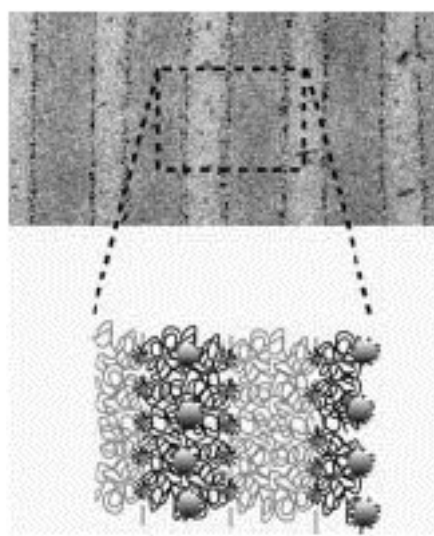


Figure 1.14: TEM bright-field image of a thin film of a polystyrene-poly(ethylene-co-propylene) block copolymer where opportunely passivated gold nanoparticles are included inside the domains of polystyrene.

The possibility to control the final morphology of the block copolymers, designing precise molecular architecture makes these materials as ideal tools for the development of novel nanocomposites where the guest molecules distribution is driven by the structuration of the matrix (*structure-guiding host nanocomposites*).³⁴

The possible outlooks linked to the development of such materials depend strictly on the improvement of the final physical properties of the materials, and from the kind of applications that could emerge from the presence of long-range order of the nanoparticles, taking advantage of both the physical properties of the polymeric matrix and the nanospecific characteristics of the included component.

To design and realise nanocomposites based on the above materials, the combination of the sol-gel synthesis and the self-assembly of block copolymers to prepare well-defined inorganic nanoparticles included into nanoscale structures appears to be a promising and innovative

strategy.¹³⁹⁻¹⁴² In fact, the sol-gel technique allows preparing active inorganic phases with a high control of purity, composition, microstructure and textural properties of the final material, while the technology of preparation of BCPs can be used to give special characteristics to the material in terms of ordered structure, well-organised porosity and flexibility.

Therefore the two technologies combine the typical advantages of the inorganic materials (rigidity, high thermal stability) with those of the polymeric materials (polymeric chains flexibility, ductility and processability).

The main characteristic of the sol-gel synthetic procedure will be discussed below for a better understanding of its fundamental aspects.

1.6 The sol-gel technology

The sol-gel is a versatile wet chemical process to synthesize ceramic and glass materials. This synthesis technique involves the transition of a system from a colloidal liquid, named sol, into a solid gel phase.^{11,143,144} By the sol-gel process, it is possible to fabricate ceramic or glass materials in a wide variety of forms: ultra-fine or spherical shaped powders, thin film coatings, ceramic fibers, microporous inorganic membranes, monolithic gels, or extremely porous aerogels. An overview of the sol-gel process is illustrated in Figure 1.15.

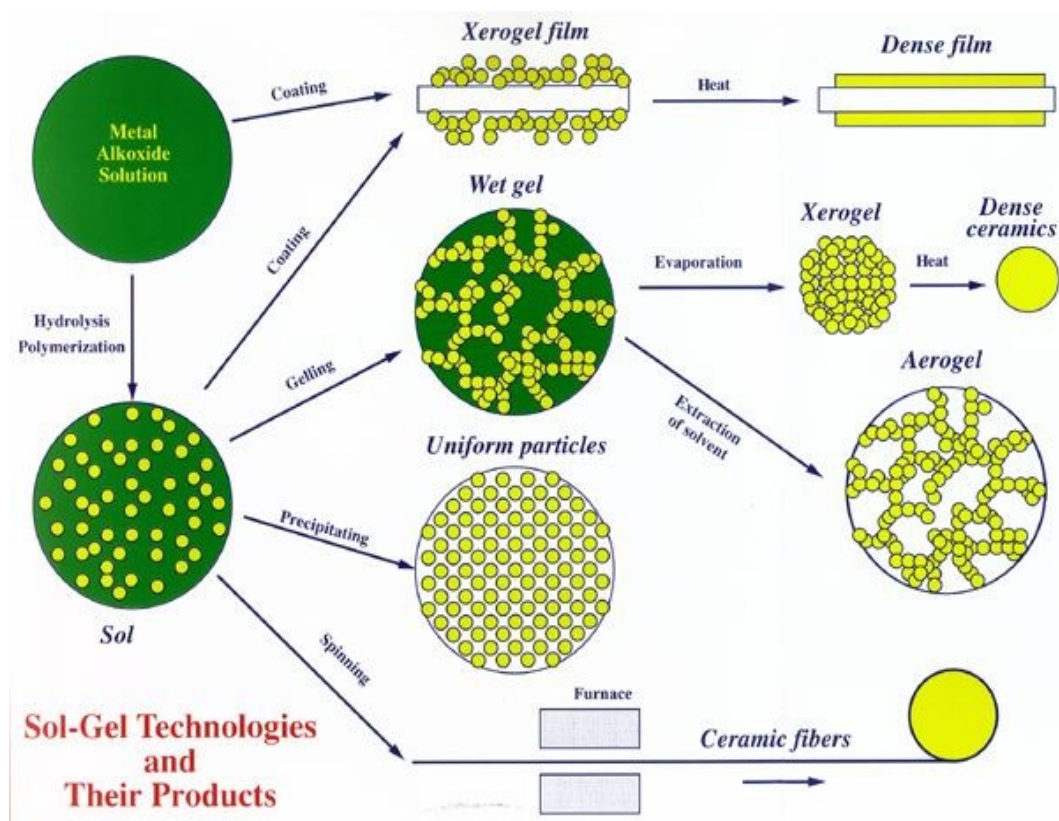


Figure 1.15: Schematic representation of the sol-gel process and its products.

The starting materials used in the preparation of the sol are usually inorganic metal salts or metal organic compounds, that are subjected to a series of hydrolysis and polycondensation reactions to form the wet gel.^{11,143,144} Suitable heat treatment of wet gel allow to obtain ceramic materials in different forms. Thin films can be produced by spin-coating or dip-coating. When the sol is cast into a mould, a wet gel will form. By proper heat-treatment, the

wet gel is converted into dense ceramic or glass materials. If the liquid in a wet gel is removed under a supercritical condition, a highly porous and extremely low density aerogel material is obtained. As the viscosity of a sol is adjusted into a suitable viscosity range, ceramic fibers can be drawn from the sol. Ultra-fine and uniform ceramic powders are formed by precipitation, spray pyrolysis, or emulsion techniques.

The main advantages of the sol-gel technique include the low process temperature, the ability to control the composition on molecular scale and the porosity, the homogeneity of the final product up to atomic scale. Moreover, it is possible to synthesize complex composition materials, to form high purity products through the use of high purity reagents, and to provide coatings over complex geometries.^{11,143,144}

1.6.1 Sol-gel chemistry

❖ *The role of the precursors*

Metallic alkoxides with general formula $M_y(OR)_y$, where M = element with valence y and R = *alkoxide group*, are generally used as molecular precursor of reagents.

These alkoxides must exhibit useful properties to control the chemical synthesis of oxides:

1. *easy to purify*: a lot of alkoxides can be distilled in order to obtain highly pure products;
2. *wide variety*: it is possible to choose R among a large number of alkylic groups in order to obtain the expected reactivity;
3. *possible control* of hydrolysis and polycondensation reactions;
4. *mixed alkoxides* as a further control of the stoichiometry and homogeneity of the obtained products.

❖ *Gelation: hydrolysis and polycondensation*

The transition from sol to gel involves two key steps, hydrolysis and polycondensation. Generally, the hydrolysis takes place also by small amounts of water. Moreover, it is necessary that the molecular precursors form a homogeneous solution. Then, non-aqueous solvent, such as alcohol, are added. In the hydrolysis reaction, the alkoxide groups (OR) are replaced stepwise by hydroxyl groups (OH):

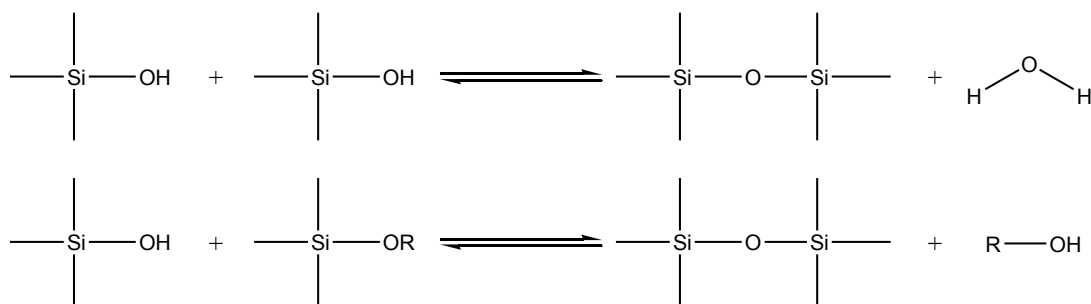


The hydrolysis rate was found to depend on many factors, among them the charge density on the metal, the number of metal ions bridged by an hydroxo- or oxo-ligand, and the size of the alkyl groups.^{145,146} Conversely, inhibition occurs as the number of hydroxo-ligand coordinating M increases or when the pH, temperature, or water and solvent concentration tend to favour the reverse reaction (esterification).

If the M-O bonds are highly polarized, due to high oxygen electronegativity compared to metal, their hydrolysis rates is fast. On the contrary, the hydrolysis rates of non-metal-oxygen bonds (Si-O, P-O, Ge-O) is slower. This aspect is very important for multi-component systems (mixed oxides) where the different hydrolysis rates of the precursors give self-condensation instead of cross-condensation, with formation of M-O-M and M'-O-M' instead of M-O-M' linkages. In this case a non-homogeneous gel is formed. Many solutions can be adopted to solve the above problem:

1. modification of the hydrolysis rate of the more reactive precursor using reaction inhibitors (for example chelants);
2. use of double alkoxides;
3. modification of the hydrolysis rate of the slower precursor by a catalyzed pre-hydrolysis (acid or basic).

Simultaneously to the hydrolysis, the polycondensation reactions occur:



The polycondensation reactions involve hydroxyl groups and result in M-O-M' linkages which, in turn, yield a three dimensional network. The gel state is then best described as a viscoelastic material composed of interpenetrating solid and liquid phases.¹⁴⁷ Its structure is strongly dependent on the water content in the system and on the catalysis nature. In acidic solution or for low water concentration, weakly cross-linked linear chains are produced (see Figure 1.16a), resulting in a soft gel which can be readily redispersed in solution. On the other hand, in base-catalyzed solutions, branched clusters are preferentially formed (see Figure 1.16b) and their propensity to coalesce is responsible of the solution gelation.^{148,149}



(a)



(b)

Figure 1.16: Gel structure: (a) crosslinked linear chains; (b) branched clusters.

❖ *Transformations of the gel*

The wet gel, obtained by hydrolysis and polycondensation reactions, must be subjected to suitable heat treatments to transform it into the final product (glass or ceramic), with the expected characteristics.

In the drying process, the wet gel is heated at about 373 K to allow the evaporation of the water physically trapped into the polymeric network as well as of residual alcohol. Many difficulties can arise during this stage as the removal of large amounts of liquid phase induces strong capillary forces causing large shrinkage and the formation of cracks. To minimize these effects, gels are normally dried very slowly and for coatings, the thickness usually must not exceed 10 μm .

The dried gel is annealed in the temperature range 573–773 K to remove the residual organic component. During these heat-treatments, the completion of condensation reactions takes place both on surface and inside the gel.

Usually, the nature and temperatures of the various reactions occurring during the heating are evaluated by differential thermal analysis (DTA).

1.7 Description of the thesis work

The aim of this PhD project has been the preparation of nanostructured organic/inorganic hybrid and inorganic materials, by a novel synthetic strategy that combines the bottom-up approach of the sol-gel technique, which is versatile and cheap, and the property of block copolymers to form ordered nanostructures by self-assembly. These nanocomposites have been obtained as thin films. Special efforts have been devoted toward achievements of nanostructures with long range order extended over macroscopic surfaces. The achievement of a long range order at nanometer scale over macroscopic surfaces is fundamental not only from a point of view of the basic knowledge but also to enlarge the application field of these materials. In the literature examples of nanocomposite materials obtained with a synthetic approach analogous to the one discussed here have been reported.¹³⁹⁻¹⁴² However, the results were not promising for applications due to the lack of nanostructural organization over a large area. This is due to the intrinsic difficulties to combine the sol-gel process protocol with the self-assembling ability of block copolymers.

Therefore combining the nanostructuring ability of BCPs with the crosslinking reactions of metal oxide precursor via sol-gel technique is still a challenge. In particular during the three

years project of this PhD work special attention has been devoted toward the set-up of methods to achieve well reproducible nanostructured metal oxide substrates, resorting to the combination of two leading procedures: self-assembly from BCP and sol-gel technique.

The BCP used was polystyrene-*b*-poly(ethylene oxide) (PS-*b*-PEO) with molecular mass 136 kDa and the volume fraction (ϕ) of PEO block equal to 23%. This ensured the formation of cylindrical nanostructures characterized by hexagonal arrangement of PEO cylinders inside the PS matrix. The amphiphilic nature of the BCP allowed selective inclusion of metal oxides, namely TiO₂ or Nb₂O₅, and its precursors inside the PEO cylindrical domains. The precursor used was titanium tetraisopropoxide (TTIP) and Nb (V) ethoxide, respectively.

Initially, thin films of the sole copolymer have been prepared on different substrates through spin coating technique. In the second step highly stable organic/inorganic nanocomposites with a well-defined nanostructure have been obtained, by selective inclusion of the metal alkoxide precursors in the PEO domains. In the third step an ordered disposition of inorganic oxides nanoparticles according to the templating pattern of the BCP has been obtained by removing the organic component at high temperature.

In the case of TiO₂ based BCP nanocomposites, since the titania motifs are reminiscent of the long range order achieved by BCP alone, procedures for improving the long-range order in the hexagonal packing of PEO cylinders have been set-up. A novel "solvent annealing" technique has been devised to enhance the order of the neat BCP and of the hybrid materials. Different solvent under different humidity conditions have been tested.

In the present thesis, the description of the materials, methods and techniques used for preparation and characterization of BCP/metal oxides samples are reported in Chapter 2.

In Chapter 3 the results obtained in the characterization of the thin films are reported along with the characterization of initial materials used for preparation of hybrid nanocomposites.

The methods developed to achieve the long range order of nanostructured thin films are also described in details in Chapter 3.

In Chapter 4, a possible application of the hybrid and heat-treated thin films is described, namely related to the soot detection by measurements of conductivity, with the final objective of fabrication of a soot sensor. These results are critically reviewed in Chapter 4, whereas Chapter 5 is dedicated to the conclusions.

Bibliography of Chapter I

1. Sohn B.H., Seo B.H., *Chem. Mater.* **2001**, *13*, 1752–7.
2. Horiuchi S., Fujita T., Hayakawa T., Nakao T., *Langmuir* **2003**, *19*, 2963–73.
3. Zehner R.W., Lopes W.A., Morkved T.L., Jaeger H., Sita L.R., *Langmuir* **1998**, *14*, 241–4.
4. Zehner R.W., Sita L.R., *Langmuir* **1999**, *15*, 6139–41.
5. Shenhar R., Jeoung E., Srivastava S., Norsten T.B., Rotello V.M., *Adv. Mater.* **2005**, *17*, 2206–10.
6. Morkved T.L., Wiltzius P., Jaeger H.M., Grier D.G., Witten T.A., *Appl. Phys. Lett.* **1994**, *64*, 422–4.
7. Lopes W.A., Jaeger H.M., *Nature* **2001**, *414*, 735–8.
8. Lopes W.A., *Phys. Rev. E* **2002**, *65*, 031606/1-14.
9. Ansari I.A., Hamley I.W., *J. Mater. Chem.* **2003**, *13*, 2412–3.
10. Hayward R.C., Chmelka B.F., Kramer E.J., *Adv. Mater.* **2005**, *17*, 2591–5.
11. Brinker, C. J., Scherer, G. W., *Sol-Gel Science: The Physics and Chemistry of Sol-Gel Processing*, Academic Press: Boston, **1990**.
12. Park, C., Yoon, J., Thomas, E. L., *Polymer* **2003**, *44*, 6725.
13. Krausch, G., Magerle, R., *Adv. Mater.* **2002**, *14*, 1579.
14. Hamley, I. W., *Angew. Chem., Int. Ed.* **2003**, *42*, 1692.
15. Lazzari, M., Lopez-Quintela, M. A., *Adv. Mater.* **2003**, *15*, 1583.
16. Lu, W., Sastry, A. M., *IEEE Trans. Semicond, Manuf.* **2007**, *20*, 421.
17. Hawker, C. J., Russell, T. P., *MRS Bull.* 2005, *30*, 952.
18. Li, M. Q., Coenjarts, C. A., Ober, C. K., *Adv. Polym. Sci.* **2005**, *190*, 183.
19. Segalman, R. A., *Mater. Sci. Eng. R. Rep.* **2005**, *48*, 191,
20. Cheng, J. Y., Ross, C. A., Smith, H. I., Thomas, E. L., *Adv. Mater.* **2006**, *18*, 2505.
21. Stoykovich, M. P., Nealey, P. F., *Mater. Today* **2006**, *9*, 20.
22. Krishnamoorthy, S., Hinderling, C., Hcinzelmann, H., *Mater. Today* **2006**, *9*, 40.

23. Li, M. Q., Ober, C. K., *Mater. Today* **2006**, *9*, 30.
24. Fasolka, M. J., Mayes, A. M., *Annu. Rev. Mater. Res.* **2001**, *31*, 323.
25. Darling, S. B., *Prog. Polym. Sci.* **2007**, *32*, 1152.
26. Kim, H.C., Hinsberg, W. D. J., *Vac. Sci. Technol., A* **2008**, *26*, 1369.
27. Bates F. S., Fredrickson G. H., *Phys. Today* **1999**, *52*, 32.
28. Abetz, V., Simon, P. F., *Adv. Polym. Sci.* **2005**, *189*, 125.
29. Van Zoelen, W., ten Brinke G., *Soft Matter* **2009**, *5*, 1568.
30. Bruning, J. H., *Proc. Soc. Photo-Opt. Eng.* **2007**, *6520*, 6520041.
31. Bates F. S., Fredrickson G. H., *Annu. Rev. Phys. Chem.* **1990**, *41*, 525; L. Leibler, *Macromolecules* **1980**, *13*, 1602.
32. Fan S., Kyu T., *Macromolecules* **2000**, *33*, 9568.
33. Khandpur A. K., Farster J. S., Bates F. S., *Macromolecules* **1995**, *28*, 8796.
34. Bockstaller M. R., Mickiewicz R. A., Thomas E. L., *Adv. Mat.* **2005**, *17*, 1331.
35. Hild G., Lamps J.P., *Polymer* **1998**, *39*, 2637.
36. Narrainen A. P., Pascual S., David M. H., *J. Polym. Sci. Part A, Polymer Chemistry* **2002**, *40*, 439
37. *Block Copolymers in Nanoscience*. Massimo Lazzari, Guojun Liu, Sébastien Lecommandoux Copyright © 2006 WILEY-VCH Verlag GmbH & Co. KGaA, Weinheim ISBN: 3-527-31309-5.
38. Keller A., Pedemonte E., Willmouth F.M., *Nature* **1970**, *225*, 538.
39. Folkes M. J., Keller A., Scalisi F. P., *Colloid. Polym. Sci.* **1973**, *251*, 1.
40. Kofinas P., Cohen R. E., *Macromolecules* **1995**, *28*, 3361.
41. Drzal P. L., Barnes J. D., Kofinas P., *Polymer* **2001**, *42*, 5633.
42. Quiram D. J., Register R. A., Marchand G. R., Adamson D. H., *Macromolecules* **1998**, *31*, 4891.
43. Van Asselen O. L. J., van Casteren I. A., Goossens J. G. P., Meijer H. E. H., *Macromol. Symp.* **2004**, *205*, 85.
44. Skoulios A., *J. Polym. Sci. Polym. Symp.* **1977**, *58*, 369.
45. Hadziioannou G., Mathis A., Skoulios A., *Colloid. Polym. Sci.* **1979**, *257*, 15.
46. Hadziioannou G., Mathis A., Skoulios A., *Colloid. Polym. Sci.* **1979**, *257*, 136.

47. Morrison F. A., Winter H. H., *Macromolecules* **1989**, *22*, 3533.
48. Morrison F. A. , Winter H. H., Gronski W., Barnes J. D., *Macromolecules* **1990**, *23*, 7200.
49. Wiesner U., *Macromol. Chem. Phys.***1997**, *198*, 3319.
50. Scott Pinheiro B., Winey K. I., *Macromolecules* **1998**, *31*, 4447.
51. Leist H., Maring D.,Thurn- Albrecht T., Wiesner U., *J. Chem. Phys.* **1999**, *110*, 8225.
52. Hermel T. J., Wu L. F., Hahn S. F., Lodge T. P., Bates F. S., *Macromolecules* **2002**, *35*, 4685.
53. Stangler S., Abetz V., *Rheol. Acta* **2003**, *42*, 569.
54. Wu L., Lodge T. P., Bates F. S., *Macromolecules* **2004**, *37*, 8184.
55. Sebastian J. M., Graessley W. W., Register R. A., *J. Rheol.* **2002**, *46*, 863.
56. Angelescu D. E., Waller J. H., Register R. A., Chaikin P. M., *Adv. Mater.* **2005**, *17*, 1878.
57. Angelescu D. E., Waller J. H., Adamson D. H., Deshpande P., Chou S. Y., Register R. A., Chaikin P. M., *Adv. Mater.* **2004**, *16*, 1736.
58. Luo K. F., Yang Y. L., *Polymer* **2004**, *45*,6745.
59. Albalak R. J., E. L. Thomas E. L., *J. Polym. Sci. Polym. Phys.* **1993**, *31*, 37.
60. Albalak J., Thomas E. L., *J. Polym. Sci. Polym. Phys.* **1994**, *32*, 341.
61. Honeker C. C., Thomas E. L., Albalak R. J., Hajduk D. A., Gruner S. M., Capel M. C., *Macromolecules* **2000**, *33*, 9395.
62. Dair B. J., Avgeropoulos A., Hadjichristidis N., *Polymer* **2000**, *41*, 6231.
63. Villar M. A., Rueda D. R., Ania F., E. L.Thomas, *Polymer* **2002**, *43*, 5139
64. Morkved T. L., Lu M., Urbas A. M., Ehrichs E. E., Jaeger H. M., Mansky P., Russell T. P., *Science* **1996**, *273*, 931.
65. Onuki A., Fukuda J., *Macromolecules* **1995**, *28*, 8788.
66. Thurn-Albrecht T., Steiner R., DeRouchey J., Stafford C. M., Huang E., Bal M., Tuominen M., Hawker C. J., Russell T. P., *Adv. Mater.* **2000**, *12*, 787.
67. Thurn-Albrecht T., DeRouchey J., Russell T. P., Kolb R., *Macromolecules* **2002**, *35*, 8106.
68. Elhadj S., Woody J. W., Niu V. S., Saraf R. F., *Appl. Phys. Lett.* **2003**, *82*, 872.
69. Xu T., Zhu Y., Gido S. P., Russell T. P., *Macromolecules* **2004**, *37*, 2625.

70. DeRouchey J., Thurn-Albrecht T., Russell T.P., Kolb R., *Macromolecules* **2004**, *37*, 2538.
71. Xiang H., Lin Y., Russell T. P., Kolb R., *Macromolecules* **2004**, *37*, 5358.
72. Thurn-Albrecht T., Schotter J., Kästle G. A., Emley N., Shibauchi T., Krusin-Elbaum L., Guarini K., Black C. T., Tuominen M. T., Russell T. P., *Science* **2000**, *290*, 2126.
73. Osuji C., Ferreira P. J., Mao G., Ober C. K., Vander Sande J. B., Thomas E. L., *Macromolecules* **2004**, *37*, 9903.
74. Tomikawa N., Lu Z. B., Itoh T., Imrie C. T., Adachi M., Tokita M., Watanabe J., *Jpn. J. Appl. Phys. 2*, **2005**, *44*, L711.
75. Grigorova T., Pispas S., Hadjichristidis N., Thurn-Albrecht T., *Macromolecules* **2005**, *38*, 7430.
76. Turturro A., Gattiglia E., Vacca P., Viola G. T., *Polymer* **1995**, *21*, 3987.
77. Kim G., Libera M., *Macromolecules* **1998**, *31*, 2569.
78. Kim G., Libera M., *Macromolecules* **1998**, *31*, 2670.
79. Kim S. H., M. Misner J., Xu T., Kimura M., Russell T. P., *Adv. Mater.* **2004**, *16*, 226.
80. Kimura M., Mister M. J., Xu T., Kim S. H., Russell T. P., *Langmuir* **2003**, *19*, 9910.
81. Lin Z., Kim D. H., Wu X., Boosahda L., Stone D., LaRose L., Russell T. P., *Adv. Mater.* **2002**, *14*, 1373.
82. Temple K., Kulbaba K., Power-Billard K. N., Manners I., Leach K. A., Xu T., Russell T. P., Hawcker C. J., *Adv. Mater.* **2003**, *15*, 297.
83. Yang X. M., Peters R. D., Nealey P. F., Solak H. H., Cerrina F., *Macromolecules* **2000**, *33*, 9575.
84. Kim S. O., Solak H. H., Stoykovich M. P., Ferrier N. J., de Pablo J. J., Nealey P. F., *Nature (London)* **2003**, *424*, 411.
85. Yang X. M., Peters R.D., Kim T. K., Nealey P. F., *J. Vac. Sci. Technol. B*, **1999**, *17*, 3203.
86. Solak H. H., David C., Gobrecht J., Golovkina V., Cerrina F., Kim S.O., Nealey P. F., *Microelectron. Eng.* **2003**, *67-68*, 56
87. Matsen M.W., *Curr. Opin. Colloid Interf. Sci.* **1998**, *3*, 40.
88. Henke C. S., Thomas E. L., Fetters L. J., *J. Mater. Sci.* **1988**, *23*, 1685.
89. Coulon G., Deline V. R., Russell T. P., Green P. F., *Macromolecules* **1989**, *22*, 2581.
90. Anastasiadis S. H., Russell T. P., Satija S. K., Majkrzak C. F., *Phys. Rev. Lett.* **1989**, *62*, 1852.

91. Russell T. P., Coulon G., Deline V. R., Miller D. C., *Macromolecules* **1989**, 22, 4600.
92. Anastasiadis S. H., Russell T. P., Satija S. K., Majkrzak C. F., *J. Chem. Phys.* **1990**, 92, 5677.
93. Russell T. P., Menelle A., Anastasiadis S. H., Satija S. K., Majkrzak C. F., *Macromolecules* **1991**, 24, 6269.
94. Collin B., Chatenay D., Coulon G., Ausserre D., Gallot Y., *Macromolecules* **1992**, 25, 1621.
95. Coulon G., Dailant J., Collin B., Benattar J. J., Gallot Y., *Macromolecules* **1993**, 26, 1582.
96. Mayes A. M., Russell T. P., Bassereau P., Baker S. M., Smith G. S., *Macromolecules* **1994**, 27, 749.
97. Carvalho V, Thomas E. L., *Phys. Rev. Lett.* **1994**, 73, 3321.
98. Joly S., Ausserre D., Brotons G., Gallot Y., *Eur. Phys. J. E* **2002**, 8, 355.
99. Royer L., *Bull. Soc. Fr. Mineral. Crystallogr.* **1928**, 51, 7.
100. Van der Mere J. H., *Discuss. Faraday Soc.* **1949**, 5, 206.
101. Swei G. S., Lando J. B., Rickert S. E., Mauritz K. A., *Encyclopedia Polym. Sci. Eng.* **1986**, 6, 209.
102. Willems J., *Naturwissenschaften* **1955**, 42, 176.
103. Lovinger A. J., *J. Polym. Sci. Polym. Phys. Ed.* **1983**, 21, 97.
104. Wittmann J. C., Lotz B., *Prog. Polym. Sci.* **1990**, 15, 909.
105. Kopp S., Wittmann J. C., Lotz B., *Makromol. Chem. Macromol. Symp.* **1995**, 98, 917.
106. Wittmann J. C., Lotz B., *Polymer* **1989**, 30, 27.
107. Wittmann J. C., Hodge A. M., Lotz B., *J. Polym. Sci. Polym. Phys. Ed.* **1983**, 21, 2495.
108. Annette Thierry and Bernard Lotz Epitaxial crystallization of polymers: means and issues, *Handbook of Polymer Crystallization* In press.
109. De Rosa C., Park C., Thomas E. L., Lotz B., *Nature* **2000**, 405, 433
110. Smith H. I., Flanders D. C., *Appl. Phys. Lett.* **1978**, 32, 349.
111. Smith H. I., Geis M.W., Thompson C. V., Atwater H. A., *J. Cryst. Growth* **1983**, 63, 527.
112. Kobayashi T., Takagi K., *Appl. Phys. Lett.* **1984**, 45, 44.
113. Flanders D. C., Shaver D. C., Smith H. I., *Appl. Phys. Lett.* **1978**, 32, 597.

114. Wittmann J. C., Smith P., *Nature (London)* **1991**, 352, 414.
115. Hansma H., Motamedi F., Smith P., Hansma P., Wittmann J. C., *Polymer Commun.* **1992**, 33, 647.
116. Dietz P., Hansma P. K., Ihn K. J., Motamedi F., Smith P., *J. Mater. Sci.* **1993**, 28, 1372.
117. Fenwick D., Ihn K. J., Motamedi F., Wittmann J. C., Smith P., *J. Appl. Polym. Sci.* **1993**, 50, 1151.
118. Fenwick D., Smith P., Wittmann J.C., *J. Mater. Sci.* **1996**, 31, 128.
119. Liu G., Yan X., Duncan S., *Macromolecules* **2002**, 35, 9788.
120. Liu G., Yan X., Qiu X., Li Z., *Macromolecules* **2002**, 35, 7742.
121. a) Lopes W.A., Jaeger H.M., *Nature* **2001**, 414, 735. b) Lopes W.A., *Phys. Rev. E* **2002**, 65, 031 606
122. Park, M., Harrison C., Chaikin P. M., Register R. A., Adamson D. H., *Science* **1997**, 276, 1401
123. Park M., Chaikin P. M., Register R. A., Adamson D. H., *Appl. Phys. Lett.* **2001**, 79, 257.
124. Edrington A. C., Urbas A. M., De Rege P., Chen C. X., Swager T. M., Hadjichristidis N., Xenidou M., Fetters L. J., Joannopoulos J. D., Fink Y., Thomas E. L., *Adv. Mater.* **2001**, 13, 421.
125. Fink Y., Urbas A. M., Bawendi B. G., Joannopoulos J. D., Thomas E. L., *J. Lightwave Tech.* **1999**, 17, 1963.
126. Urbas A. M., Fink Y., Thomas E. L., *Macromolecules* **1999**, 32, 4748.
127. Urbas A. M., Sharp R., Fink Y., Thomas E. L., Xenidou M., Fetters L. J., *Adv. Mater.* **2000**, 12, 812.
128. Bockstaller M. R., Kolb R., Thomas E. L., *Adv Mater* **2001**, 13, 1783
129. Deng, T., Chen, C. X., Honeker, C., Thomas E. L., *Polymer* **2003**, 44, 6549
130. Urbas A. M., Maldovan M., De Rege P., Thomas E. L., *Adv. Mater.* **2002**, 14, 1850.
131. Maldovan M., Urbas A. M., Yufa N., Carter W. C., Thomas E. L., *Phys. Rev. B* **2002**, 65, 165123.
132. Maldovan M., Bockstaller M. R., Thomas E. L., Carter W. C., *Appl Phys B* **2003**, 00, 1.
133. Urbas A. M., Thomas E. L., Kriegs H., Fytas G., Penciu R. S., Economou L. N., *Phys. Rev. Lett.* **2003**, 90, 108302.

134. Osuji C., Chao C. Y., Bitá I., Ober C. K., Thomas E. L., *Adv. Funct. Mater.* 2002, 2, 753.
135. Hashimoto T., Tsutsumi K., Funaki Y., *Langmuir* **1997**, 13, 6869.
136. Apel P., *Radiat. Meas.* **2001**, 34, 559.
137. Liu G., Ding J., Hashimoto T., Kimishima K., Winnik F. M., Nigam S., *Chem. Mater.* **1999**, 11, 2233.
138. Tian J., Hustad D., Coates G.W., *J. Am Chem. Soc.* **2001**, 123, 5134.
139. Gutierrez J., Tercjak A., Mondragon I., *J. Am. Chem. Soc.* **2010**, 132, 873-878
140. Scalarone D., Tata J., Caldera F., Lazzari M., Chiantore O., *Mater. Chem. Phys.* **2011**, 128, 166.
141. Memesa M., Lenz S., Emmerling S. G. J., Nett S., Perlich J., Müller-Buschbaum P., Gutmann J.S., *Colloid Polym. Sci.* **2011**, 289, 943-953.
142. Kim D. H., Sun Z., Russell T.P., Knoll W., Gutmann J.S., *Adv. Funct. Mater.* **2005**, 15, 1160-1164
143. Brinker C.J., Bunker B.C. et al., *J. Am. Chem. Soc.*, part II **1988**.
144. Jones R.W., *Fundamental Principles of Sol-Gel Technology* **1989**
145. Klein L.C., Garvey G.J., *Mater. Res. Soc. Sym. Proc.* **1984**, 32.
146. Keefer K.D., *Mater. Res. Soc. Sym. Proc.*, **1984**, 32
147. Hurd C.B., *Chem. Rev.* **1938**, 22, 403.
148. Lockwood J.D., *Nanostructure Science and Technology, Surface Effects in Magnetic Nanoparticles*, Springer: New York, **2005**.
149. Nguyen L.Q., Salim C., Hinode H., *Appl. Catal. A-Gen.* **2008**, 347, 94.

CHAPTER II

Materials and methods

Experimental part

2.1 Analyzed sample

In this PhD thesis work a polystyrene-*b*-poly(ethylene oxide) PS-*b*-PEO sample here abbreviated SEO was employed as templating agent for the subsequent addition of the inorganic material. In particular this sample presents an amorphous block of polystyrene (PS) chemically linked to a block of semicrystalline poly(ethylene oxide) (PEO). The sample was purchased from the Polymer Source Inc. In table 2.1 the main characteristic of this sample are reported.

Table 2.1 Number average molecular weight (M_n), polydispersity index of the molecular masses ($PDI = M_w/M_n$), volume fraction of the PEO block (ϕ_{PEO} or f_{PEO}) and glass transition temperature (T_g).

Sample	$M_n \times 10^3$ ^a (g/mol)	M_w/M_n ^a	f_{PEO} (%)	T_g (°C)
PS- <i>b</i> -PEO	102.0- <i>b</i> -34.0	1.18	23	-30°C

a) Obtained by SEC analysis.

The sample of PS-*b*-PEO presents the following chemical structure (Figure 2.1):

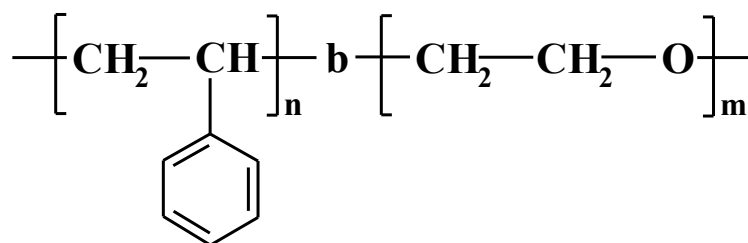
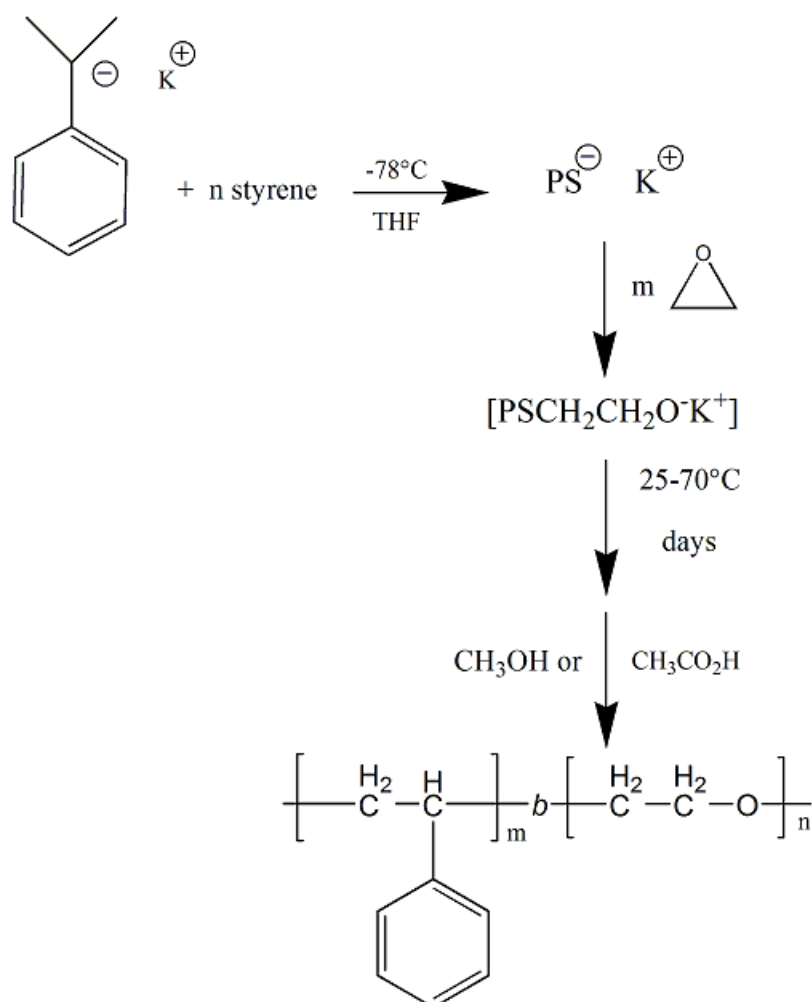


Figure 2.1: Structure of the block copolymer PS-*b*-PEO.

Poly(styrene-*b*-ethylene oxide) diblock copolymer is prepared by living anionic polymerization. Living anionic polymerization was early described and illustrated by Szwarc and co-workers in 1956.¹ Their initial work was based on the polymerization of styrene and dienes. Living anionic polymerization, especially alkyllithium initiated polymerizations, provides convenient and reliable procedures for synthesis of well-defined block copolymers with controlled molecular weight, narrow molecular weight distribution and low degrees of compositional heterogeneity.

Poly(styrene-*block*-ethylene oxide) is generally synthesized using a polymeric potassium alkoxide initiator for ethylene oxide polymerizations² as shown in Scheme 1 or direct addition of potassium salts to promote ethylene oxide polymerization using polymeric lithium alkoxides as initiators.³



Scheme 1: Living anionic polymerization of PS-*b*-PEO starting from a polymeric potassium alkoxide as initiator.

The molecular weight and polydispersity index (PDI) of the block copolymer have been characterized by size exclusion chromatography (SEC). The polymer is soluble in THF (at 35°C), CHCl₃, benzene, toluene, dioxane. The volume fraction of PEO was calculated from the relation:

$$f_{PEO}(\%) = \frac{M_{n(PEO)} / \rho_{(PEO)}}{M_{n(PEO)} / \rho_{(PEO)} + M_{n(PS)} / \rho_{(PS)}} \times 100$$

Where $M_{n(PEO)}$ e $M_{n(PS)}$ are the number average molecular weights of PEO and PS blocks, $\rho_{(PEO)}$ and $\rho_{(PS)}$ are the density of the polymers (1.064g/cm³ for PEO block and 0.969g/cm³ for PS block).⁴

The volume fraction of PEO (f_{PEO}) in the SEO copolymer is 23%. The volume fraction of PEO block of 23% was selected in order to obtain the cylindrical morphology of PEO cylinders in the PS matrix (Paragraph 1.3).

2.2 Thermal and structural analysis

2.2.1 Thermal analysis

Thermal analysis of SEO was performed by differential scanning calorimetry (DSC), in order to detect the melting point, the crystallization temperature and the glass transition temperature. DSC Mettler-822 calorimeter was used with the *intra cooler* system. Few milligrams of the sample were thermally scanned, under nitrogen flow, in an appropriate temperature range. The sample was first heated to a temperature above its melting point, then quenched and finally heated once again until melting. From the DSC curves of the thermal cycle, the temperature of first heating, crystallization and second heating were obtained. The sample was heated at a constant rate of 10°C/min.

Thermogravimetric analysis (TG) was performed at the Center for Research in Biological Chemistry and Molecular Materials (CIQUS) of the University of Santiago de Compostela to evaluate the weight loss of the SEO by heating on a thermobalance (TGA Q5000 IR

Thermogravimetric Analyzer of TA Instruments) in 100 mL min⁻¹ N₂ flow with 10 K min⁻¹ heating rate.

Differential thermal analysis provided data on the crystallization behaviour of the inorganic materials. The DTA was carried out by using a high temperature DTA unit (Netzsch, DSC 404 model) with Al₂O₃ as reference material. The DTA curves, recorded in air from room temperature up to 1273 K at a heating rate of 10 K min⁻¹, were carried out on about 30 mg of dried gel specimens.

2.2.2 Wide angle X-ray scattering (WAXS)

X-rays diffraction patterns of the analyzed samples were obtained by a Philips automatic powder diffractometer, using the Cu K α (nickel-filtered) radiation. The diffraction patterns were registered scanning continuously the diffraction angle 2θ at a rate of 0.01°/s. X-ray diffraction patterns were also collected for SEO films obtained from melt between the hot plates of a press by cooling to room temperature by fluxing water in the refrigeration system of the press. Diffraction patterns of so obtained melt pressed films were collected at different temperatures (from -50°C to 170°C).

2.2.3 Fourier transform infrared spectroscopy

Fourier transform infrared spectroscopy (FTIR) was used to have a detailed analysis of material structure and to point out the possible modifications after heat treatments. The dried gels were heated at a heating rate of 5 K min⁻¹ up to 373, 673, 873 and 1073 K, and kept at these temperatures up to achieve constant weight. The FTIR spectra of dried and heat-treated gel samples were carried out at room temperature by a Nicolet system, Nexus model, equipped with a DTGS KBr (deuterated triglycine sulfate with potassium bromide windows) detector. The absorption spectra were recorded in the 4000–400 cm⁻¹ range with a spectral resolution of 2 cm⁻¹ on samples diluted in KBr. To this end, mixture 2% weight of each sample in KBr were prepared and, 200 mg of this mixture were successively pressed in form of tablets with diameter 13 mm. The spectrum of each sample represents an average of 64 scans, which was corrected for the spectrum of the KBr blank.

The hybrid solutions containing a different amount of metal precursors were analysed using a high-performance diamond single bounce ATR accessory (“Thermo Scientific Smart Orbit” of Thermo Scientific Nicolet FT-IR Systems available at the CIQUS of the University of

Santiago de Compostela). Diamond ATR is ideal for analysis of hard, abrasive, reactive, caustic or corrosive materials because it is both inert and extremely strong.

To allow the comparison of the absorbance values, all FTIR spectra were normalized with respect to the absorption bands at 3025 and 2968 cm^{-1} .

2.3 Morphological analysis

2.3.1 Transmission electron microscopy (TEM)

For the transmission electronic microscope is used a scheme similar to the optical microscope. The incident beam is transmitted through the sample and project its image on a fluorescent screen, instead of an eyepiece. The electrons are generated by a tungsten filament and accelerated by a potential difference. The focusing of the beam is entrusted to a complex series of electromagnetic lens, generally from six to eight, constituted by electromagnetic windings symmetrically disposed around the incident beam. They adjust the path of the deflected electrons in direction of the main axis of the electron beam under high-vacuum. The thickness of the sample must be ultra-thin (from 5 to 500 nm) because the electron are transmitted through the specimen and this fact explains the intrinsic difficulties to prepare TEM samples.

TEM images have been obtained by a Philips EM 208S microscope operating at a voltage of 120kV (point resolution of 0,3 nm) available at C.I.S.M.E. (Centro Interdipartimentale di Servizio per la Microscopia Elettronica) of the University of Naples “Federico II” and with a Philips CM-12 TEM (accelerating voltage of 120 kV) at the CACTUS (Centro de Apoyo Científico-Tecnológico de la Universidad de Santiago de Compostela).

In some cases the grids (200 mesh copper grips purchased from Aldrich) where the sample was deposited underwent to a *staining* process with RuO_4 . This process consists in exposing the grids to vapors originated from an aqueous solution of RuO_4 .

According to literature both PS and PEO can be stained via RuO_4 oxidation, and staining PEO is generally viewed to be easier compared with PS.^{5,6}

The preparation of the solution of RuO_4 consists in dissolving in a flask at room temperature 1g of sodium periodate (NaIO_4) in 25 ml of distilled water. The solution changes from transparent to whitish and is placed in a water/ice bath to lower the solution temperature to 1-

5 °C. Once that this temperature is reached 0.15 g of ruthenium oxide (RuO_4) are added to the solution. Finally, the flask containing the solution is removed from the water/ice bath and stirred avoiding light exposure for about 3-4 hours.

2.3.2 Atomic Force Microscopy (AFM)

The AFM consists of a cantilever with a sharp tip (probe) at its end that is used to scan the specimen surface. The cantilever is typically silicon or silicon nitride with a tip radius of curvature on the order of nanometers. When the tip is brought into proximity of a sample surface, forces between the tip and the sample lead to a deflection of the cantilever according to Hooke's law. Depending on the situation, forces that are measured in AFM include mechanical contact force, van der Waals forces, capillary forces, chemical bonding, electrostatic forces, magnetic forces, Casimir forces, solvation forces, etc. Along with force, additional quantities may simultaneously be measured through the use of specialized types of probe. Typically, the deflection is measured using a laser spot reflected from the top surface of the cantilever into an array of photodiodes (see Figure 2.2).

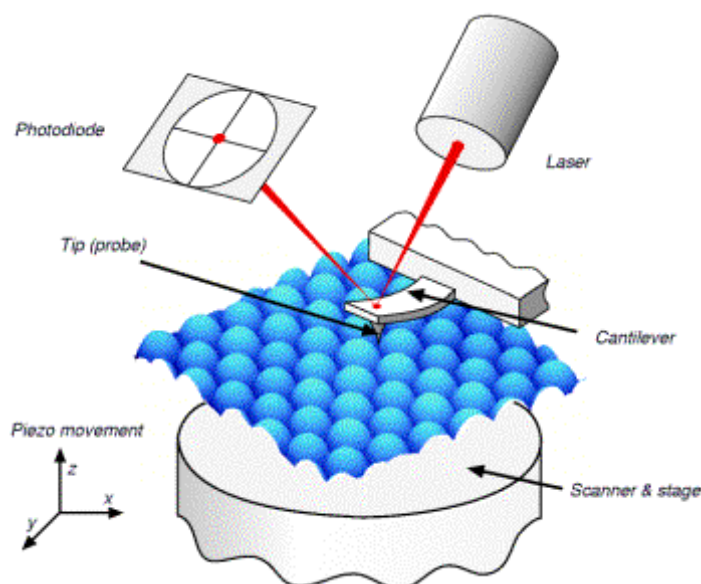


Figure 2.2: Schematic illustration of an AFM. The tip is attached to a cantilever, and is raster-scanned over a surface. The cantilever deflection due to tip-surface interactions is monitored by a photodiode sensitive to laser light reflected at the tip backside.

Other methods that are used include optical interferometry, capacitive sensing or piezoresistive AFM cantilevers. These cantilevers are fabricated with piezoresistive elements that act as a strain gauge. Using a Wheatstone bridge, strain in the AFM cantilever due to deflection can be measured, but this method is not as sensitive as laser deflection or interferometry.

If the tip was scanned at a constant height, a risk would exist that the tip collides with the surface, causing damage. Hence, in most cases a feedback mechanism is employed to adjust the tip-to-sample distance to maintain a constant force between the tip and the sample. Traditionally, the sample is mounted on a piezoelectric tube, that can move the sample in the z direction for maintaining a constant force, and the x and y directions for scanning the sample. Alternatively a 'tripod' configuration of three piezo crystals may be employed, with each responsible for scanning in the x,y and z directions. This eliminates some of the distortion effects seen with a tube scanner. In new designs, the tip is mounted on a vertical piezo scanner while the sample is being scanned in x and y using another piezo block. The resulting map of the area $z = f(x, y)$ represents the topography of the sample.

The AFM analysis can be operated in a number of modes, depending on the application. In general, possible imaging modes are divided into static (also called contact) modes and a variety of dynamic (non-contact or "tapping") modes where the cantilever is vibrated.

The AFM images reported in this PhD thesis were obtained at room temperature by a Caliber, Veeco Instruments microscope and were performed in tapping mode.

Silicon probes having a tip nominal radius of curvature of 8 nm, with a force constant of 42 N/m were used. The resonance frequency was about 320 kHz with a scan rate of 1 Hz s⁻¹. The sample line was 256 or 512 and the target amplitude was around 0.6 V.

In order to obtain repeatable results of neat block copolymers, different regions of the specimens were scanned.

In tapping mode, the tip of the cantilever does not contact the sample surface. The cantilever is instead oscillated at a frequency slightly above its resonant frequency where the amplitude of oscillation is typically a few nanometers (<10 nm). The van der Waals forces, which are strongest from 1 nm to 10 nm above the surface, or any other long range force which extends above the surface acts to decrease the resonance frequency of the cantilever. This decrease in resonant frequency combined with the feedback loop system maintains a constant oscillation amplitude or frequency by adjusting the average tip-to-sample distance. Measuring the tip-to-sample distance at each (x, y) data point allows the scanning software to construct a topographic image of the sample surface.

Non-contact mode AFM does not suffer from tip or sample degradation effects that are sometimes observed after taking numerous scans with contact AFM. This makes non-contact AFM preferable to contact AFM for measuring soft samples.

2.3.3 Scanning electron microscopy (SEM)

A scanning electron microscope (SEM) is a type of electron microscope that produces images of a sample by scanning over it with a focused beam of electrons. The electrons interact with electrons in the sample, producing various signals that can be detected and that contain information about the topography and composition of the surface of the sample. The electron beam is generally scanned in a raster scan pattern, and the position of the beam is combined with the detected signal to produce an image. SEM can achieve resolution better than 1 nanometer; specimens can be observed in high vacuum, low vacuum and in wet condition.

The types of signals produced by a SEM include secondary electrons, back-scattered electrons (BSE), characteristic X-rays, light (cathodoluminescence), specimen current and transmitted electrons. Secondary electron detectors are common in all SEMs, but it is rare that a single machine would have detectors for all possible signals. The signals result from interactions of the electron beam with atoms at or near the surface of the sample. In the most common or standard detection mode, secondary electron imaging or SEI, the SEM can produce very high-resolution images of a sample surface, revealing details less than 1 nm in size. Due to the very narrow electron beam, SEM micrographs have a large depth of field yielding a characteristic three-dimensional appearance useful for understanding the surface structure of a sample. A wide range of magnifications is possible, from about 10 times (about equivalent to that of a powerful hand-lens) to more than 500,000 times, about 250 times the magnification limit of the best light microscopes.

Back-scattered electrons (BSE) are beam electrons that are reflected from the sample by elastic scattering. BSE are often used in analytical SEM along with the spectra made from the characteristic X-rays, because the intensity of the BSE signal is strongly related to the atomic number (Z) of the specimen. BSE images can provide information about the distribution of different elements in the sample. Characteristic X-rays are emitted when the electron beam removes an inner shell electron from the sample, causing a higher-energy electron to fill the shell and release energy. These characteristic X-rays are used to identify the composition and measure the abundance of elements in the sample.

In a typical SEM (see Figure 2.3), an electron beam is thermionically emitted from an electron gun fitted with a tungsten filament cathode. Tungsten is normally used in thermionic electron guns because it has the highest melting point and lowest vapor pressure of all metals, thereby allowing it to be heated for electron emission, and because of its low cost.

Other types of electron emitters include lanthanum hexaboride (LaB_6) cathodes, which can be used in a standard tungsten filament.

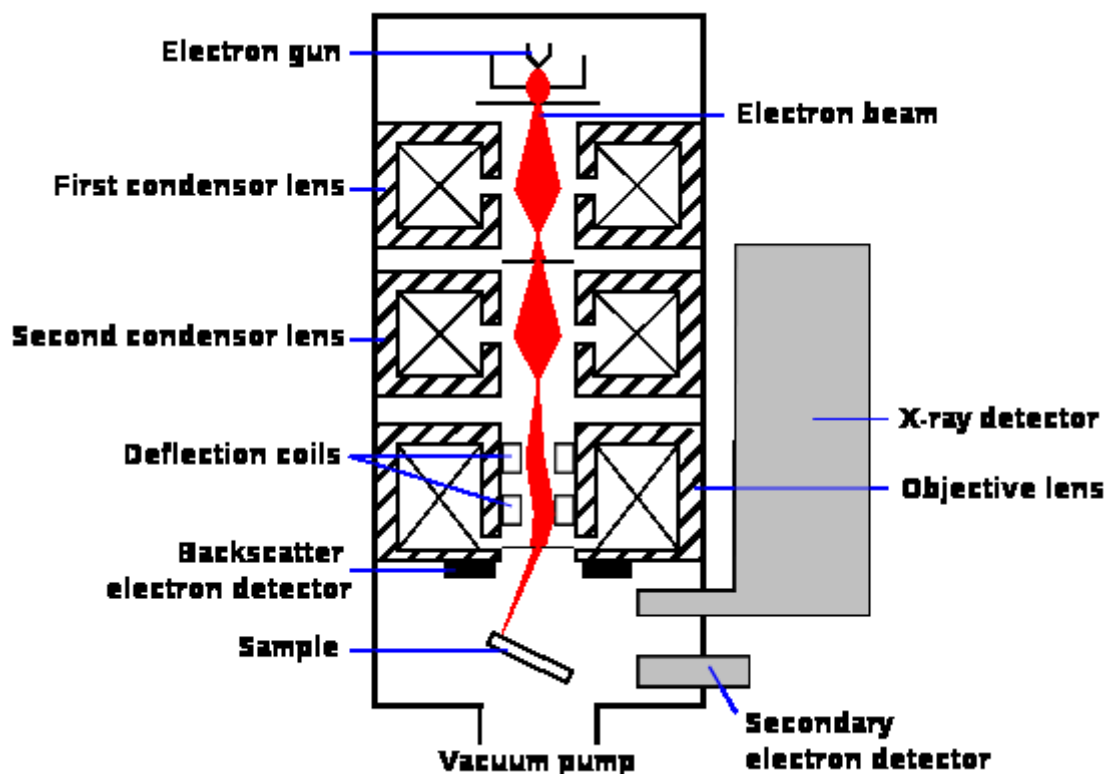


Figure 2.3: Schematic diagram of a scanning electron microscope (SEM).

The electron beam, which typically has an energy ranging from 0.2 keV to 40 keV, is focused by one or two condenser lenses to a spot about 0.4 nm to 5 nm in diameter. The beam passes through pairs of scanning coils or pairs of deflector plates in the electron column, typically in the final lens, which deflect the beam in the x and y axes so that it scans in a raster fashion over a rectangular area of the sample surface.

When the primary electron beam interacts with the sample, the electrons lose energy by repeated random scattering and absorption within a teardrop-shaped volume of the specimen known as the interaction volume, which extends from less than 100 nm to around 5 μm into

the surface. The size of the interaction volume depends on the landing energy of the electron, the atomic number of the specimen and the density of the specimen. The energy exchange between the electron beam and the sample results in the reflection of high-energy electrons by elastic scattering, emission of secondary electrons by inelastic scattering and the emission of electromagnetic radiation, each of which can be detected by specialized detectors. The beam current absorbed by the specimen can also be detected and used to create images of the distribution of specimen current. Electronic amplifiers of various types are used to amplify the signals, which are displayed as variations in brightness on a computer monitor (or, for vintage models, on a cathode ray tube). Each pixel of computer video-memory is synchronized with the position of the beam on the specimen in the microscope, and the resulting image is therefore a distribution map of the intensity of the signal being emitted from the scanned area of the specimen. In older microscopes image may be captured by photography from a high-resolution cathode ray tube, but in modern machines image is saved to a computer data storage.

All samples must also be of an appropriate size to fit in the specimen chamber and are generally mounted rigidly on a specimen holder called a specimen stub. Several models of SEM can examine any part of a 6-inch (15 cm) semiconductor wafer, and some can tilt an object of that size to 70°.

For conventional imaging in the SEM, specimens must be electrically conductive, at least at the surface, and electrically grounded to prevent the accumulation of electrostatic charge at the surface.

All the SEM images reported in the following chapters were obtained with a Zeiss Ultra Plus (see Figure 2.4) field emission SEM at 1.5 kV (range of acceleration voltage: 0.02 kV – 30 kV) equipped with a Inlens detector and a SE Everhart - Thornley Secondary Electron Detector at the CACTUS (Centro de Apoyo Científico-Tecnológico de la Universidad de Santiago de Compostela).



Figure 2.4: Overview of Zeiss Ultra Plus field emission SEM.

It was also equipped with EDX (Energy Dispersive X-ray) microanalysis. This micro-analytical technique uses the characteristic spectrum of X-rays emitted by the specimen after excitation by high-energy electrons to obtain information about its elemental composition. EDX is generally better suited to detecting elements of high atomic number (Z).

2.4 Thin film deposition technique: spin-coating

Hybrid films and block copolymer films have been prepared by spin coating a solution of BCP in a volatile organic solvent deposited onto a substrate (silicon wafers or glass). The polymer film spreads by centrifugal forces, and the volatile solvent is rapidly driven off. With care, the method can give films with a low surface roughness over areas of square millimeters. The influence of solvent evaporation on roughness has been studied by Strawhecker et al.⁷ They studied the behavior of two hydrophobic polymers which are glassy under ambient conditions, polystyrene (PS) and poly(ethylmethacrylate) (PEMA). The polymers were spin cast from solution onto smooth silicon wafers employing good solvents to avoid complications associated with the phase separation in the drying film. The roughness, and its standard deviation, increase monotonically with vapor pressure of the solvent P_{vp} (see Table

2.2 for the values of P_{vp} for different solvents), especially when $P_{vp} > 0.1$ bar [104 N/m²] as shown in Figure 2.5. For any given solvent, the roughness R_a decreased with increasing spin speed, and was found that R_a scaled linearly with film thickness.

Table 2.2: ^a γ is the surface tension, P_{vp} the vapor pressure and R_a the roughness of the resulting polymer films.

Table 1. Physical Properties of Solvents Employed^a

solvent	γ (dyn/cm)	P_{vp} (bar)	R_a (nm)
dichloromethane	27.84	0.4570	144
acetone	23.70	0.2374	
chloroform	27.14	0.2350	79
tetrahydrofuran	27.31	0.2150	65
propyl bromide		0.2156	54
carbon tetrachloride	26.95	0.1240	66
ethyl acetate	23.97	0.1210	49
methyl propionate	25.06	0.0889	28
benzene	28.88	0.1130	23
methyl ethyl ketone	23.96	0.1040	
methyl <i>n</i> -butyrate	25.19	0.0429	20
toluene	28.52	0.0342	19
1,1,2-trichloroethane	34.70	0.0228	28
methyl isobutyl ketone	23.90	0.0187	14
tetrachloroethylene	31.74	0.0199	23
<i>m</i> -xylene	29.02	0.0107	17
styrene	32.00	0.0086	15
dichlorobenzene		0.0007	35

Since the primary factor inhibiting film leveling is the rapid evaporation of solvent, it is possible to define the ratio λ of the fluid “leveling” time, τ_{level} , to the solvent evaporation time, τ_{evap} , as a measure of the competition between these processes ($\lambda = \tau_{level} / \tau_{evap} \propto E$ where E is the solvent evaporation rate). Since E at any spin speed tracks P_{vp} , it is clear that the film leveling tendency, as embodied in λ , decreases with increasing P_{vp} . Consequently, films created with more volatile solvents will be rougher due to flow instabilities, coupled to the inability of the resulting film surface to level fast enough before it becomes “frozen” into a dried state having a very long viscoelastic relaxation time. These findings are consistent with the experimental results shown in Figure 2.5.

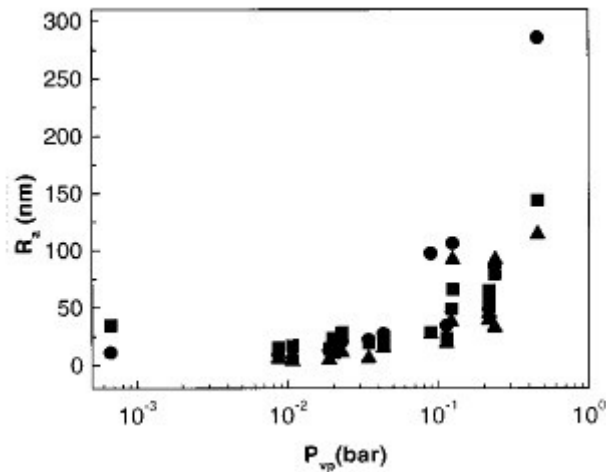


Figure 2.5: Average film roughness, R_a , as a function of solvent vapor pressure, P_{vp} for films spin cast at 200 rpm: triangles, PEMA; squares, PS-200; circles, PS-1000.

The neat and hybrid materials synthesized as thin films in this PhD study were spin-coated using a “Speciality Coating Systems model P6700 series” spin-coater on a substrate (normally Si wafer or glass slides) using a good solvent (toluene) for both the blocks of the PS-*b*-PEO copolymer controlling the roughness and the thickness of the film tuning the spinning speed of the rotating plate.

2.5 Profilometry

A diamond stylus is moved vertically in contact with a sample and then moved laterally across the sample for a specified distance and specified contact force. A profilometer can measure small surface variations in vertical stylus displacement as a function of position. A typical profilometer can measure small vertical features ranging in height from 10 nanometers to 1 millimeter. The height position of the diamond stylus generates an analog signal which is converted into a digital signal stored, analyzed and displayed. The radius of diamond stylus normally ranges from 20 nanometers to 25 μm , and the horizontal resolution is controlled by the scan speed and data signal sampling rate.

In order to measure the thickness of the thin films it was necessary to create a neat step between the investigated materials and the substrate as shown in Figure 2.6.

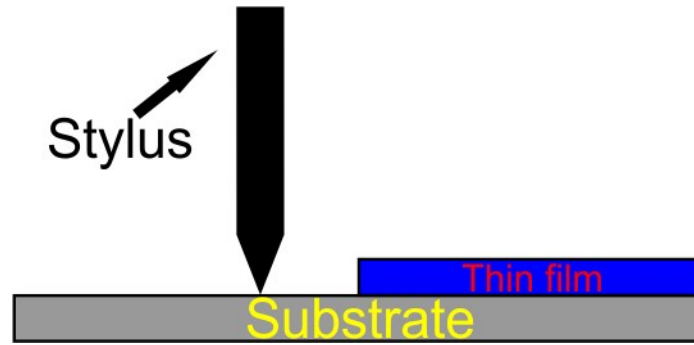


Figure 2.6: Schematic representation of the profilometric measurements performed over the neat block-copolymer or the hybrid materials thin films.

Once that thin films were spin-coated homogeneously all over the surface of the Si wafer, one-half of the substrate covered by the neat or hybrid nanocomposite was cleaned out using acetone thus creating a well-defined step.

All the profilometric measurements were obtained using a “DEKTAK³ – Surface Profile Measuring System” fabricated by Sloan Technology, a subsidiary division of Veeco Instruments Inc. This equipment was located at the “Facultad de Óptica y Optometría de la Universidad de Santiago de Compostela” in Spain. This instrument is a surface texture measuring system, which could analyze the vertical surface profile of the sample: its roughness, waviness and step height. Measurements were made electromechanically by moving the sample beneath a diamond-tipped stylus (12.5 μm standard radius). Dektak³ provided accurate height measurements with vertical resolution of 5 Å in a long lateral scan range of 50 μm to 30 mm. The instrument combined a measurement accuracy of 10 Å, 1σ step height repeatability, enabling precise measurements of thin films thickness below 100 Å. The machine was supplied with a color video camera and provided both the real time viewing of the scan in progress and saving a video image of the analyzed surface for further reference.

The analysis of thin film surface with the profilometer allowed also evaluating the arithmetic average value of roughness R_a defined by equation:

$$R_a = \frac{1}{n} \sum_{i=1}^n |y_i|$$

Where n is the number of the equally spaced points along the trace and y_i is the vertical distance from the mean line to the i^{th} data point of the stylus trace.

2.6 Preparation process of neat and hybrid materials

The strategic approach employed to obtain well reproducible nanostructured thin films with large specific area is summarized in Figure 2.7. The intermediate steps used for the preparation of hybrid nanostructured BCP thin films including the metal precursor inside the PEO domains are also illustrated. The step A of Figure 2.7 depicts the case in which the pure PS-*b*-PEO block copolymer solutions (1 wt % dissolved in toluene) was spin-coated at 2500 rpm for 30 seconds onto inert support (Si wafer or glass slides) at room temperature. PEO cylinders were oriented with axes perpendicular to the film surface embedded in a nearly hexagonal array in the PS matrix.

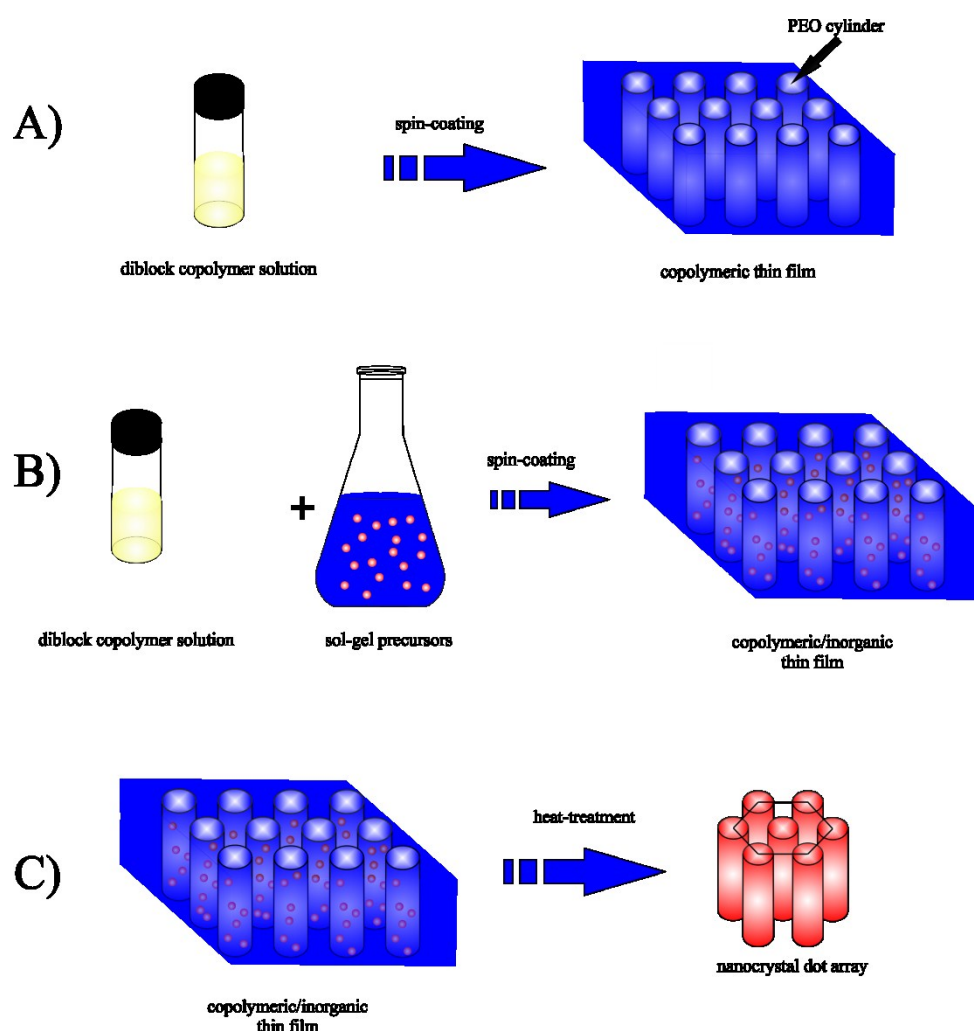


Figure 2.7: Schematic representation of the thin-films preparation process. A): Alignment of the block-copolymer domains due to self-assembly with PEO cylinders all vertical. B): Preparation process of BCP hybrid nanocomposite filled with metal oxides precursor. C): Heat-treatment of the so-obtained nanocomposites and consequent obtainment of metal oxides nanoparticles in a hexagonal array reminiscent of the hexagonal nanostructure of hybrid nanocomposite at step B.

The step B represents the preparation method of the thin hybrid films obtained by the mixing of a solution containing of the alkoxide precursor to the BCP solution and the successive spin coating. The sol-gel was prepared by mixing isopropyl alcohol (IPA), titanium tetraisopropoxide (TTIP, 97% purchased from Aldrich) or niobium ethoxide (99.95% trace metals basis purchased from Aldrich), and H₂O. Solution were prepared at concentration 0.0125 M of metal oxide precursor (TTIP or Nb ethoxide), 0.0125 M of water using a mixed solvent in 1:1 vol/vol ratio of toluene and isopropanol. Subsequently, toluene was dropped slowly into the homogeneous mixture of the sol-gel and stirred for 1 h. Afterward, the desired amount of sol-gel was added to the block copolymer solution and stirred for 30 min. The hybrid solutions were spin coated at 2500 rpm for 30 seconds onto inert support (Si wafer or glass slides) at room temperature.

The so-obtained nanocomposites were then annealed at 600 °C at a rate of 2 °C min⁻¹ and were kept at that temperature for 4 hours to eliminate completely the organic matrix (step C of Figure 2.7) using a horizontal tube furnace (Carbolite[®]).

An hexagonal array of metal oxides nanoparticles was obtained reminiscent of the nanostructure of hybrid nanocomposites achieved at step B.

Bibliography of Chapter II

1. Szwarc, M., Levy, M. & Milkovich, R. *J. Am. Chem. Soc.* **1956**, *78*, 2656
2. Wilhelm, M., Zhao, C., Wang, Y., Xu, R., Winnik, M. A., Mura, J., Riess, G. & Croucher, M. D., *Macromolecules* **1991**, *24* 1033
3. Quirk R.P., Kim J., Kausch C.T., Chun M. *Polym Int* **1996**; *39*, 3.
4. L.J., Fetters; D.J., Lohse, D., Richter; T.A., Witten; A., Zirkel, *Macromolecules* **1994**, *27*, 4639.
5. W. Chen, C. Y. Li, J. X. Zheng, P. Huang, L. Zhu, Q. Ge, R. P. Quirk, B. Lotz, L. Deng, C. Wu, E. L. Thomas, S. Z. D. Cheng, *Macromolecules* **2004**, *37*, 5292-5299.
6. J. S. Trent, J. I. Sceinbeim, P. R. Couchman, *Macromolecules* **1983**, *16*, 589-598.
7. Strawhecker K. E., Kumar S. K., Douglas J.F., Karim A. *Macromolecules* **2001**, *34*, 4669–72.

CHAPTER III

Ordering of nanostructured BCP based hybrid thin films over large areas

3.1 Characterization of the neat block copolymer (SEO)

3.1.1 Thermal analysis

In Figure 3.1 the DSC thermogram recorded during the first and second heating scans and crystallization scan of as-synthesized PS-*b*-PEO copolymer is reported.

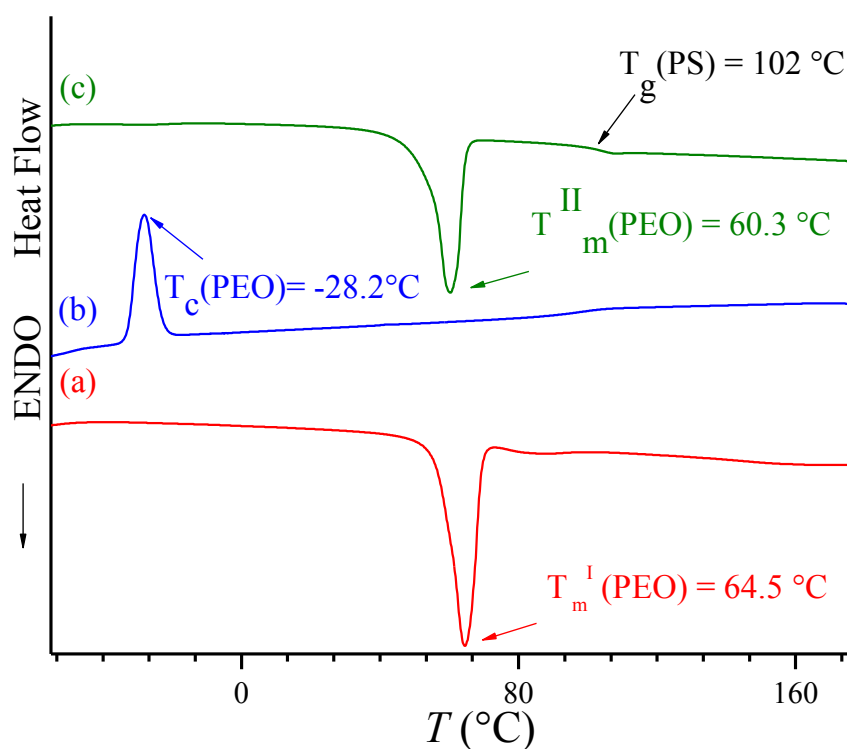


Figure 3.1: DSC thermogram of first heating (a), crystallization (b) and second heating (c) of as prepared PS-*b*-PEO copolymer sample registered at the scanning rate of $10^{\circ}\text{C}/\text{min}$.

An endothermic peak is present at T_m^I of 64.5°C (first melting) and T_m^{II} of 60.3°C (second melting) due to the melting of the crystalline block of PEO (curves a and c of Figure 3.1) and

an exothermic peak due to the crystallization of the same block at T_c of $-28,2^\circ\text{C}$. The glass transition of PS domains is around 102°C (curve c of Figure 3.1).

Generally the temperature of crystallization of the PEO homopolymer is around 40°C .¹ From literature it is known that in PS-*b*-PEO copolymers² the crystallization temperature can be lower than that of the homopolymer. This behavior was found also for a symmetric diblock copolymer, poly(ethylene oxide)-*block*-poly(1,4-butadiene) (PEO-*b*-PB) with PEO and PB being the crystalline and amorphous block, respectively, blended with various amount of a low molecular weight PB homopolymer.^{3,4}

For PEO homopolymer and for a PS-*b*-PEO copolymer where the major component is PEO the crystallization of the melt may be triggered by both homogeneous and heterogeneous nucleation. However, when PEO is the minor component as in our case, the PEO phase will typically crystallize in confined environment due to phase separation of melt. In our case, based on the volume fraction of PEO block equal to $f_{PEO} = 23\%$ (Paragraph 1.3), PEO crystallization is expected to occur inside the cylindrical microdomains of PEO embedded in the PS matrix. The order-disorder transition is expected at temperatures of 160°C for this type of copolymer,^{3,4} and the crystallization of the PEO from this strongly segregated melt occurs after vitrification of the PS matrix. As consequence of microphase separation of PEO blocks in narrow regions we argue that its crystallization temperature at large undercooling is due to homogeneous nucleation since the concentration of heterogeneities is expected to be very low inside the corresponding cylindrical domains.

TGA was used to study the weight loss process of the block copolymer. A single-step weight loss process has been detected for the neat SEO (Figure 3.2). At 350°C the 5% of weight loss was detected. The complete degradation of the copolymer took place at 458°C.

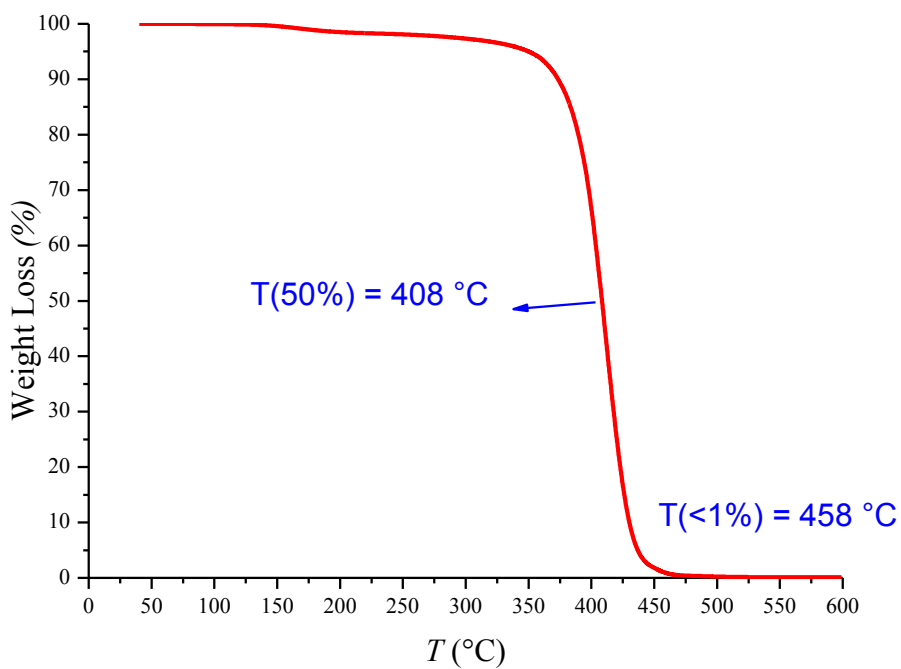


Figure 3.2: TGA curve of SEO copolymer performed in N₂ (g) inert atmosphere.

3.1.2 Wide angle X-ray scattering (WAXS)

The X-ray diffraction pattern of the as-synthesized sample (Figure 3.3) were registered at room temperature.

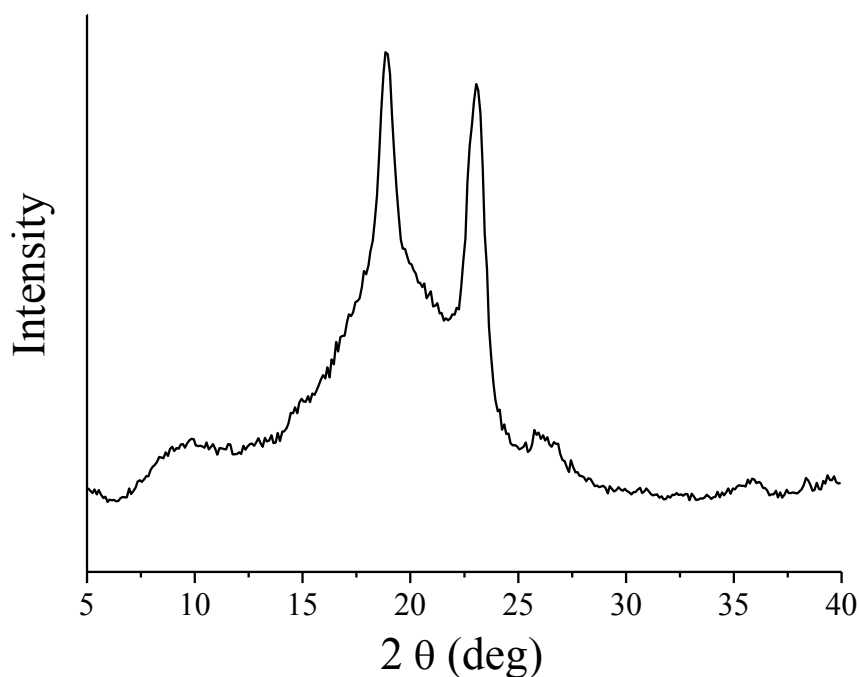


Figure 3.3: X-ray diffraction pattern of the SEO BCP as-synthesized sample at room temperature.

The diffraction pattern showed two distinct peaks centered at $2\theta \approx 19$ and 23° . These peaks are characteristic of polyethylene oxide⁵ and are superposed to the contribution of amorphous phases of PEO and PS blocks.

X-ray diffraction patterns of SEO melt pressed films at different temperatures (Figure 3.4) were conducted to measure its crystallization temperature.

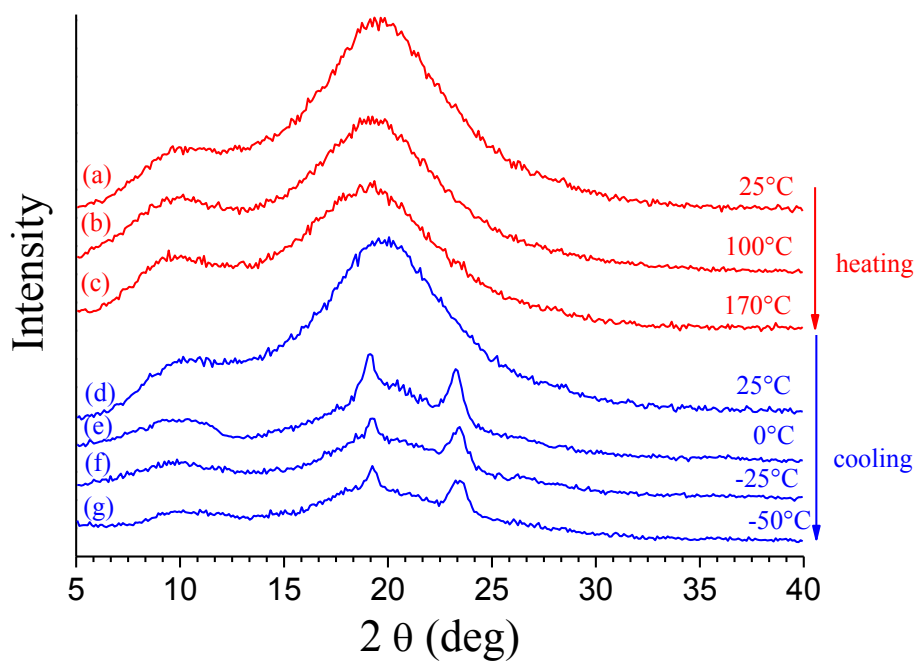


Figure 3.4: X-ray diffraction patterns of melt pressed SEO films collected at different temperatures. In red are depicted the patterns collected during heating up to 170°C; in blue are represented the patterns obtained during cooling.

The X-ray diffraction pattern of melt pressed SEO films does not show any Bragg reflection. PEO block crystallizes instead from melt during cooling in the temperature range comprised between 25 °C and 0°C (curve e of Figure 3.4).

3.1.3 Morphological analysis of the neat SEO

The morphological analysis has been initially performed on the neat PS-*b*-PEO BCP.

Thin films of the neat SEO were obtained using the experimental procedure already described in Paragraph 2.6 (step A).

The AFM phase image of the nanostructured thin film of the sole BCP copolymer is reported in Figure 3.5a. The bright regions correspond to the section of the PEO cylinders oriented with axes perpendicular to the film surface embedded in a nearly hexagonal array in the PS matrix.

This perpendicular orientation of PEO cylinders was obtained by spin-coating toluene solutions of 1 wt% SEO using an inert support of glass. The thickness of the film is controlled to be below 70 nm (evaluated by profilometric measurements) and thus close to the distance between neighboring cylindrical domains (Figure 3.5c).

As reported in literature indeed the thickness of BCP films and the interaction of blocks with the support are key parameters for controlling the orientation of microdomains.⁶

Figure 3.5b shows a three dimensional reconstruction of the bi-dimensional height image where the hydrophilic PEO block are clearly visible as ordered hexagonally packed holes in the hydrophobic matrix.

In the AFM height image PEO domains appear as indented regions (dark in Figure 3.5b) due to their low specific volume in comparison with that of PS block ($V_{sp} \text{ PEO} = 0.67 \text{ cm}^3/\text{g}$, $V_{sp} \text{ PS} = 0.91 \text{ cm}^3/\text{g}$).¹ The arithmetic average roughness (R_a) of these thin films was calculated by profilometry to be $\approx 40 \text{ \AA}$.

The center-to-center distance (d_{C-C}) of neighboring PEO domains is found between 65 and 75 nm and the diameter of the section of cylinders (D) is 39 nm as shown respectively in Figures 3.5c-d where the corresponding distributions are reported.

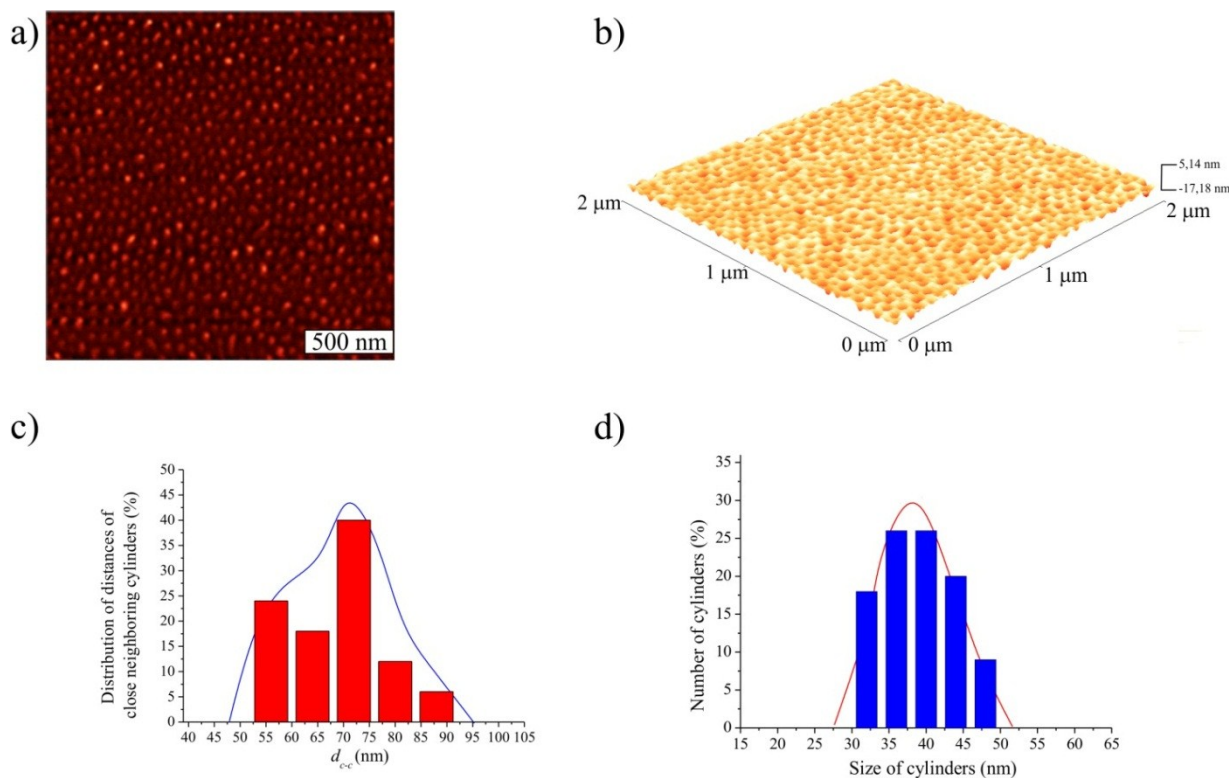


Figure 3.5: a) Bi-dimensional AFM phase image ($2\mu\text{m} \times 2\mu\text{m}$) of the neat SEO obtained by spin-coating at 2500 rpm at room temperature a toluene solution 1wt% BCP onto a glass substrate; b) three-dimensional view obtained from an height AFM image ($2\mu\text{m} \times 2\mu\text{m}$) of the neat SEO copolymer; c) and d) bar diagrams and their fitting curves representing the distribution of distance between center of cylinders and the size of cylinders evaluated from the AFM phase image.

The same values of D and d_{c-c} were detected from the FESEM images of Figure 3.6 at different magnifications where the top section of the PEO cylinders are seen as dark circles in the PS bright matrix. Similar images are obtained over different regions of the same film and on SEO films obtained in independent experiments. This indicates that the cylindrical morphology with PEO cylinders with axes perpendicular to the substrate is obtained over the whole macroscopic area of the films.

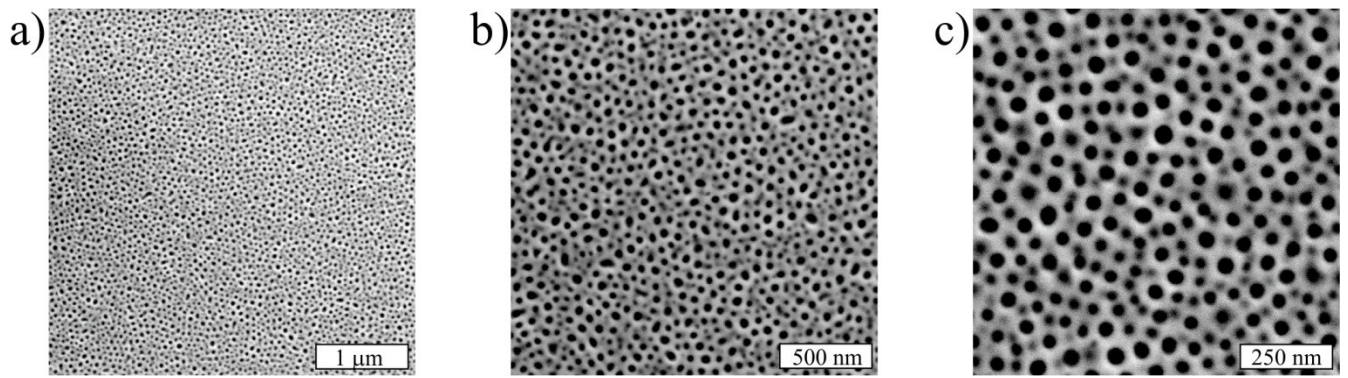


Figure 3.6: FESEM images at different magnifications [a) $4\mu\text{m} \times 4\mu\text{m}$; b) $2\mu\text{m} \times 2\mu\text{m}$ c) $1\mu\text{m} \times 1\mu\text{m}$] of the neat SEO film obtained by spin-coating at 2500 rpm at room temperature a toluene solution 1 wt% BCP onto a Si wafer substrate.

Only near the edges of the support the BCP thin film appeared broken (Figure 3.7a) and even at the boundary these irregularities were difficult to be detected. Therefore the process of spin-coating leads to obtain SEO thin film of uniform morphology all over the macroscopic area of the substrate. It has been possible to obtain the cross-sectional view of the neat copolymer close to the boundary regions (Figure 3.7b). The hydrophilic PEO cylinders appear as perpendicular to the substrate as light-colored columns spanning the whole film thickness.

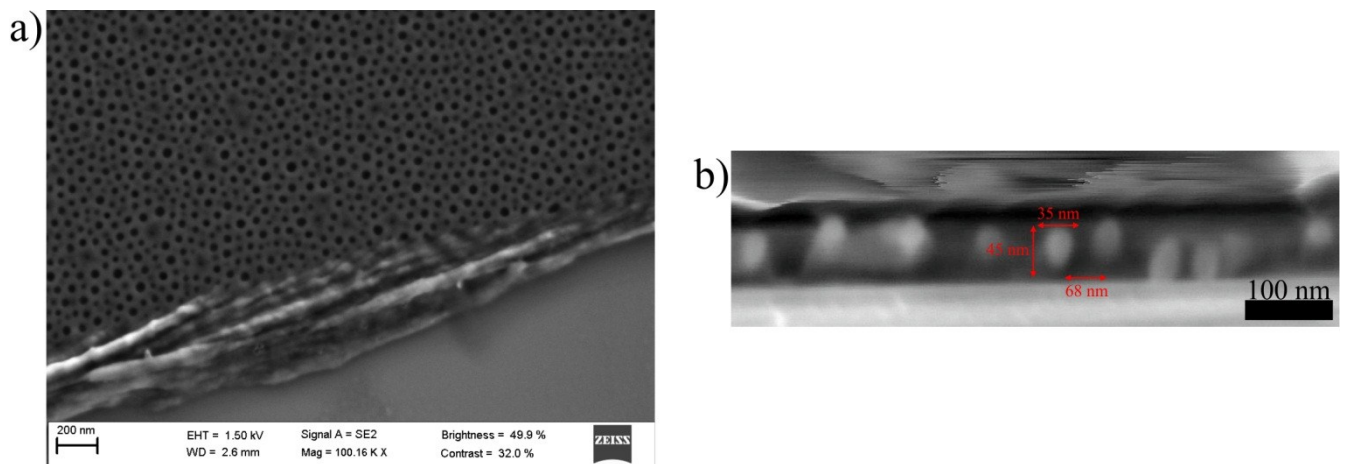


Figure 3.7: a) FESEM image of a SEO film obtained by spin-coating at 2500 rpm at room temperature a toluene solution 1 wt% BCP onto a Si wafer substrate acquired in a region of the thin film close the edges of the support; b) cross-sectional FESEM image of the neat BCP, highlighting the value of the diameter and height of the cylinders and the center-to-center distance of neighboring PEO cylinders.

From FESEM image of Figure 3.7b the value of the diameter of the cylinders ($D \sim 39\text{ nm}$), the dimension of the center-to-center distance between cylinder ($d_{C-C} \sim 68\text{ nm}$) and the height of the cylinders equal to $\sim 45\text{ nm}$ could be measured in close agreement with the values

established from the analysis of the two-dimensional AFM and FESEM images of Figure 3.5 and 3.6.

The thin films of SEO obtained in the same conditions were also analyzed by TEM (Figure 3.8a-c). The grids where the sample was deposited underwent to a *staining* process with RuO_4 as discussed in Paragraph 2.3.1.

According to literature^{7,8} both PS and PEO can be stained via RuO_4 oxidation, and staining of PEO is generally viewed to be easier compared with PS since PEO is more reductive than PS.⁷ In particular it was demonstrated that the staining power of RuO_4 toward PEO and PS blocks is dependent on the environmental conditions of the staining process.⁷ When staining is performed in a less controlled humidity conditions (as in our case), PEO blocks are stained first. When the environment is dry with a low humidity (for example using a dry nitrogen atmosphere), the PS blocks are stained first.

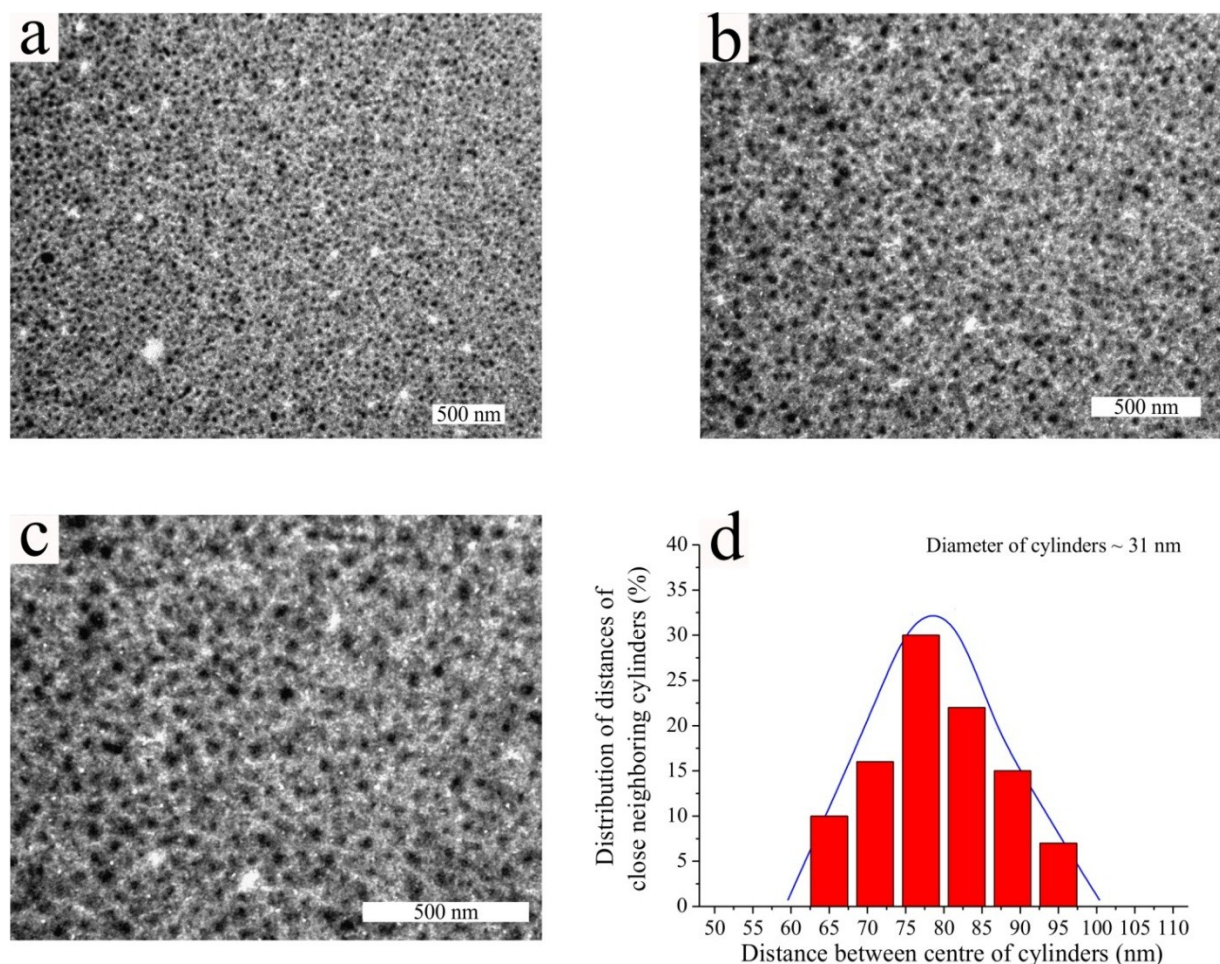


Figure 3.8: TEM images at increasing magnifications (a-c) of the neat SEO film obtained by spin-coating at 2500 rpm at room temperature a toluene solution 1wt% BCP onto a glass substrate and then deposited on copper grids. The sample was RuO_4 stained. d) bar diagram with its fitting curve representing the distribution of distance between center of cylinders evaluated from TEM images. In the conditions adopted during staining (not controlled humidity conditions) PEO domains appear dark.

From analysis of TEM images the diameter of cylinders and the distance between center of cylinders were evaluated resulting only slightly different from the values of these parameters estimated from the AFM and FESEM images of Figures 3.5 and 3.6. The results are reported in Table 3.1.

Table 3.1: Size of the parameters D (diameter of cylinders) and d_{c-c} (centre-to-center distance between cylinders) evaluated from AFM, FESEM and TEM images.

	<i>AFM</i>	<i>FESEM</i>	<i>TEM</i>
<i>D(nm)</i>	39	39	31
<i>d_{c-c}(nm)</i>	70	68	79

3.2 Synthesis and characterization of TiO₂

3.2.1 Applications of TiO₂

Titanium dioxide is used in heterogeneous catalysis, as a photocatalyst, in solar cells for the production of hydrogen and electric energy, as gas sensor, as white pigment (e.g. in paints and cosmetic products), as a corrosion-protective coating, as an optical coating, in ceramics, and in electric devices such as varistors. It is important in earth sciences, it plays a role in the biocompatibility of bone implants, it has potential application as a gate insulator for the new generation of MOSFETS and as a spacer material in magnetic spin-valve systems, and it finds applications in nanostructured form in Li-based batteries and electro-chromic devices.⁹

A better understanding and improvement of catalytic reactions is one main driving force for surface investigations on TiO₂. Because most heterogeneous catalysts consist of small metal clusters on an oxide support, many studies related to growth of metals on TiO₂ were performed. These metal/TiO₂ systems often serve as a model for other metal/oxide surfaces. Traditionally, TiO₂ is a component in mixed vanadia/titania catalysts used for selective oxidation reactions.¹⁰ The surface science of vanadium and vanadia/TiO₂ systems was addressed by several groups.¹¹⁻¹³

TiO₂ is not suitable as a structural support material, but small additions of titania can modify metal-based catalysts in a profound way. The so-called strong-metal support interaction (SMSI) is, at least in part, due to encapsulation of the metal particles by a reduced TiO_x overlayer (see ref. 14 by Haller and Resasco). Recently, this phenomenon was revisited using surface science techniques.¹⁵ The discovery that finely dispersed Au particles supported on TiO₂ and other reducible metal oxides oxidize CO at low temperature¹⁶ has spurred some excitement in the surface science community.

The photoelectric and photochemical properties of TiO₂ are another focus of active research. The initial work by Fujishima and Honda¹⁷ on the photolysis of water on TiO₂ electrodes without an external bias, and the thought that surface defect may play a role in the decomposition of water into H₂ and O₂, has stimulated much of the early work on TiO₂.¹⁸ Unfortunately, TiO₂ has a low quantum yield for the photochemical conversion of solar energy. The use of colloidal suspensions with the addition of dye molecules has been shown to improve efficiency of solar cells, and has moved TiO₂-based photoelectrochemical converters into the realm of economic competitiveness.¹⁹

By far, the most actively pursued applied research on titania is its use for photo-assisted degradation of organic molecules. TiO_2 is a semiconductor and the electron–hole pair that is created upon irradiation with sunlight may separate and the resulting charge carriers might migrate to the surface where they react with adsorbed water and oxygen to produce radical species. These attack any adsorbed organic molecule and can, ultimately, lead to complete decomposition into CO_2 and H_2O . The applications of this process range from purification of wastewaters,²⁰ disinfection based on the bactericidal properties of TiO_2 ²¹ (for example, in operating rooms in hospitals), use of self-cleaning coatings on car windshields²² to protective coatings of marble (for preservation of ancient Greek statues against environmental damage).²³ It was even shown that subcutaneous injection of a TiO_2 slurry in rats, and subsequent near-UV illumination, could slow or halt the development of tumor cells.²⁴

Semiconducting metal oxides may change their conductivity upon gas adsorption. This change in the electrical signal is used for gas sensing.²⁵ TiO_2 is not used as extensively as SnO_2 and ZnO , but it has received some attention as an oxygen gas sensor, e.g. to control the air/fuel mixture in car engines.²⁶

The sheer volume of TiO_2 pigments produced world-wide—currently ca. 4 million tons per year — is stunning. TiO_2 pigment is used in virtually every kind of paint because of its high refractive index. (see Table 3.2 for a summary of the values of the refractive indexes). The surface properties play a role even in these wide-spread applications, e.g. the photocatalytic degradation of binder in paints is a major problem for the paint industry. TiO_2 is non-toxic and safe, and can be dispersed easily. In pure form it is also used as a food additive,²⁷ in pharmaceuticals, and in cosmetic products.²⁸

Table 3.2: Maximum, medium and minimum values of refractive index (n_g , n_m and n_p), of the different mineral forms of titanium dioxide.

Refractive index			
	n_g	n_m	n_p
α-TiO_2 (rutile)	2.908	–	2.621
β-TiO_2(anatase)	2.488	–	2.561
γ-TiO_2(brookite)	2.7004	2.5843	2.5831
TiO_2 (rutile)	2.9467	–	2.6506
TiO_2(anatase)	2.5688	–	2.6584
TiO_2(brookite)	2.809	–	2.677

Titanium dioxide is used extensively in thin-film optical-interference coatings.²⁹ Such coatings are based on the interference effects between light reflected from both the upper and lower interface of a thin film (the same effect gives rise to the different colors of an oil film on water). The relative ratios between transmission and reflection of light are governed by the index of refraction of the thin film and the surrounding media. By depositing a stack of layers with the appropriate optical index, the refraction/transmission properties of a stack of thin layers on a glass substrate can be designed to meet a great number of applications. Examples for such devices include antireflective coatings, dielectric mirrors for lasers, metal mirrors with enhanced reflection, and filters. For most films a combination of materials with indexes as high and as low as possible is an advantage. Titanium dioxide has the highest index of all oxides, making it ideally suited for this application.

One of the issues currently debated in materials science is the search for the best dielectric gate material for replacing SiO₂ MOSFET devices. It appears that the limit for miniaturization, when electric tunneling through ever thinner SiO₂ films becomes significant, will be reached in the very near future. Ultrathin metal oxide films might be well-suited as the gate material of the future, and TiO₂, with its high dielectric constant (Table 3.3), would be an attractive candidate for this application.

Table 3.3: Dielectric properties of the mineral form of rutile considered respect the optical axis and the *c*-axis.

Dielectric properties			
	Frequency (Hz)	Temperature (K)	Dielectric constant
rutile, perpendicular to optical axis	10 ⁸	290–295	86
rutile, parallel to optical axis	–	290–295	170
rutile, perpendicular to <i>c</i>-axis	10 ⁴	298	160
rutile, along <i>c</i>-axis	10 ⁷	303	100

A new kind of gate oxide must meet very stringent requirements—no surface states, virtually pin-hole free, stoichiometric ultrathin films, good interface formation with the Si substrate, etc. TiO₂ could be a viable approach to dielectrics whose oxide equivalent thickness is less than 2.0 nm.

TiO₂ films grown by chemical vapor deposition (CVD) on Si substrate show excellent electric characteristics, but a low resistivity layer, probably because SiO₂, forms at the interface.³⁰ Interestingly, modified TiO₂ films are also promising materials for spintronics applications, although TiO₂ itself is not a magnetic material. When anatase TiO₂ films are doped with a few percent of Co, they become ferromagnetic.³¹ Such films are optically transparent, semiconducting, and ferromagnetic at room temperature, and might be ideal candidates for spin-based electronic devices.

Nanostructured TiO₂ electrodes have received quite a bit of attention. One particularly interesting application is the implementation of nanocrystalline TiO₂ films in electrochromic devices.³² Such devices control light transmission in windows or light reflection in mirrors and displays. They are based on two complementary electrodes (TiO₂ and WO₃), which change their color upon reduction/oxidation cycles induced by an electrical current.

3.2.2 The structure of TiO₂ surfaces

The relationship between atomic surface structure and other physical and chemical properties is probably one of the most important achievements of surface science. Because of the mixed ionic and covalent bonding in metal oxide systems, the surface structure has an even stronger influence on local surface chemistry as compared to metals or elemental semiconductors.³³

A great amount of work has been performed on TiO₂ over the years, and has led to an understanding that is unprecedented for a metal oxide surface.

Titanium dioxide crystallizes in three major different structures; rutile (tetragonal, D_{4h}¹⁴-P4₂/mm, a=b=4.584 Å, c=2.953 Å)³⁴, anatase (tetragonal, D_{4h}¹⁹-I4₁/amd, a=b=3.782 Å, c=9.502 Å) and brookite (rhombohedral, D_{2h}¹⁵-Pbca, a=5.436 Å, b=9.166 Å, c=5.135 Å).³⁵

Other structures exist as well, for example, cotunnite TiO₂ has been synthesized at high pressures and is one of the hardest polycrystalline materials known. However, only rutile and anatase play any role in the applications of TiO₂ and are of any interest here as they have been studied with surface science techniques. Their unit cells are shown in Figure 3.9. In both structures, the basic building block consists of a titanium atom surrounded by six oxygen atoms in a more or less distorted octahedral configuration. In each structure, the two bonds between the titanium and the oxygen atoms at the apices of the octahedron are slightly longer. A sizable deviation from a 90° bond angle is observed in anatase. In rutile, neighboring octahedra share one corner along $\langle 1\ 1\ 0 \rangle$ — directions, and are stacked with their long axis alternating by 90°. In anatase the corner-sharing octahedra form (0 0 1) planes. They are

connected with their edges with the plane of octahedra below. In all TiO_2 structures, the stacking of the octahedra results in threefold coordinated oxygen atoms.

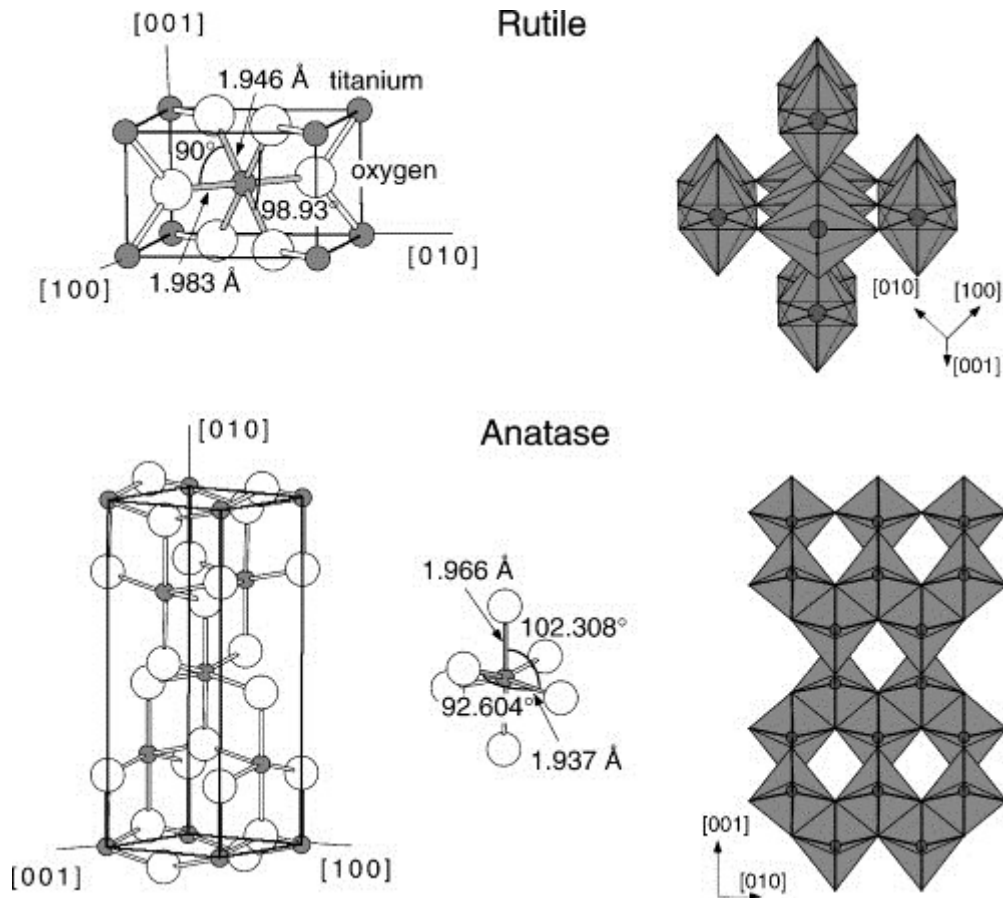


Figure 3.9: Bulk structures of rutile and anatase. The tetragonal bulk unit cell of rutile has the dimensions, $a=b=4.587 \text{ \AA}$, $c=2.953 \text{ \AA}$, and the one of anatase $a=b=3.782 \text{ \AA}$, $c=9.502 \text{ \AA}$. In both structures, slightly distorted octahedra are the basic building units. The bond lengths and angles of the octahedrally coordinated Ti atoms are indicated and the stacking of the octahedra in both structures is shown on the right side.

Rutile TiO_2 single crystals are widely available. They can be bought in cut and polished form from companies (such as Commercial Crystal Laboratories, USA; Kelpin Kristallhandel, Germany; Goodfellow, UK; Earth Jewelry, Japan and many others). A very small roughness is achieved by grinding the sample, and then polishing the surface for many hours with a chemo-mechanical treatment. This is also referred to as epitaxial polish.³⁶

Ramamoorthy and Vanderbilt³⁷ calculated the total energy of periodic TiO_2 slabs using a self-consistent ab initio method. The (1 1 0) surface has the lowest surface energy, and the (0 0 1) surface the highest. This is also expected from considerations of surface stability, based on electrostatic and dangling-bonds arguments. The thermodynamic stability of the (1 0 0)

surface was also considered, and was found to be stable with respect to forming (1 1 0) facets. The (0 0 1) surface was almost unstable with respect to the formation of macroscopic (1×1) (0 1 1) facets. From the calculated energies a three-dimensional (3D) Wulff plot was constructed (see Figure 3.10). The Wulff construction³⁸ gives the equilibrium crystal shape of a macroscopic crystal. For comparison with experimental crystal shapes one has to take into account that only four planes were considered and that the calculations are strictly valid only at zero temperature.

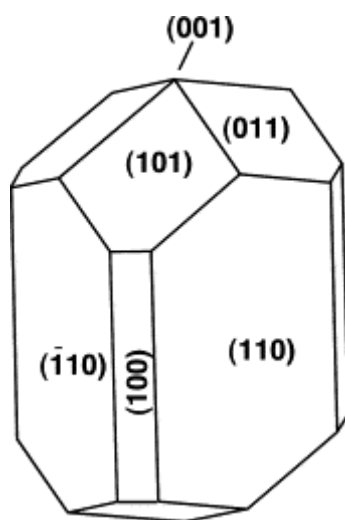


Figure 3.10: The equilibrium shape of a macroscopic TiO_2 crystal using the Wulff construction.³⁷

The experimental results on the three low-index rutile surfaces fit rather well with the stability expected from these calculations. For rutile, the (1 1 0), (0 0 1) and (1 0 0) surfaces have been studied, with (1 1 0) being the most stable one. For anatase, the (1 0 1) and the (1 0 0)/(0 1 0) surface planes are found in powder materials, together with some (0 0 1). The (1 0 1) surface was calculated to have the lowest surface energy, even lower than the rutile (1 1 0) surface.³⁹

3.2.3 Nanostructured TiO_2

The current international trend to synthesize, characterize, and investigate ‘nano’ materials has also involved TiO_2 . This material lends itself quite well to building tiny structures in all sorts of sizes and shapes. Such nano- TiO_2 is typically produced in a sol-gel process, where a titanium alkoxide or halide (TiCl_4 , TiF_4) is hydrolyzed, often in the presence of a template such as nano-spheres, nano-rods or anodic porous alumina.⁴⁰⁻⁴²

The structures that have been made present different shape: nano-rods, whiskers, wires, spheres, ordered holes. For example perfectly ordered TiO_2 ‘nano-whiskers’, i.e., flat anatase platelets a few nanometer wide and several tens of nanometer long, were produced by Zhu and Ding.⁴³ In this case, the selective coordination of acetate groups on specific lattice planes was invoked to account for the oriented growth.

Another beautiful construction are hollow TiO_2 ‘microspheres’, ca. 20 μm in diameter with a wall only a few tens of nanometer thick, synthesized by Iida et al.⁴⁴

Yin et al.⁴⁵ have succeeded in obtaining hollow spheres of TiO_2 with the inner surface coated with Ag nanoparticles. It was shown that these nanoparticles could then be etched, leaving nanoholes inside TiO_2 microspheres (as shown in Figure 3.11).

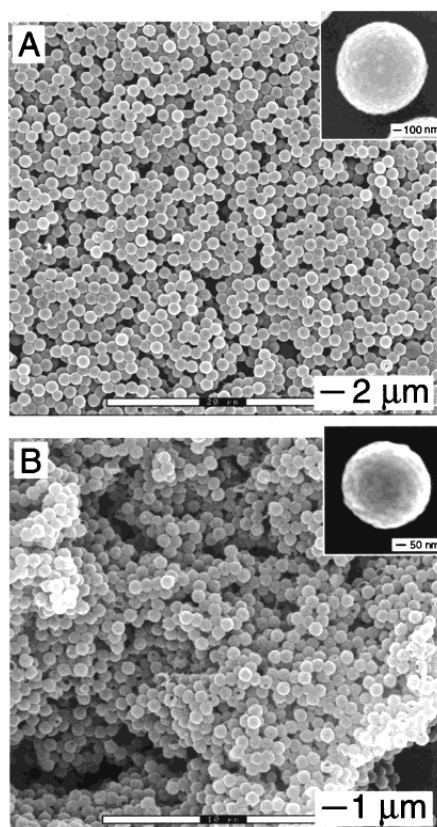


Figure 3.11: SEM images of some as-synthesized hollow spheres of titania that were generated by templating the sol-gel precursor solution against a crystalline array of (A) 1- μm and (B) 0.38- μm PS beads whose surfaces had been prederivatized with nanoparticles of silver. In these two samples, the percentages of broken hollow spheres were <5%. The thickness of the ceramic wall for these two samples was ~50 and ~30 nm.

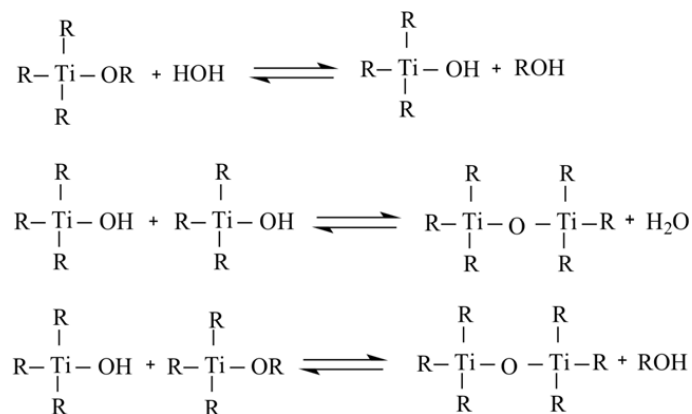
It was speculated that these structures could be used as extremely tiny containers for encapsulation in the delivery of drugs or the protection of biologically active agents. Or one could dream as these spheres becoming the tiniest ‘microreactors’ for catalytic reactions.

The formation of periodic arrangements of nanostructured TiO₂ can also be achieved. For example, the formation of a zeolite-like mesoporous materials has been accomplished for TiO₂ and other metal oxides.⁴⁶⁻⁴⁷ Such high-surface area materials could be interesting for catalytic applications or in photonics.

Another possible scenario that has been developed during last years is the preparation of thin films with a self-organized nanostructure using the self-assembly capability of block copolymer templates that will be discussed more extensively in the following paragraphs.

3.2.4 Synthesis and characterization of TiO₂

Sol-gel synthesis has been chosen as the chemical technique to prepare titania nanoparticles. The most commonly used precursors for sol-gel synthesis are alkoxides. In this study, titanium tetraisopropoxide (TTIP, 97% purchased from Aldrich) was used as precursor in sol-gel synthesis for generating titanium dioxide nanoparticles, due to high chemical activity of the M-OR bond, which allows facile tailoring in situ during synthesis, as shown in Scheme 3.1.



Scheme 3.1: Precursor reactions in the sol-gel process: hydrolysis, alcohol condensation and water condensation.

The choice of the sol-gel technique to fabricate TiO₂ was due to the possibility to prepare active inorganic phases with a high control of purity, composition, microstructure and textural properties of the final material. The sol-gel was prepared mixing isopropanol, TTIP and

deionized water (in a molar ratio 1:1). In our procedure we have not used any acid catalyst such as HCl to accelerate the hydrolysis reactions. Indeed, according to literature,⁴⁸ use of concentrated solutions of HCl beside of accelerating the hydrolysis of TTIP, slows down the polycondensation process of TiO₂ precursor while decreasing the quality of solvent toward the PS component of the BCP. This may result in formation of micellar entities, consisting of PS cores surrounded by PEO chains in the corona. Therefore the synthetic procedure adopted in the present study for sol-gel synthesis of TiO₂ prevents formation of micellar entities, without hindering formation of TiO₂ nanoparticles. To this aim 0.0125 M solutions of TTIP were prepared using toluene/isopropanol mixed solvent in 1:1 vol/vol ratio. The resultant TTIP solution was bright light-yellow. It was left under stirring for 1 day, observing no precipitation. Samples for XRD measurements were prepared by adding a few drops of the solution onto microscope slides, allowing the solution to dry under ambient conditions. Then the films were heat-treated in air at 100, 200, 400°C for 4 h with an identical ramp of 4 °C/min. In Figure 3.12 the diffraction patterns of the films treated at 200 and 400°C are shown.

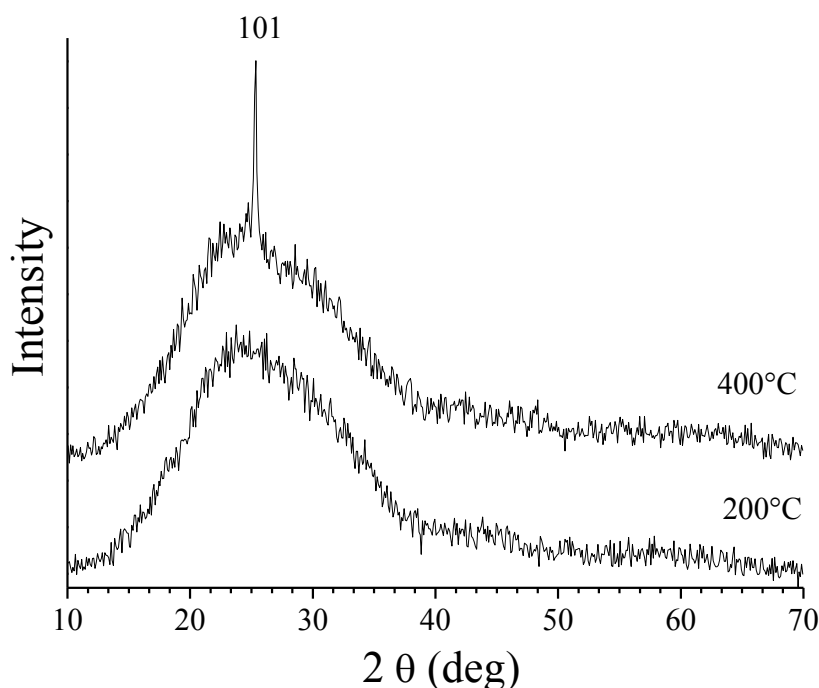


Figure 3.12: X-ray diffraction patterns of TiO₂ cast films heat-treated at 200 and 400°C for 4 h.

For the heat-treated films at 200°C no specific diffraction peak is noticed except from the amorphous halo centered at $2\theta = 25^\circ$ due to the glass slide support whereas at 400°C an intense Bragg peak appears at $2\theta \approx 25^\circ$ corresponding to 101 reflection of anatase.

The solution containing the titania precursor was dried in air leaving a white powder. The powders were treated at different temperatures in consecutive annealing steps of 4 h at 100, 400, 600, 800 °C. The X-ray powder diffraction profiles of these samples are reported in Figure 3.13.

The average size of crystallites was calculated from the width at the half-height B of the 101 Bragg peak of anatase and 110 Bragg peak of rutile, using the Sherrer equation:⁴⁹

$$t = \frac{k \lambda}{B \cos \Theta}$$

where k is a shape factor of the particle (it is 1 if the spherical shape is assumed), λ and Θ are the wavelength and the diffraction angle of the peak, respectively. No correction for instrumental broadening was performed in the use of Sherrer formula. The peak width was measured at half of the maximum intensity.

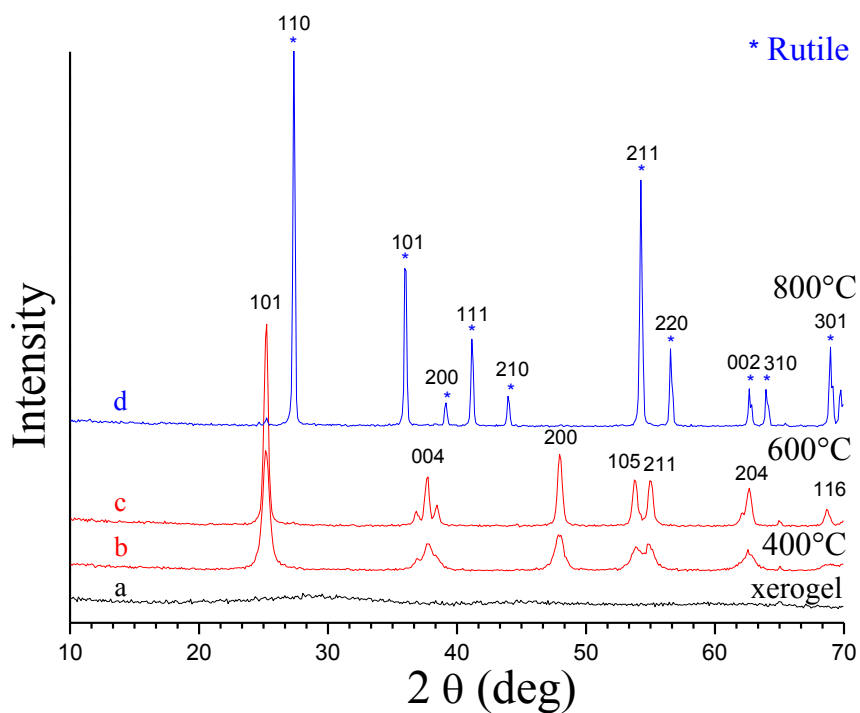


Figure 3.13: X-ray diffraction patterns of TiO₂ powders heat-treated at different temperatures for 4 h.

The dried powders (xerogel) did not show any crystallization peak (curve a of Figure 3.13). At 400°C the reflections of anatase are apparent (curve b of Figure 3.13). The anatase polymorph remains stable also upon successive annealing at 600°C (curve c of Figure 3.13). The average size of anatase crystals in the direction normal to (101) planes is 13.5 nm at 400°C and increases up to 21.6 nm at 600°C.

Phase transformation of anatase to rutile is obtained at 800°C (curve c of Figure 3.13) by narrowing of Bragg peaks.. In fact at 800°C the phase transformation from anatase to rutile is almost complete whereas the crystal size in the direction normal to (110) plane of rutile is 42.8 nm.

The differential thermal analysis measurement (DTA) of the xerogel showed two exothermic peaks at 267 °C and 375 °C in Figure 3.14. The peaks are attributed to the combustion of organic compounds and the phase transitions of amorphous to crystalline brookite (at ≈ 267 °C) and brookite to anatase (at ≈ 375 °C). As indicated by Liu,⁵⁰ the phase transitions of amorphous phase to anatase may have also occurred because the exothermic peak is not sharp.

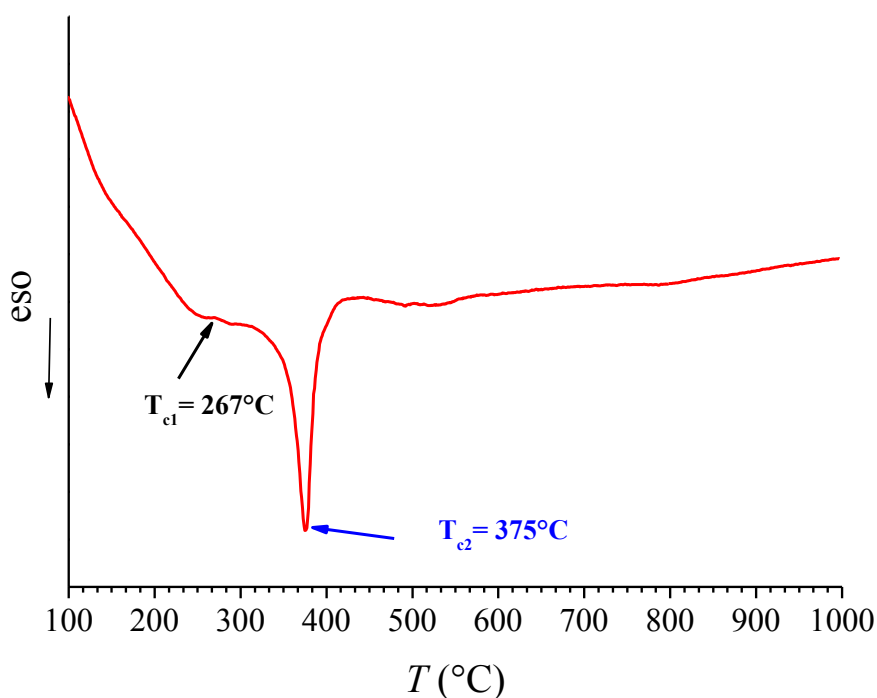


Figure 3.14: DTA curve of xerogel recorded in air from room temperature up to 1273 K at a heating rate of 10 K min⁻¹.

The results of FTIR spectroscopic measurements of xerogel and of the samples annealed at different temperatures are shown in Figure 3.15. From the FTIR spectrum of xerogel, it can be concluded that the broad band at about 3260 cm^{-1} is related to the stretching vibration of O-H and -CH- , respectively. The band at 1630 cm^{-1} can be attributed to the bending mode of adsorbed water, but disappears at higher temperatures. The band at about 1430 cm^{-1} is related to the C-O-H bending vibration, which is attributed to the presence of tetraisopropyl titanate.⁵¹ Bands below 800 cm^{-1} are due to the Ti-O and Ti-O-Ti stretching vibration.⁵¹⁻⁵² For the FTIR spectra of the heat-treated powders (starting from 400°C), only the strong band at about 500 cm^{-1} can be observed, which is related to the Ti-O stretching vibration and is in well agreement with the finding of Liu.⁵⁰ From the IR spectra, it can be shown that after heat-treating at 400°C , 600°C and 800°C most of the organic component disappeared, which is in good agreement with the thermal behavior of Figure 3.14.

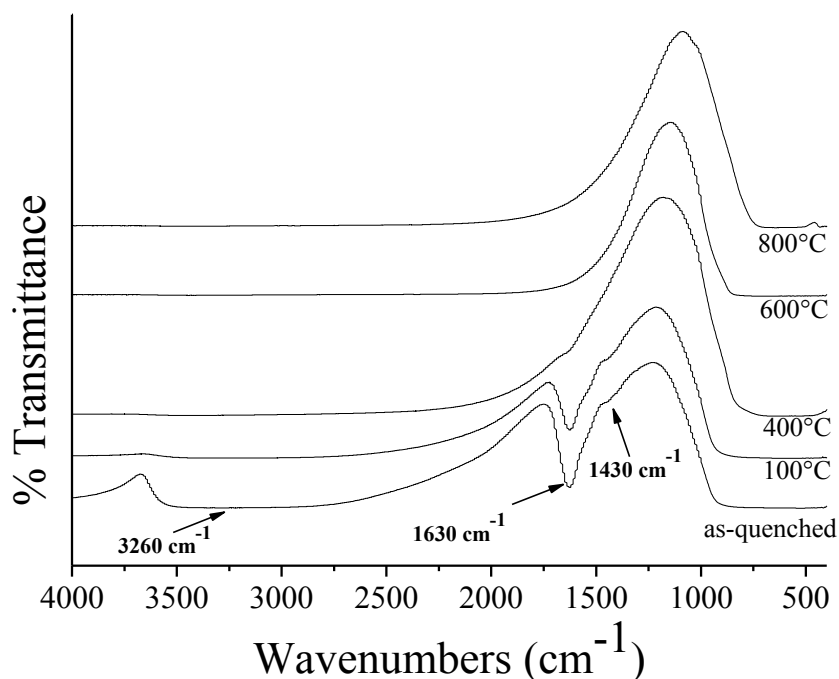


Figure 3.15: FTIR spectra of TiO₂ powders annealed at different temperatures.

3.2.5 Morphological analysis of TiO₂ films obtained from TTIP solution

FESEM analysis was performed on TiO₂ films obtained by spin coating and drop casting TTIP 0.0125 M solutions in toluene/isopropanol 1:1 vol/vol mixed solvent. In Figure 3.16 the FESEM images of the TiO₂ thin films obtained by spin coating the TTIP solution on Si wafer are shown before and after heat treatment at 600°C for 4 h. In both cases a disordered array of TiO₂ nanoclusters was obtained.

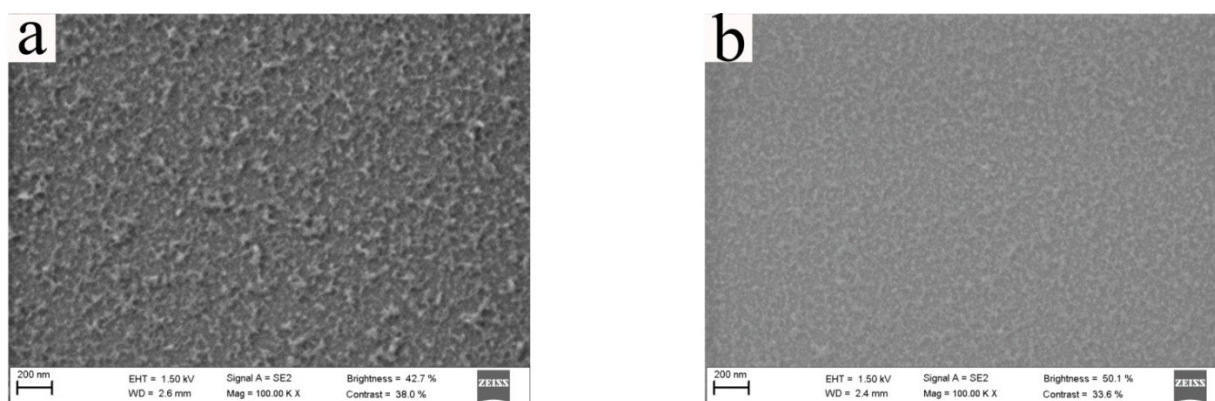


Figure 3.16: FESEM images of thin films of TiO₂ obtained through sol-gel technique by spin-coating TTIP solution at 2500 rpm at room temperature (a) before and (b) after heat-treatment at 600°C for 4h.

The FESEM images of the TiO₂ thin film obtained by drop casting the TTIP solution on Si wafer are shown in Figure 3.17 before and after heat treatment at 600 °C for 4 h. A homogenous layer of TiO₂ with an irregular surface is obtained also in these cases.

The EDX (Energy Dispersive X-ray) microanalysis of TiO₂ film surface of Figure 3.17b was performed in order to obtain information about the elemental composition of the sample.

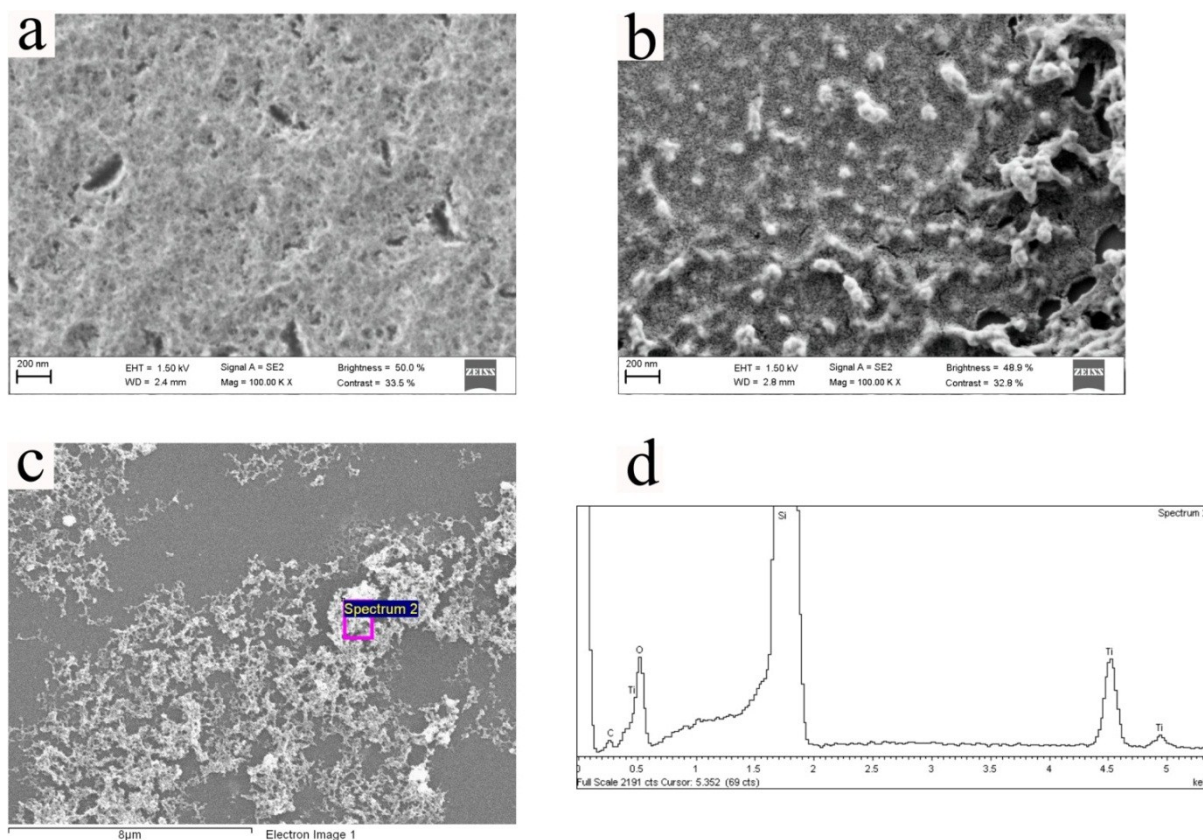


Figure 3.17: FESEM images of thin film of TiO_2 obtained through sol-gel technique by drop casting the TTIP solution on the Si wafer at room temperature before (a) and after (b) the heat-treatment at 600°C for 4 h. EDX spectrum (d) performed on the heat-treated sample over the area included in the rectangle (c).

A characteristic spectrum of X-rays emitted by the specimen (over the area included in the rectangle of $1\ \mu\text{m} \times 1.25\ \mu\text{m}$ of the heat-treated sample shown in Figure 3.17c) after excitation by high-energy electrons was obtained in Figure 3.17d. The intensity of the peaks of EDX spectrum is proportional to the relative concentration of elements on the surface. The position of the peaks indicates the presence of Ti and O of anatase. A strong signal relative to the Si of the support is also present. A little amount of C atoms is also detected due to the presence of unreacted alkoxide precursor.

3.3 Hybrid materials

TiO₂/SEO nanocomposites have been prepared following the method described in Paragraph 2.6. SEO solutions (1 wt% in toluene) were stirred at room temperature for at least 1 h to ensure complete dissolution. Then, the sol–gel was prepared mixing 5000 μ l of isopropanol (IPA), TTIP (0.125 mmol) and H₂O (0.125 mmol). Subsequently, toluene (5000 μ l) was dropped slowly into the homogeneous mixture of the sol–gel and stirred for 1 h. Afterward the desired amount of sol–gel was added to the SEO solution and stirred for 30 min, at concentrations listed in Table 3.4

Table 3.4: TTIP/PEO monomeric unit molar ratio, volume of sol/gel (V_{sg}) added to 500 μ l of toluene solution 1 wt% SEO and volumetric ratio ($\phi_P\%$) in the resultant mixture between the sol/gel containing the TiO₂ precursor and SEO solution evaluated as $V_{sg}/500 \mu$ l.

Solutions	(n TTIP/ n m.u. PEO) %	V_{sg} (μ l)	$\phi_P\% = V_{sg}/V_{SEO}$
A	1	20	4
B	2.5	50	10
C	10	200	40
D	20	400	80
E	40	800	160
F	60	1200	240
G	80	1600	320

The FESEM and AFM images of thin films obtained by spin coating the SEO solution containing 2.5 mol% TTIP are reported in Figure 3.18.

From FESEM and AFM images of Figure 3.18 a and b it is apparent that also the hybrid system is characterized by a pseudo-hexagonal array of PEO cylinders (dark regions) with axes perpendicular to the substrate embedded in the PS matrix (bright regions). The average diameter of cylinders is 32 nm from analysis of FESEM image (Figure 3.18c) and \approx 25 nm from analysis of AFM images (Figure 3.18d). From both images the average value of center-to-center distance between close neighboring cylinders is \approx 66 nm.

This indicates that the morphology of the hybrid system with 2.5 mol% TTIP is not greatly influenced by the support, namely Si wafer for FESEM images, glass for AFM measurements. The values of D and d_{c-c} of the hybrid system of Figure 3.18 were slightly lower than those

observed in the AFM and FESEM images of neat SEO thin films of Figure 3.5 and 3.6 that were equal to 39 in both cases.

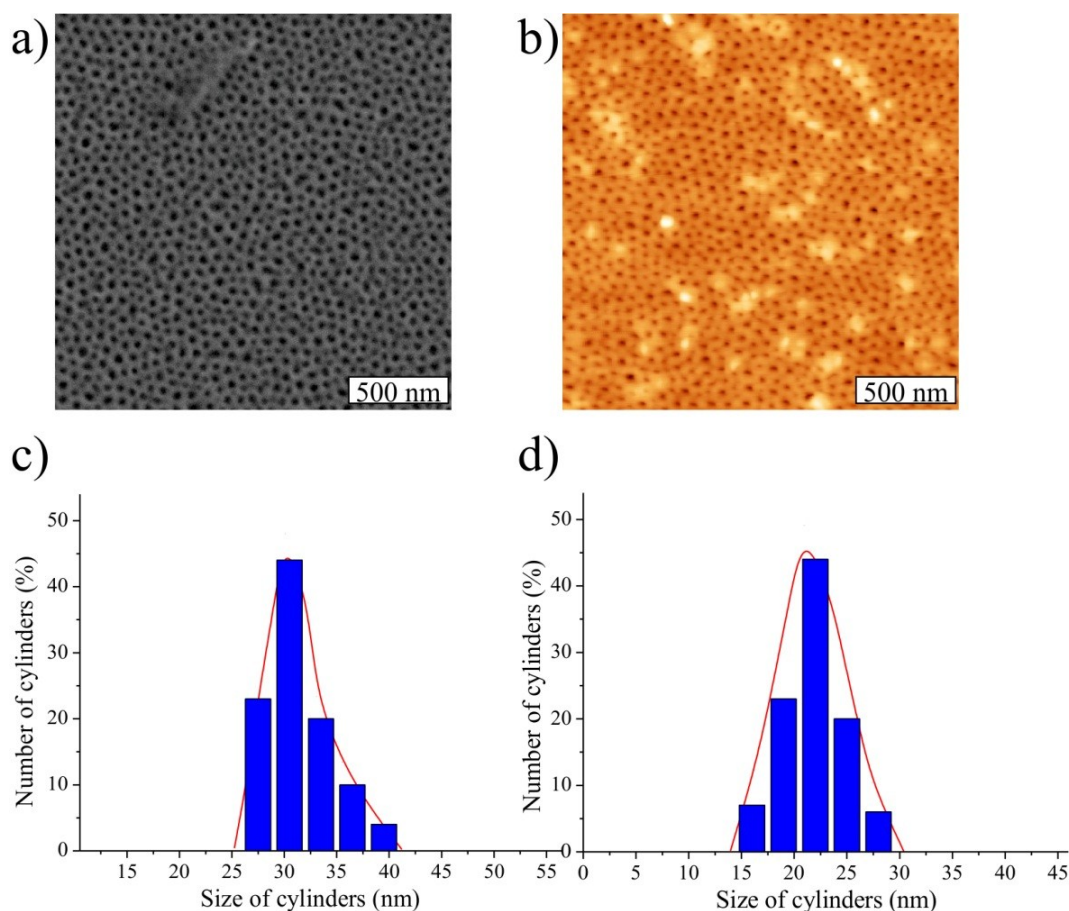


Figure 3.18: FESEM (a) and AFM (b) height images of thin films of SEO with the 2.5 mol% TTIP obtained by spin-coating at 2500 rpm at room temperature. Distribution of diameter of cylinders obtained from analysis of FESEM a and AFM b images (c and d respectively).

TEM images of the sample with the same content of the titania precursor are shown in Figure 3.19 at two different magnifications.

Whereas for the neat PS-*b*-PEO it was necessary to expose the organic block copolymer to the vapors of RuO₄ to enhance the contrast between PEO and PS domains, in the case of hybrid system the presence of the inorganic network provides high contrast of the hydrophilic PEO domains, that appear dark in the bright PS matrix. The fact that PEO domains appear dark is due to the high electron density achieved by selective inclusion of TiO₂ precursor.⁵³

The diameter of the dark regions was ≈ 24 nm (as shown in Figure 3.19c) that matches quite well with the dimensions of the top section of the diameter of cylinders of PEO domains of

2.5 mol% TTIP hybrid nanocomposite calculated from the AFM and FESEM images of Figure 3.18. The measured value of d_{c-c} was 66 nm.

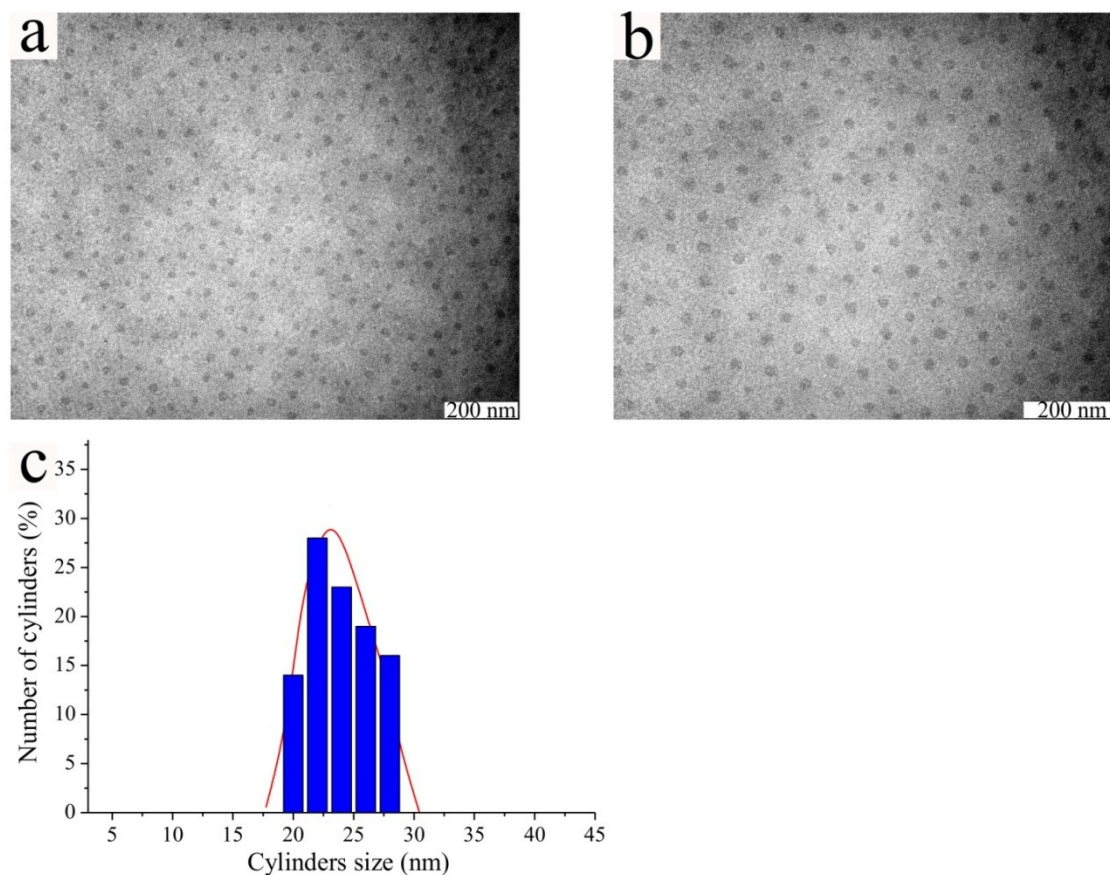


Figure 3.19: TEM images at different magnifications (a,b respectively) of the hybrid thin film with 2.5 mol% of TTIP obtained by spin-coating the solution B of table 3.14 at 2500 rpm at room temperature. Spin coating was performed on the copper grids. c) bar diagram with its fitting curve representing the distribution of diameter of cylinders calculated from TEM images.

The FESEM image of hybrid SEO system containing different concentration of TiO_2 precursor are shown in Figure 3.20. In all cases a morphology reminiscent of the cylindrical morphology of neat SEO (Figures 3.5 and 3.6) is obtained regardless of content of TiO_2 precursor. Dark spots can be still interpreted as due to PEO domains characterized by selective inclusion of TiO_2 precursors. The average diameter of PEO domains D has been calculated by averaging over at least one hundred measurements of diameter of dark spots taken over different regions of the same FESEM image and over different FESEM images of the same sample. The so calculated valued of D are reported in Figure 3.20h.

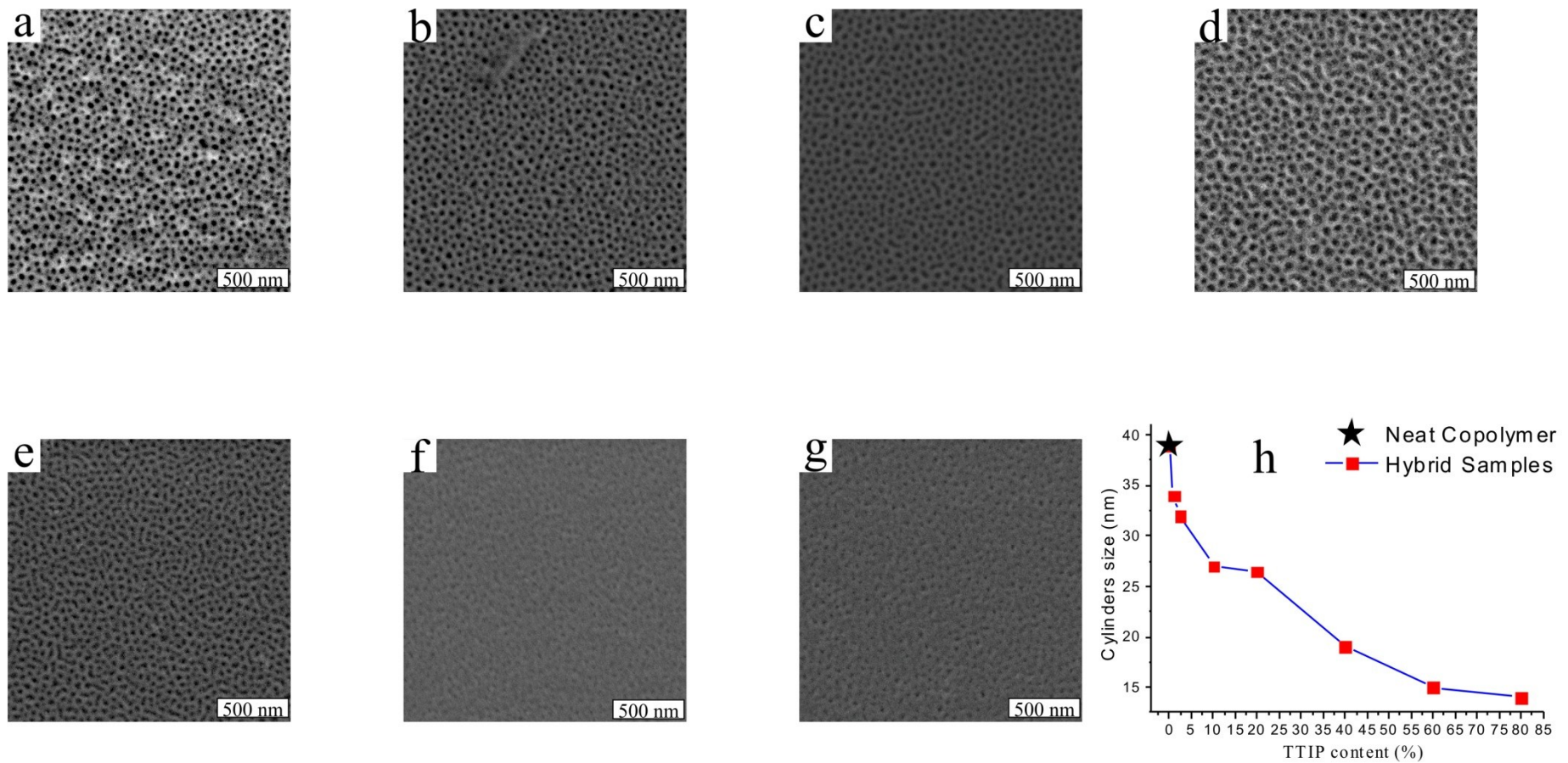


Figure 3.20: FESEM images ($2\mu\text{m} \times 2\mu\text{m}$) of the hybrid SEO samples obtained by spin coating at 2500 rpm at room temperature loaded with increasing amounts of the sol-gel containing the TiO_2 precursor which correspond to different values of $\text{Ti}:\text{PEO}$ molar ratio a) 1 mol%, b) 2.5 mol%, c) 10 mol%, d) 20 mol%, e) 40 mol%, f) 60 mol%, g) 80 mol%. The average values of the diameter (D) of the PEO block for the neat SEO and the hybrid samples with different contents of TiO_2 precursor are reported in h.

It is apparent that the D values decrease with increasing TTIP content in the initial solution. The decrease in D can be understood as a cooperative effect of two different factors:

1) Effect of the complex micellization behavior of amphiphilic di-block copolymers in mixed solvents.⁵⁴ In general, the size and shape of amphiphilic diblock copolymer micelles depends on the interfacial tension between the two solvated blocks. If one uses a mixed solvent system, such as the toluene/isopropanol system employed in this study, at least one of the blocks will be preferentially solvated by one solvent component. In these cases, the resulting interfacial tension and thus, the micelle size, is a function of the solvent composition. Seo et al. investigated the micellization of a PS-*b*-PEO copolymer with PEO volume fraction of 87% using a mixed solvent consisting of a hydrophobic and hydrophilic component .⁵⁵ It was found that the domain size of the resulting PEO block decreased with the hydrophilicity of the mixed solvent. In our system addition of increasing amount of TTIP precursor solution (see Table 3.4) increases also the solvent because also the relative amount of isopropanol increases. Therefore it may be assumed that also in our system the size of PEO domains decreases with increase of TiO₂ precursor content⁵⁶ because of increase of the degree of hydrophilicity of the mixture of solvents (toluene/isopropanol) used for the preparation of hybrid thin films. This effect may be referred as *cosolvent effect*.

2) Effect of crystallization of PEO block. Crystallization of PEO block was probably suppressed with the addition of increasing amount of TTIP. This is a well-known phenomenon in polymer blending, where the intimate mixing of a second polymer prevents PEO crystallization.⁵⁷⁻⁵⁸ In this case a loss of crystallinity in the PEO block was produced by the infiltration of TiO₂ into its domain. The inorganic oxide was chemically linked by hydrogen bonds with PEO chains preventing full crystallization of the PEO domain (*loss of crystallinity*).⁵⁹ It is worth noting that in general selective introduction of inorganic materials in specific domains of a block copolymer may induce different changes up to lead to morphological transitions with respect to the morphology of the neat BCP. Templin et al.⁶⁰ described the achievement of different morphologies after selective confinement of organically modified silica mesostructures in the PEO domains of a PI-*b*-PEO copolymer. Yeh et al.⁶¹ infiltrated CdS quantum dots into the PEO block of a PS-*b*-PEO diblock copolymer, passing from originally hexagonally packed cylindrical structures to bcc or sc structures.

The occurrence of this cooperative factors was evaluated adding 200 μl of toluene/isopropanol mixture in 1:1 vol/vol ratio (“white solution”) to 500 μl of 1 wt% PS-*b*-PEO solution ($\phi_p = 40\%$, see Figure 3.21a-b). The “white solution” had the same composition of the solvent used for dissolving the titania precursor in our sol/gel system. FESEM images of thin films of neat SEO prepared from 1 wt% BCP toluene solution, of SEO prepared adding to 1 wt% BCP solution the white solution and of SEO hybrid system containing 10 mol% TiO_2 precursor and are shown in Figure 3.21. It is apparent that the diameter of cylindrical PEO domains D of neat SEO equal to 39 nm (Figure 3.21a) decreased upon addition of both the white solution (Figure 3.21b) and the solution of TiO_2 precursor (Figure 3.21c), assuming average values of 32 and 26 nm respectively. Simultaneously the center-to-center distance d_{c-c} of neighboring cylinders increased only slightly from the value of 69 nm (Figure 3.21a’) to values of ≈ 73 nm (Figures 3.21b’ and c’). We argue that the addition of the white solution produced an decrease of D value because of *cosolvent effects*, whereas in the hybrid system the decrease of D value was due to both *cosolvent effect* and *loss of crystallinity*.

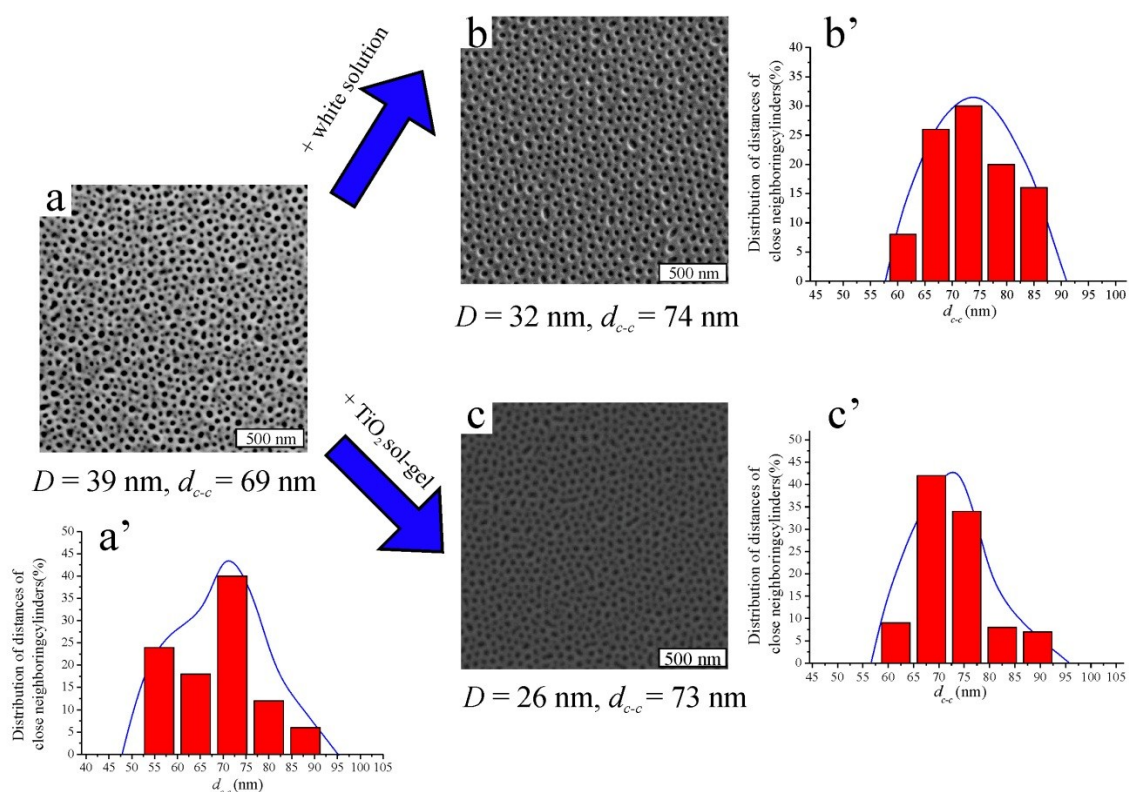


Figure 3.21: FESEM images ($2\mu\text{m} \times 2\mu\text{m}$) of thin films of neat SEO (a), neat SEO obtained adding the white solution to 1 wt% BCP toluene solution (b) and hybrid SEO system containing 10 mol% TiO_2 precursor obtained by spin coating at 2500 rpm at room temperature. Bar diagrams with fitting curves depicting the distribution of center-to-center distance between neighboring cylinders (a’-c’).

3.4 Heat-treated materials

After the obtainment of the hybrid materials the next step was the achievement of ordered titania nanoparticles. It was necessary to reach a temperature at which the copolymer is completely removed (>458 °C as depicted from TGA of Figure 3.2). At that temperature anatase crystallographic form appeared as shown from the DTA of the xerogel of Figure 3.14. The hybrid nanocomposites were annealed at 600°C at a rate of 2 °C min⁻¹ and were kept at that temperature for 4 h to be sure of the complete removal of the PS-*b*-PEO. FESEM images of the heat-treated hybrid samples are shown in Figure 3.22. TiO₂ bright nanoparticles were clearly distinguished for all the compositions of the initial hybrid systems (Figure 3.22a-g) standing up on the surface of the substrate according to a pseudo-hexagonal geometry reminiscent of the hexagonal morphology of the hybrid nanostructures.

The diameter of the nanoparticles originated from the sample containing 1 mol% of titania precursor was 13.5 nm. With increasing additions of TTIP the corresponding heat-treated samples presented a progressively greater diameter of the nanoparticles (NPs). The diameters of the nanoparticles increased up to the case of the sample with a TTIP/PEO molar ratio of 20 mol%. For the samples containing 40-60-80 mol% of the titania precursor an inversion of this trend was experienced reaching a constant value of about 17 nm. This result can be interpreted comparing the values of D of the PEO domains that accommodated the inorganic oxide before its removal and the diameter of the NPs with increasing content of TTIP in Figure 3.22h.

Comparing the two curves of Figure 3.22h one can easily conclude that the evolution of the size of the titania network is strictly related to the dimensions of the PEO affine block. Up to the addition of 20 mol% of Ti alkoxide a continuous growth of the NPs was detected bringing the complete filling of PEO domains (D of PEO = 27 nm, D of the NPs = 30 nm). Since a decrease of the section of the cylinders of PEO, for further increases of ϕ_p , occurred due to the cosolvent effect coupled with the loss of crystallinity of the hydrophilic domains tethered with the titania network, a decrease of the diameter of the NPs also occurred while increasing the degree of coverage of TiO₂ particles on the substrate (vide infra).

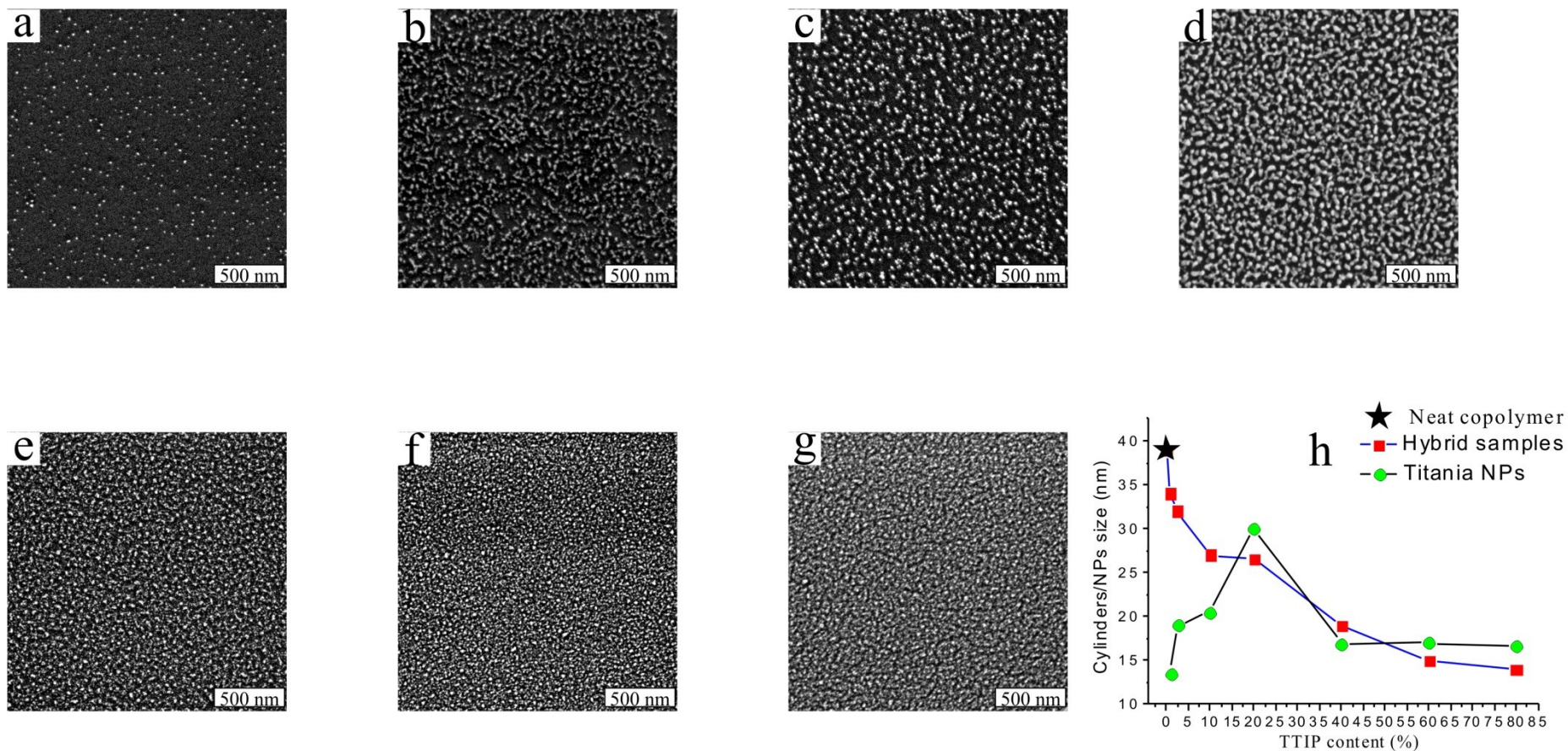


Figure 3.22: FESEM images ($2\mu\text{m} \times 2\mu\text{m}$) of the heat-treated (600°C at a rate of 2°C min^{-1} for 4h) hybrid samples obtained by spin coating at 2500 rpm at room temperature loaded with increasing amounts of the sol-gel containing the TiO_2 precursor which correspond to different values of $\text{Ti}:\text{PEO}$ molar ratio a) 1 mol%, b) 2.5 mol%, c) 10 mol%, d) 20 mol%, e) 40 mol%, f) 60 mol%, g) 80 mol%. The values of the diameter (D) of the neat SEO, of the hybrid samples with different contents of Ti precursor and of titania NPs are reported in h.

The area coverage of TiO₂ NPs in the heat-treated sample (Figure 3.23a-g) is reported as a function of TTIP content. The *ImageJ* software was used in order to measure the area coverage. *ImageJ* is a public domain, Java-based image processing program developed at the National Institutes of Health. *ImageJ* was designed with an open architecture that provides extensibility via Java plugins and recordable macros.

The FESEM images of Figure 3.22 were firstly converted in binary images and then the percentage of the area occupied from TiO₂ NPs, here seen as dark dots, was calculated. A steady growing of the area coverage percentage was measured as reported in Table 3.5 and depicted in Figure 3.23h, reaching the maximum value of about 80% for the sample containing 80% of titania precursor.

Table 3.5: Heat-treated samples obtained from hybrid systems with the indicated TTIP/PEO molar ratio and the corresponding area coverage of the TiO₂ NPs.

Heat-treated samples (<i>n</i> TTIP/ <i>n</i> PEO %)	TiO ₂ Area coverage %
1	2.3
2.5	15.3
10	17.5
20	38.5
40	51.6
60	55.9
80	76.8

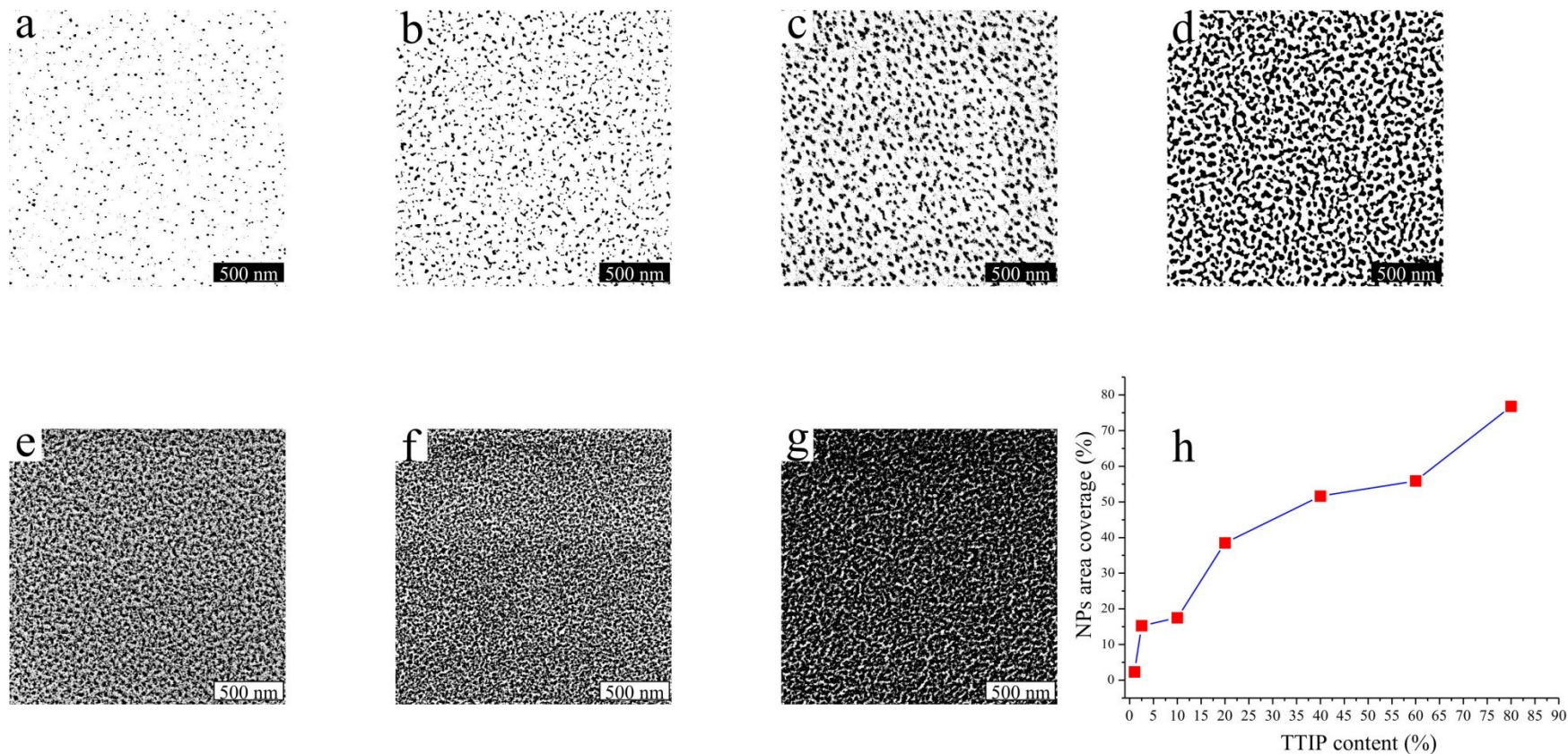


Figure 3.23: Converted binary FESEM images ($2\mu\text{m} \times 2\mu\text{m}$) using *ImageJ* of the heat-treated (600°C at a rate of 2°C min^{-1} for 4h) hybrid samples obtained by spin coating at 2500 rpm at room temperature loaded with increasing amounts of the sol-gel containing the TiO_2 precursor which correspond to different values of *Ti:PEO* molar ratio a) 1 mol%, b) 2.5 mol%, c) 10 mol%, d) 20 mol%, e) 40 mol%, f) 60 mol%, g) 80 mol%. The values of titania NPs area coverage are reported in h.

3.5 PEO-TiO₂ thin films materials

In the current literature the system PEO-TiO₂ has received attention and the use of the PEO homopolymer as dispersant of TiO₂ precursor restituted different effects: it acted as retardant for the growth of anatase nanocrystals,⁶² it increased the photodecomposition rates by synthesis of PEO-TiO₂ particles spherical shape,⁶³ PEO was also used to enhance the crystal growth kinetics of TiO₂ crystals due to the increased surface area induced by dissolution of PEO component in hybrid networks.⁶⁴

In this contest the preparation of PEO-TiO₂ hybrid materials was developed in order to attest that in absence of self-assembly from a block copolymer, such as the PS-*b*-PEO used here, TiO₂ does not form any nanostructured surface. A PEO with molecular mass of 20 kDa ($T_m^I = 65.1^\circ\text{C}$, $T_c = 40.5^\circ\text{C}$, $T_m^{II} = 63.8^\circ\text{C}$; temperature of complete degradation of PEO 422°C) was dissolved in toluene (1 wt%) and then spin-coated (2500 rpm for 30'') on Si wafer. The FESEM image of the neat PEO showed a smooth surface without any particular morphology (see Figure 3.24a).

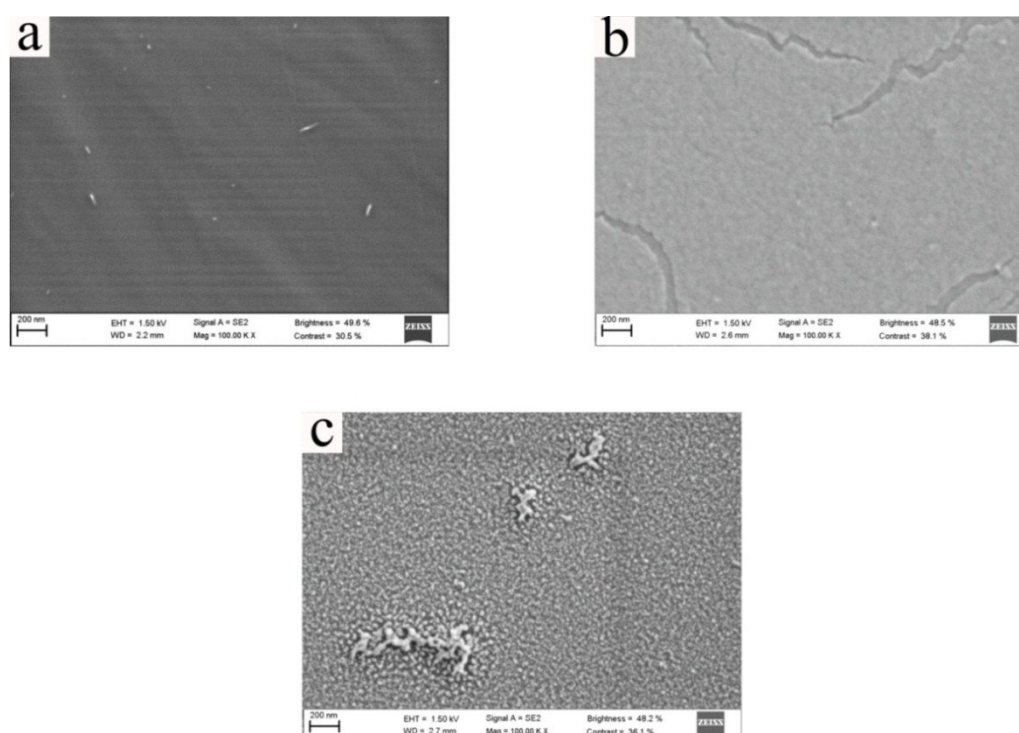


Figure 3.24: FESEM images of the neat PEO homopolymer (a), of the hybrid PEO-TiO₂ sample ($n\text{TTIP}/n\text{PEO} = 2.5$ mol%) (b) and the corresponding heat-treated sample (c) thin films obtained by spin-coating at 2500 rpm at room temperature.

200 μl of a sol-gel prepared as in Paragraph 2.6 was added to 500 μl of a toluene PEO solution (TTIP/PEO m.u. molar ratio = 2.5 mol%) and then deposited as thin film by spin-coating. As happened for the neat homopolymer also in this case FESEM image (Figure 3.24b) indicated that the surface resulted quite flat with some cracks disposed randomly on the surface. The last step was to perform heat-treatment (600°C at a rate of $2^{\circ}\text{C min}^{-1}$ for 4 h) of the hybrid PEO sample aimed to investigating the morphology of TiO_2 on the Si wafer. As shown by FESEM image of Figure 3.24c after the removal of the PEO homopolymer disordered TiO_2 films covered by particles of size of tens nanometers forming large and irregular aggregates were obtained. The use of neat PEO homopolymer instead of nanostructured BCP demonstrated that the TiO_2 films by heat-treatments are featureless with no particular mesoscopic arrangement of nanocrystals.

3.6 Adhesion tests of the heat-treated hybrid films

The heat-treated sample obtained from the BCP hybrid films containing 2.5 mol% TTIP (Figure 3.25a) underwent to two different tests aimed at probing the degree of adhesion properties of TiO₂ inorganic nanocrystals.

As first test an air flow with a rate of 32 L/min at 7 bar was directed for 30 seconds on the heat-treated sample. In the second test the same sample was dipped into a pH 4 solution for one minute. The corresponding images are shown in Figures 3.25b and c.

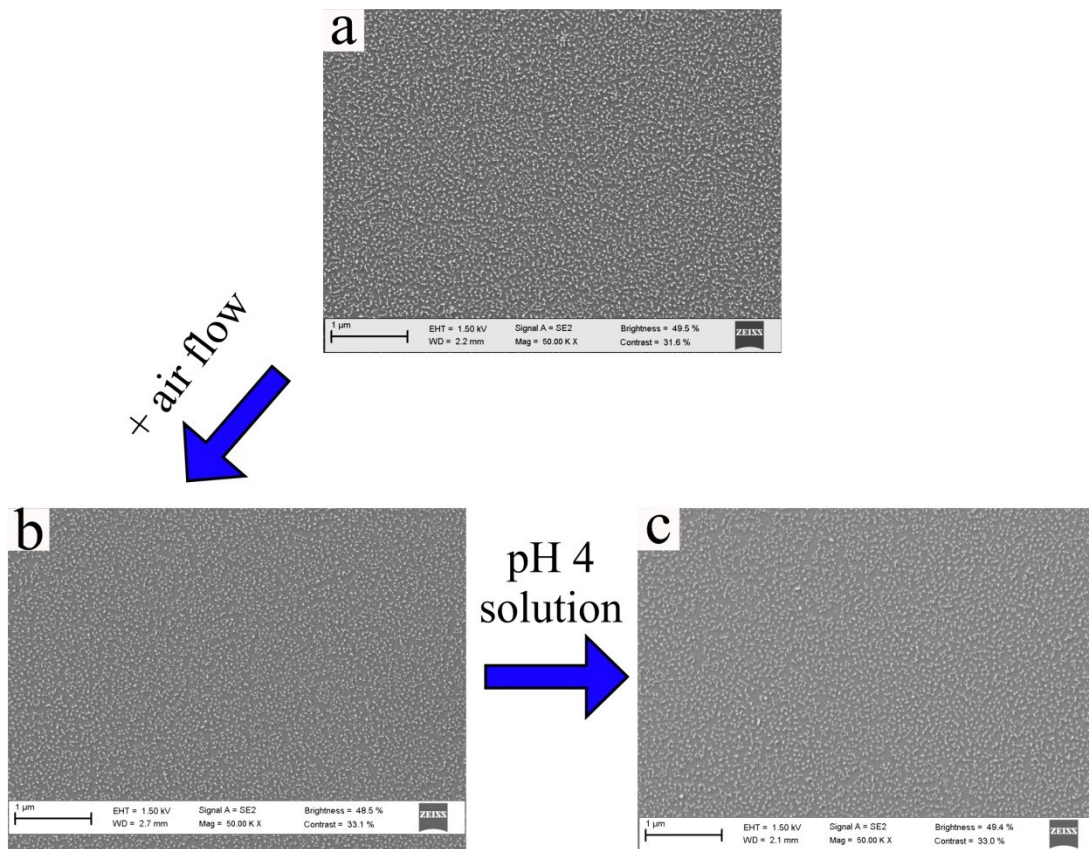


Figure 3.25: FESEM images of the heat-treated PEO-TiO₂ sample ($n_{\text{TTIP}}/n_{\text{PEO}} = 2.5 \text{ mol\%}$) obtained by spin coating at 2500 rpm at room temperature before (a) and after flowing air with a rate of 32 L/min at 7 bar for 30'' (b) and successive dipping in a pH 4 solution for one minute.

This indicated that the nanometric particles of anatase were quite well anchored on the surface of the Si wafer. The evaluation of the area coverage of the three images gave the same value of 15%.

3.7 Solvent annealing: a methodology to improve on long range scale the cylindrical morphology of the neat SEO and of the hybrid materials

Thin films of block copolymer have attracted particular attention due to their potential applications in areas ranging from nanolithographic masks, high surface area catalyst supports, membranes, etc.

In these applications, critical issues are the control of both lateral ordering as well as the orientation of microstructures of block copolymers. A number of strategies have been developed to control the nanoscopic orientation of these thin films including surface modification using random copolymers, the use of templates, the employment of specific surface interactions, applying external fields, as already discussed in Paragraph 1.4.

Solvent evaporation under controlled conditions can provide a strong directional field to orient block copolymer film nanostructures.⁶⁵ A high degree of lateral order with few defects can be achieved. This results from the propagation of ordering from the surface into the film. It may also enable ordered structures to develop more rapidly, although equilibrium morphologies may not be accessed without further annealing. Krausch and co-workers showed that the solvent (THF) evaporation rate could be used to change the orientation of lamellae formed by a PS–P2VP–*Pt*BMA [(P2VP = poly (2-vinylpyridine and *Pt*BMA= poly (tert-butyl methacrylate))] triblock copolymer.⁶⁶ It was further shown that macroscopic sample geometries (confinement within channels) could be used to enhance alignment due to the anisotropic lateral contraction induced. Parallel lamellae were observed for low evaporation rates, and perpendicular lamellae for high evaporation rates.

Russell and co-workers have applied the solvent annealing technique very successfully to PS–PEO films annealed in benzene vapor.⁶⁷ GISAXS has been used to probe the development of ordering and the perfection of the hexagonal structure has been quantified via triangulation algorithms. For PS–PEO diblocks, environment-controlled spin-coating in a mixed solvent atmosphere of toluene and water leads to well-developed perpendicular PEO cylinder orientation.⁶⁸ Toluene is a selective solvent for PS, whereas water is selective for PEO. Perpendicular orientation was favored in the presence of a mixture of solvents selective for each block.

In contrast, Xuan et al. suggest that well-ordered cylinders form in thin films in the presence of a PMMA-selective solvent (chloroform or acetone) only. Following extended solvent vapor treatment, the parallel cylinder morphology is recovered with PMMA at the surface instead of

PS. It has been mentioned that solvent annealed structures can be subjected to aging, in particular interfacial flattening, due to interfacial tension.⁶⁹

Addition of salt has been shown to improve the ordering of perpendicular PEO cylinders in a PS-PEO diblock film during solvent annealing.⁷⁰ Complexation of the alkali halide or metal salts with PEO leads to greater incompatibility between blocks and enhanced mobility of the polymer chains, both contributing to the improvement in ordering.

Annealing in selective solvents can lead to non-equilibrium structures in PS-PMMA diblocks.⁷¹ Annealing of either a symmetric or an asymmetric sample in a selective solvent for PMMA (acetone) created initial hexagonal-packed sphere structures, which upon further exposure to solvent developed into the expected stripe patterns resulting from lamellar or cylinder structures. The non-equilibrium hexagonal structures can be trapped by vitrification at room temperature. Annealing in different solvents can be used to switch from parallel to perpendicular cylindrical P4VP + HABA (HABA = (2-(4'-hydroxybenzeneazo)benzoic acid) domain orientation and vice versa in thin films of PS-P4VP complexed with HABA.⁷² The HABA forms a hydrogen bonding complex with the P4VP. Swelling in dioxane even led to a transition to a spherical morphology.

At the present time the lack of a univocal, easy and convenient strategy of exposure to solvent vapors that can be used for both the neat and the inorganic/organic materials has brought in this study to a deep investigation of these aspects. As first aim the development of a strategy that could work on the neat SEO was achieved. In a second step the reproducibility of these achievements was tested also on the hybrid materials, understanding that the tuning of certain physical parameter, such as the value of relative humidity (RH%) played a great role for the final morphology.

The polymer-solvent interaction parameter χ , was taken into account to evaluate the miscibility between a polymer and a solvent and in our case χ was calculated in order to quantify the affinity between the blocks constituting the PS-*b*-PEO copolymer and the vapors of different solvents.¹ This parameter is modeled as the sum of entropic and enthalpic components:

$$(\chi = \chi_H + \chi_S) \quad (1)$$

where χ_H is the enthalpic component and χ_S is the entropic component. χ_S is usually taken to be a constant between 0.3 and 0.4 for nonpolar systems: $\chi_S = 0.34$ is often used.⁷³ The enthalpic component can be related to the Hildebrand parameters:

$$\chi_H = [V_i(\delta_1 - \delta_2)^2]/RT \quad (2)$$

with V_i the molar volume of species, δ_1 and δ_2 the Hildebrand parameters of the interacting polymer and solvent, R the ideal gas constant at temperature T . Substituting eq. (2) in eq. (1):

$$\chi = [V_i(\delta_1 - \delta_2)^2]/RT + 0.34 \quad (3)$$

Equation (3) permits only positive values of the interaction parameter. Since the Flory-Huggins criterion for complete solvent-polymer miscibility is $\chi < 0.5$, the enthalpic contribution must be small and the solubility parameters of the solvent and polymer must be similar. The molar volume of the solvent also affects miscibility and phase equilibria: a Hildebrand parameter needed for phase separation or miscibility cannot be specified without specifying V_i . Equation (3) works well for nonpolar systems for which Eq. (2) is a good description of the enthalpic component of the interaction parameter. The geometric mean assumption of regular solution theory is not appropriate for polar systems, and better models include an extra term describing the interchange energy density for the solvent-polymer pair. For example:

$$\chi = \chi_S + (V_i A_{12})/RT \quad (4)$$

with:

$$A_{12} = \delta_1^2 - \delta_2^2 - 2 \times l_{12} \delta_1 \delta_2 \quad (5)$$

where l_{12} characterizes the intermolecular forces between molecules (rather than using the geometric mean assumption). Equation (5) allows the modeling of specific interactions between components 1 and 2. Mixed solvents can be treated as a single solvent by determining the solubility parameter of the solvent mixture, and then using this value in Eq. (3). If both the solvents and the polymers interact, the description is more complicated. An alternative definition of A_{12} uses the two-component solubility parameter:

$$A_{12} = (\delta_{1d} - \delta_{2d})^2 + (\delta_{1p} - \delta_{2p})^2 \quad (\text{eq. 6})$$

with δ_d is the dispersion solubility parameter, and δ_p is the polar solubility parameter.⁷⁴⁻⁷⁶ The Hansen parameters may also be used to model A_{12} .¹

Taking into account these considerations the χ values for each polymer-solvent pair used in this study were calculated as reported in Table 3.6.

Table 3.6: Molar volume (V_s), Hildebrand parameter (δ); dispersive term (δ_d); polar term (δ_p); polymer-solvent interaction parameter for the PS block [χ_{p-s} (PS)] and for PEO block [χ_{p-s} (PEO)].

Solvent/Polymer	V_s (cm³/mol)	δ (J cm⁻³)	δ_d (J cm⁻³)	δ_p (J cm⁻³)	χ_{p-s} (PS)	χ_{p-s} (PEO)
Water	18.0	47.9	15.5	18.0	1.1	1.6
Water/Toluene (1:1 vol/vol)	62.4	33.1	16.7	4.7	0.4	0.4
Acetone	74.0	20.3	15.5	10.4	1.0	2.1
Toluene	106.8	18.2	18.0	1.4	0.3	0.5
PS		18.6	17.6	6.1		
PEO		19.9	17.3	3.0		

Based on the parameters of Table 3.6 a preference of the PS block, in comparison to PEO block, to the toluene solvent annealing may be established. The χ values are both less than 0.5 but the difference between them is appreciable. Also in the case of water/toluene mixed solvent a good miscibility is predictable. Otherwise when acetone or pure water vapors are employed a poor affinity is expected. A slight overestimation of χ_{p-s} (PEO) relative to the water solvent annealing is detected due to the lack of a term in eq.6 that can consider the

strong specific interactions (hydrogen bonds) that are established between the hydrophilic PEO block and water.

3.7.1 Solvent annealing on the neat SEO by exposure to solvent vapors in a closed vessel

The first attempt to achieve an improvement of the long range morphological order of the SEO spin coated thin films was to place them in a closed vessel containing toluene vapors (the same solvent used to dissolve the PS-*b*-PEO copolymer) at room temperature. The thin films of the neat SEO were left under solvent annealing several hours (24 or 48 h). Russell and co-workers⁶⁷ showed that the starting morphology obtained by spin-coating of a PS-*b*-PEO was far from the equilibrium morphology, and the degree of lateral order was low. After the solvent annealing treatment and the removal from the benzene atmosphere, the solvent evaporates and the ordering of the PEO domains improved dramatically with a strong reduction of the defects after 48 h.

In our case after 24 and 48 hours no morphological improvement was detected as shown in Figure 3.26a,b. The cylindrical morphology was still found only in some areas and not over the entire surface of the substrate as happened for SEO thin films that did not undergo to any treatment (Figure 3.6).

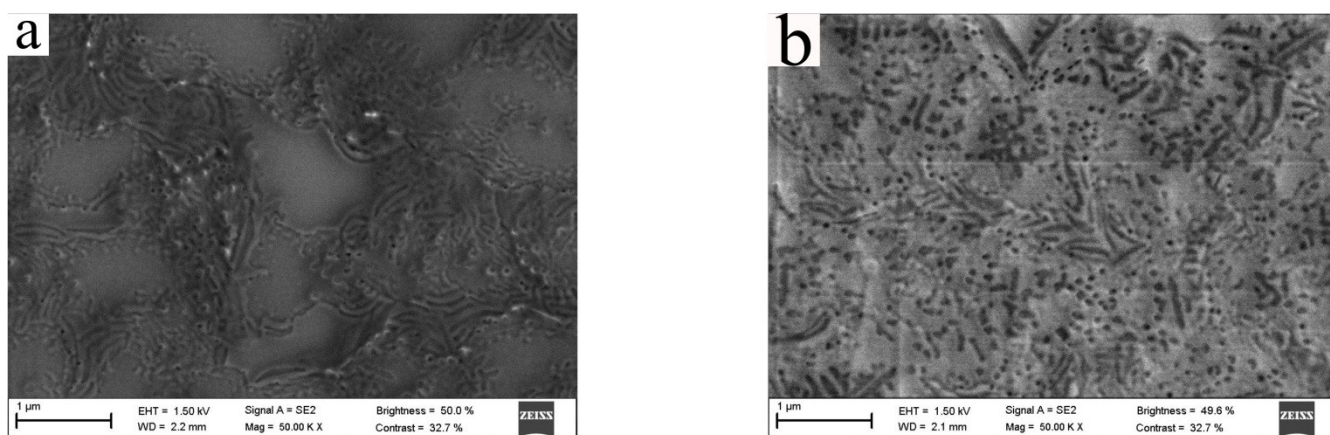


Figure 3.26: FESEM images of the neat SEO thin films spin-coated at 2500 rpm at room temperature and then annealed by toluene vapors for 24 (a) and 48 h (b) in a closed vessel.

Moreover some cylinders parallel to the substrate are clearly visible evidencing a transition to a stripe nanostructure after the solvent annealing by toluene vapors. This behavior was also

experienced by Chen et al.⁷¹ that developed a reproducible way of obtaining nanopatterns in PS-*b*-PMMA diblock copolymer thin films. They selected acetone as preferential solvent for PMMA block. The χ parameter, measured considering eq. 6 as in our study, was calculated to be 0.6 and 0.3 for PS and PMMA respectively (acetone should be a non-solvent for PS and a good solvent for PMMA). When the PS-*b*-PMMA thin films were annealed by acetone, the highly lateral ordered nanopatterns can be formed with different morphologies from spherical domains to striped ones. The characteristic spacing of striped surface patterns was similar to the bulk period. After solvent extraction, the formed structures were frozen. Both components PS and PMMA were vitrified and stiff at room temperature; therefore, the surface pattern were stable under ambient conditions.

Our system gave the same behavior: toluene was employed for solvent annealing and represented a good solvent particularly for the PS block [χ_{p-s} (PS) = 0.3 and χ_{p-s} (PEO) = 0.5]. The section of the cylinders was measured for both parallel and perpendicular cylinders and was found practically identical in both cases (~40 nm).

3.7.2 Solvent annealing on the neat SEO and on the hybrid samples directly in the spin-coating chamber

For BCP PEO-based systems, it was found that one of the most critical processing conditions was the control of relative humidity during the solvent annealing step and it was found that the achievement of precise values of humidity brought to an high degree of lateral ordering.

Bang et al.⁷⁷ were able to improve the degree of lateral ordering of PEO-*b*-PMMA-*b*-PS triblock copolymers that were spin-coated onto silicon substrates. The solvent annealing process was performed in a homebuilt glove-box chamber at room temperature, which is schematically illustrated in Figure 3.27.

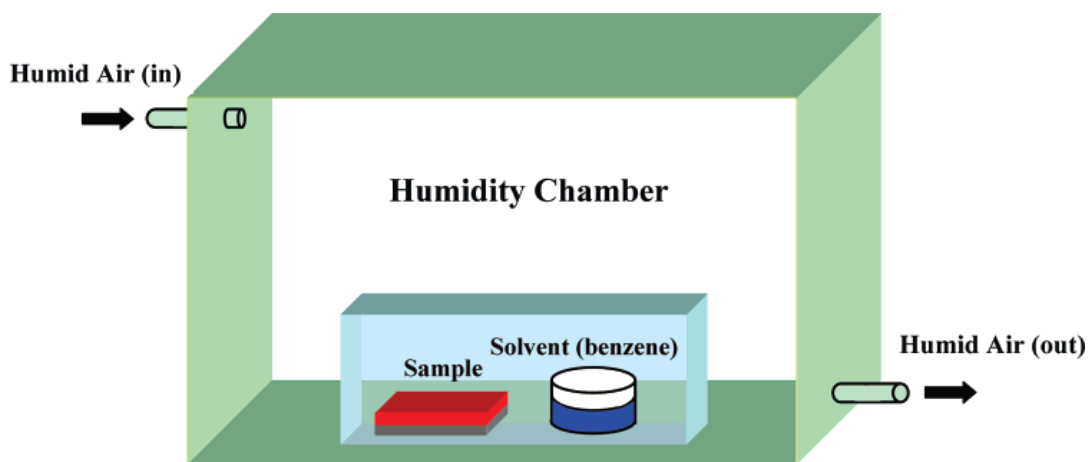


Figure 3.27: Schematic illustration of the solvent annealing chamber used by Bang et al.⁷⁷

The whole glove-box chamber was continually flushed with humid air, which was produced by bubbling air through warm water (~ 50 °C). The relative humidity percentage (R.H.%) in the chamber was controlled by admixing dry air or adjusting the water temperature and was monitored just before the removal of the inner chamber. Once the desired R.H. condition was reached, it was maintained constant throughout the whole process. As shown in Figure 3.27, samples are placed in the much small inner sealed chamber, an upside down glass container on a larger glass Petri dish, under saturated benzene vapor where the R.H. is initially the same as in the much larger outer chamber. The samples were annealed for 12 h, then the upside down glass container was simply removed from the Petri dish inside the much larger glovebox that serves as the humidity chamber, thus allowing the benzene in the swollen sample to evaporate under a given R.H. condition.

Kim and co-workers⁶⁸ showed that the orientation and ordering of an asymmetric ($\phi_{\text{PEO}} = 0.23$) PS-*b*-PEO copolymer were reached avoiding relatively long-term (>12 h) solvent annealing process. They reported a strategy for fast processing in order to control orientation of microdomains.

After depositing a 1% (by mass) PS-*b*-PEO solution in toluene onto a silicon substrate, the deposition was performed in a spin-coater which was encased to control the atmosphere. Prior to spin-coating, the enclosed chamber was partially saturated for ≈ 40 seconds with an excess of a given liquid solvent. They developed a faster (<2 min) methodology respect the classical ones to control the orientation of cylindrical microdomains in thin block copolymer films using a controlled atmosphere spin-coating process. During spinning, a preferential affinity of water vapor was detected allowing the PS-*b*-PEO cylinder orientation to be controlled from

parallel to perpendicular with respect to the film surface and with a relatively high degree of lateral order for perpendicular orientations.

The illustrated scientific scenario shows that parameters as the relative humidity and the development of a fast procedure are essential key points for the achievement of an innovative and effective solvent annealing process that can be able to reduce the morphological defects at long range scale. Many efforts have been done in the present study to develop a novel single step method for film deposition/solvent annealing process that could work properly on both neat PS-*b*-PEO copolymer and the hybrid nanocomposites. The first attempt corresponded to the production of a controlled vapor atmosphere in the closed spin-coater chamber, as represented in Figure 3.28a, where the organic or the hybrid solutions were spin coated simultaneously to solvent annealing process. On the bottom of the chamber two Petri dishes filled with the appropriate solvent were placed.

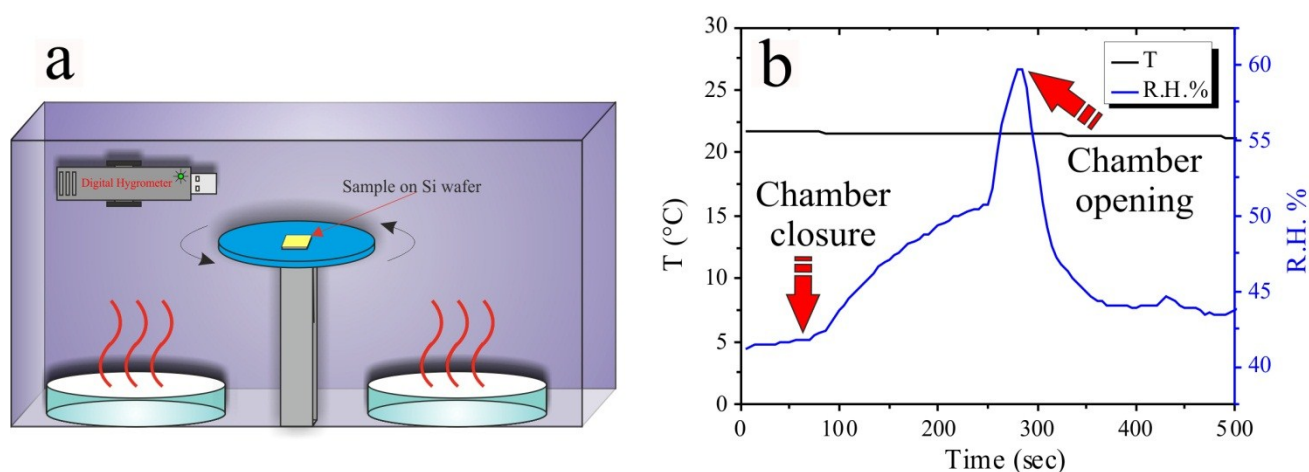


Figure 3.28: Schematic illustration (a) of the sealed solvent annealing chamber containing the organic or hybrid solutions deposited on the substrate on the top of the plate, the Petri dishes filled with the appropriate solvent and the digital hygrometer. In graph (b) the change in R.H.% and T is reported during the entire process. After 1' the spin-coater chamber containing Petri dishes filled with water was sealed, R.H.% increased up to opening of the chamber at 4'40'' experiencing an increase of ~20% R.H.

A digital hygrometer (*LOG32 Data Logger*) was put inside the sealed chamber in order to monitor the values of temperature and relative humidity as a function of time with a frequency of 2 seconds, as shown in Figure 3.28b in the case of water annealing. The variation of R.H.% was monitored before without the presence of the solution on the plate of the spin-coater in order to verify the reproducibility of the process (for each kind of used solvent). So it was

possible to assume that after a certain laps of time a desired value of R.H.% could be reached and the spin-coating process started.

A comparison between the morphology reached for the thin film of unannealed SEO, the toluene and water/toluene (1:1 vol/vol) annealed SEO thin films is reported in Figure 3.29a-c. Figures 3.29b,c are relative to a precise value of R.H.% that was obtained during the process and restituted the best result for each solvent atmosphere (50% R.H. for toluene and 62% R.H. for water/toluene annealing). It appeared that the vapor annealing brought to an improvement of lateral order with respect to the untreated sample.

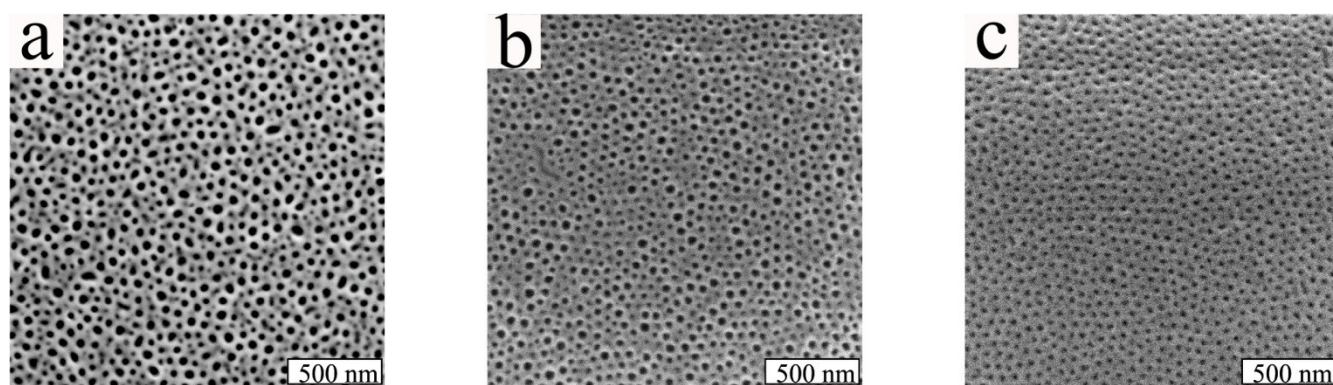


Figure 3.29: FESEM images of the neat SEO thin films spin-coated at 2500 rpm at room temperature (a), after toluene (50 R.H.%) (b) and water/toluene annealing (62 R.H.%) (c) in the sealed spin-coater chamber.

The Voronoi constructions helped to quantify the amount of the improvement of long-range order. In mathematics, a Voronoi diagram is a way of dividing space into a number of regions. A set of points (called seeds, sites, or generators) is specified beforehand and for each seed there will be a corresponding region consisting of all points closer to that seed than to any other. The regions are called Voronoi cells.

It is named after Georgy Voronoi, and is also called a Voronoi tessellation, a Voronoi decomposition, or a Dirichlet tessellation (after Lejeune Dirichlet). Voronoi diagrams have found numerous practical and theoretical applications and can be found in a large number of fields, even in art, in technology and in chemical sciences where it is employed to better visualize lattice defects,⁷⁹⁻⁸² such as dislocations and disclinations.

In this study these diagrams were created by drawing bonds to connect the center of each sphere (corresponding to the top section of the PEO cylinders) to its neighbors. The perpendicular bisectors of these bonds intersect to form a polygon. The polygon has a number of sides equal to the number of nearest neighbors of the sphere in the center. For example the

6-fold-coordinated sites will appear as green hexagons while 5's are displayed as olive pentagons and 7's are displayed as red heptagons.

The occasional misidentification of coordination number for cylinders at the image edges by the Voronoi algorithm was corrected by hand. Additionally, data from cylinders whose centers lay within one lattice period of the edges of the image were discarded.

The creation of these diagrams was possible thanks the use of *ImageJ* software running a macro written expressly for this study by J. Hanson, Senior Imaging Analyst at Eli Lilly and Company.

This algorithm worked efficiently on images of $1\mu\text{m}\times 1\mu\text{m}$ (see Figure 3.30a-c) that were analyzed starting from the FESEM images of Figure 3.29 (neat SEO with no annealing, toluene annealing and water/toluene annealing).

A quantitative evaluation of the improvement of the long range order was measured using the equation $\%_{Hex} = N_{Hex} / N_{Poly} \times 100$ that restituted the percentage of the hexagons ($\%_{Hex}$) once counted the number of hexagons (N_{Hex}) and of the all the present polygons (N_{Poly}).

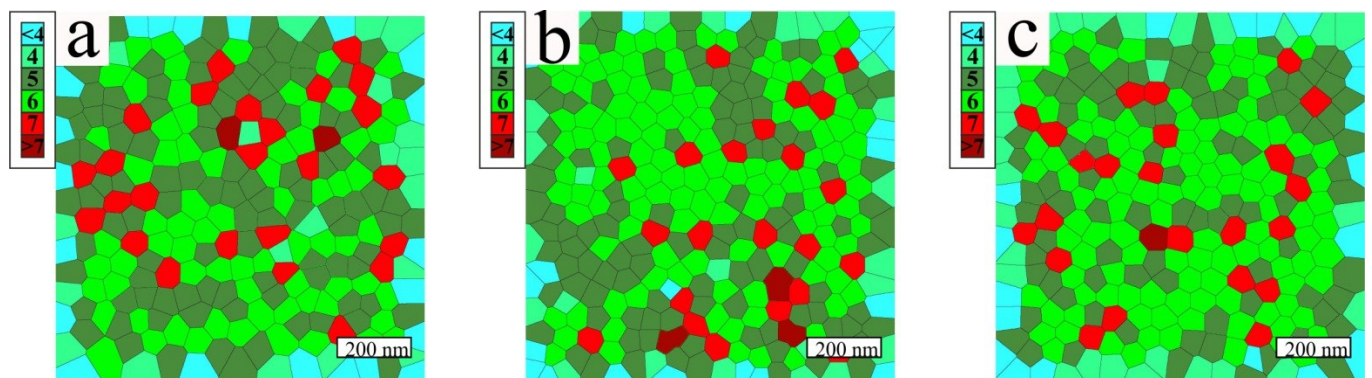


Figure 3.30: Voronoi constructions of $1\mu\text{m}\times 1\mu\text{m}$ of the neat SEO thin films spin-coated at 2500 rpm at room temperature before (a) and after toluene (50 R.H.%) (b) and water/toluene annealing (62 R.H.%) (c). On the top left of each image a legend highlighting the correspondences between colors and number of the side of the polygons is reported.

An effective and tangible improvement was experienced controlling the inner atmosphere of the spin-coating chamber passing from the 35% of hexagons for the neat SEO to 46 and 53 % for toluene and water/toluene annealing respectively.

Using water annealing the formation of square platelets with a side length of $\sim 1\mu\text{m}$ was detected, for annealing treatment with humidity conditions of 54 R.H.% (Figure 3.31a) to 62 R.H.% (Figure 3.31b). However formation of these platelets does not impair the cylindrical morphology all over the substrate.

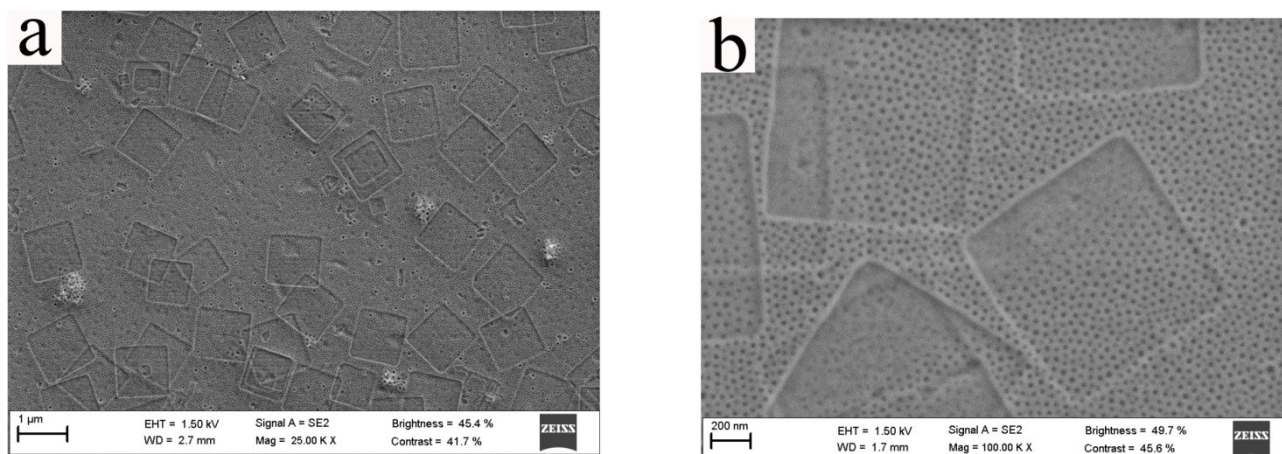


Figure 3.31: FESEM images of the SEO thin films spin-coated at 2500 rpm at room temperature after water annealing at different values of R.H.%: 54 R.H.% (a) and 62 R.H.% (b) in the sealed spin-coater chamber.

Theoretical studies using self-consistent-field calculations, scaling arguments, and computer simulations have indicated that tethered block copolymer brushes exhibit complex behaviors that depend on many factors. These factors include the Flory-Huggins interaction parameter, the overall molecular weight, the volume fraction of one block, the flexibility of the backbone, the grafting density, environmental conditions (solvent, temperature), and the surface free energy of each block in the air. Crystalline-amorphous block copolymers have already been used to grow platelets in dilute solutions, practically identical to those detected in this study, which have a “sandwiched” structure with the single crystal in the middle covered by two nano-amorphous block layers on the top and bottom of the basal surface of platelets.⁸³⁻⁸⁴

Some method as the most widely used self-seeding technique, based on partly dissolving preformed crystals at lower crystallization temperature, subsequent reheating to a seeding temperature and then quickly cooling to a preset crystallization temperature, brings to the grow of single crystals. Huang et al.⁸⁵ demonstrated that the formation of lamellar square platelets was possible preparing dilute toluene solution of a semicrystalline ABC triblock copolymer, polystyrene-*b*-poly(2-vinylpyridine)-*b*-poly(ethylene oxide) (PS-*b*-P2VP-*b*-PEO) with trace amounts of water. It has been shown that the primary role of water was to solvate the PEO blocks by hydrogen bonding and the water to PEO monomeric unit molar ratio played an important role in determining the structure of aggregates in the solution. The hydrogen bonding between the water and PEO m.u. facilitated the nucleation of the crystallization of PEO blocks.

It was reported that also for polystyrene-block-poly(ethylene oxide) (PS-*b*-PEO) copolymers sandwich-like platelets were generated, with the PEO single crystals in the middle covered by two amorphous layers on the top and bottom of the PEO basal surface. The crystallization behavior of the platelet was evidenced by the electron diffraction pattern, which was recognized to be the [001] zone pattern of the monoclinic lattice of PEO.⁸⁶

Therefore, it is probable that the non-crystalline PEO segments attached to the crystalline surface participate in microphase separation. The formation of a microphase-separated brush depended on two factors: the strong incompatibility between PS and noncrystalline PEO chains (covalently linked to the stems of crystalline PEO) and weak interaction of PS-PS brushes (as depicted in Figure 3.32). This is the explication of the persisting cylindrical morphology on the top of the PEO crystalline platelets.

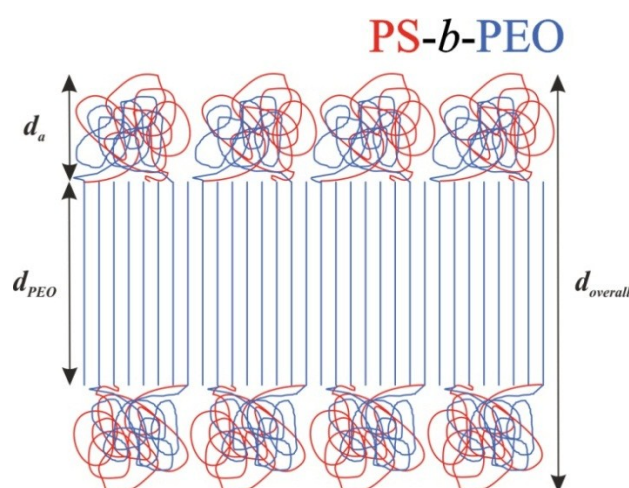


Figure 3.32: Schematic representation of the microphase-separated brushes on the top/bottom of the PEO square platelet. The blue and red lines represent PS and PEO chains, respectively. The overall thickness of the semi-crystalline block copolymer platelet ($d_{overall}$) is represented as the sum of the thickness of the PEO crystal (d_{PEO}) and the thickness of the tethered amorphous chains (d_a).

On the other hand, it has been observed that when the PS-*b*-PEO solution was not stirred and left in storage at room temperature, formation of regular square platelets could be completed in relative short period. This can be explained by the heterogeneous nucleation due to incomplete dissolution of PEO at microscopic level without stirring.⁸⁵⁻⁸⁷

In order to corroborate this behavior thin films from a solution of SEO in toluene were obtained before and after the storage (1 week) at room temperature without stirring (Figure 3.33a,b).

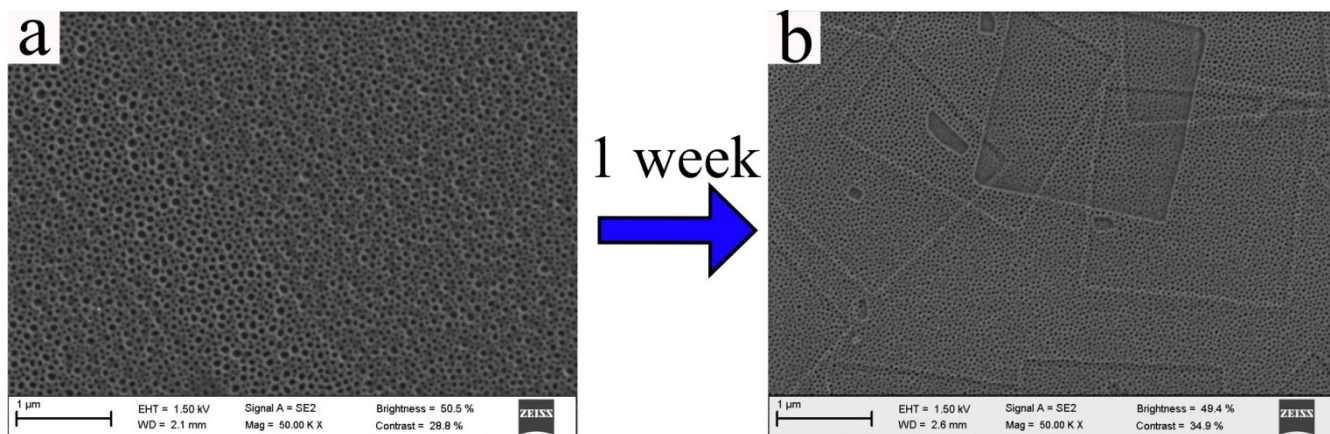


Figure 3.33: FESEM images of the neat SEO thin films spin-coated at 2500 rpm at room temperature obtained from toluene solutions before (a) and after (b) the storage at room temperature for one week without stirring.

The FESEM images confirmed that the aging process led to the formation of square platelets with microphase-separated brushes on their top as already occurred when the as-prepared solution containing the PS-*b*-PEO copolymer was deposited as thin film in a water-rich atmosphere.

In Table 3.7 the values of waiting times to be used in order to achieve specific values of relative humidity for each process of solvent annealing are reported.

Table 3.7: For each kind of solvent employed the elapsed time (in minute) and the corresponding value of relative humidity (R.H.%) are reported.

Solvent	Time (min)	R.H.%
Toluene	30	50
Water/Toluene (1:1 vol/vol)	30	62
Water	3-10	54-62

After the same laps of time (30 minutes) the relative humidity increased further for the water/toluene annealing compared to the toluene annealing. Differently when in the closed spin-coater chamber were introduced the Petri dishes containing only water, the relative humidity increase rapidly, reaching high values after only ten minutes.

The water/toluene annealing, as previously shown by Voronoi diagrams, produced a vapor atmosphere that restituted the best improvement of lateral order for the neat SEO, compared to other annealing treatments. Therefore this mixed solvent annealing was employed on the hybrid solutions in order to reproduce that morphological enhancement. The solution containing a molar ratio between the TiO₂ precursor and the PEO m.u. of 40% was employed for this purpose. Two different values of relative humidity were used in the sealed spin-coater chamber to compare the behavior of the organic/inorganic system with that of neat PS-*b*-PEO. In Figure 3.34a,b the water/toluene annealed samples at 36 R.H.% and 62 R.H.% are reported, reached after 3 and 30 minutes of annealing respectively.

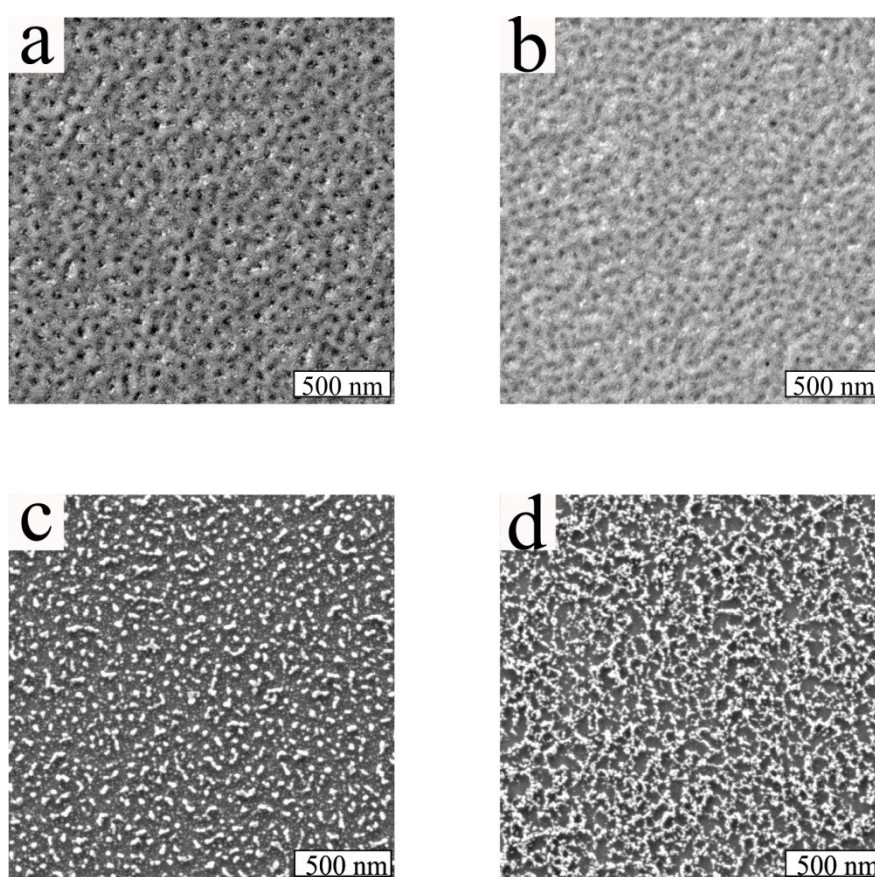


Figure 3.34: FESEM images of the hybrid thin films ($nTi:nPEO = 40$ mol%) spin-coated at 2500 rpm at room temperature after water/toluene annealing at different values of R.H.%: 36 R.H.% (a) and 62 R.H.% (b) in the sealed spin-coater chamber and their corresponding heat-treated samples (c) and (d).

The diameter of cylinders passed from 25 nm to 17 nm when the annealing time and consequently the relative humidity percentage were increased. It was not possible to obtain the Voronoi constructions of these images because of their intrinsic ground noise. This indicates that the enhancement of lateral order achieved for the water/toluene annealed neat SEO was not achieved in the case of the hybrid system.

The so-obtained samples were heat-treated at 600°C to remove the organic matrix. The size and the disposition of the TiO₂ nanoparticles reflected perfectly the size of the preexisting PEO cylinders in the case of the 36 R.H.% solvent annealed sample (D of the nanoparticles \sim 26 nm, see Figure 3.34c) and resulted in an extended disordered network of anatase (Figure 3.34d) for the sample that has been heat-treated starting from the 62 R.H.% solvent annealed sample. An attempt that consisted in spin-coating the hybrid solution in absence of any particular solvent atmosphere was developed in order to exclude that the employment of a certain vapor atmosphere could be responsible of that loss of lateral order.

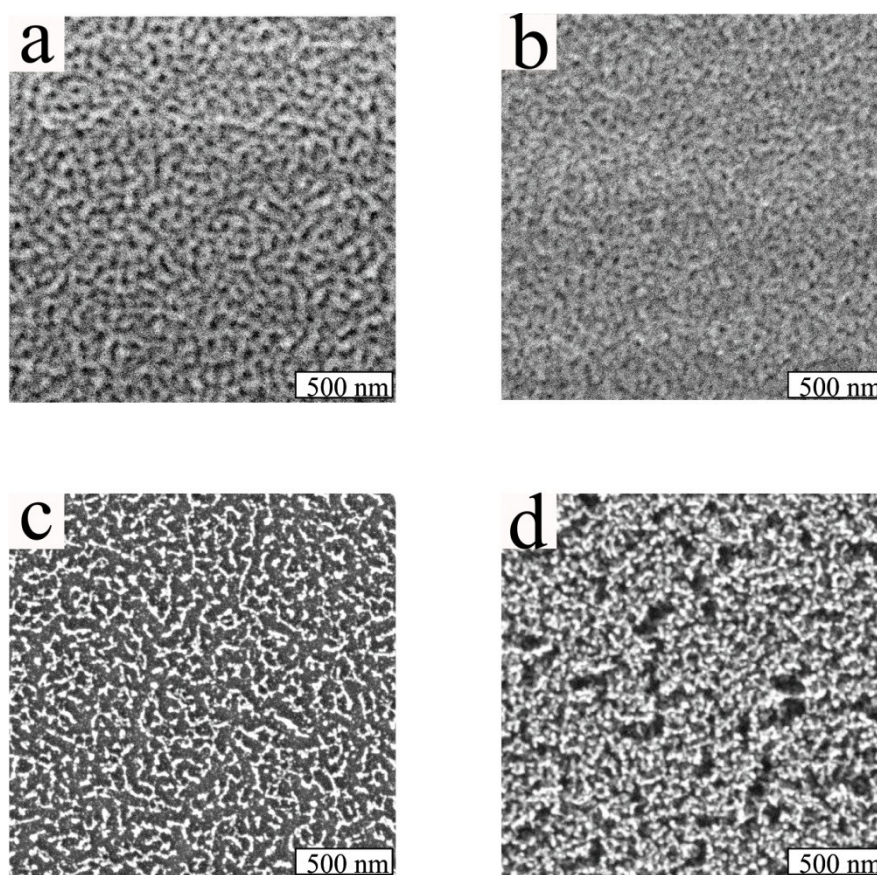


Figure 3.35: FESEM images of the hybrid thin films ($nTi:nPEO = 40\%$) spin-coated at 2500 rpm at room temperature, at room atmosphere (25 R.H.%) after 3 (a) and 30 minutes (b) waiting periods in the sealed spin-coater chamber and their corresponding heat-treated samples (c) and (d).

The hybrid solutions were left on the substrate placed on the plate of the closed spin-coater at room atmosphere (25 R.H.%) starting spin coating after 3 and 30 minutes delay.

An identical behavior was detected for both the hybrid systems (Figure 3.35a-b) and heat-treated samples (Figure 3.35 b-c). As experienced previously for the organic/inorganic samples an increase in the waiting time brought to a decrease in the diameter of the PEO cylinders, passing from 24 to 17 nm. For a comparison of the heat-treated samples of Figure

3.34 and 3.35 the area coverage of titanium oxide nanoparticles was evaluated, as listed in Table 3.8.

Table 3.8: The elapsed time (in minute) that restituted a certain value of relative humidity (R.H.%) and the percentage of TiO₂ area coverage relative to the heat-treated hybrid samples is reported for each kind of vapor atmosphere employed.

Vapor atmosphere	Time (min)	R.H.%	Area coverage (%)
Water/Toluene (1:1 vol/vol)	3	36	24
	30	62	37
Room atmosphere	3	25	28
	30	25	44

The titania nanoparticles obtained after the heat-treatment that derived from the water/toluene annealing and from the room atmosphere process presented a similar area coverage both after three minutes of treatment (24 and 28 %) and after thirty minutes (37 and 44%).

This results brought to the conclusion that leaving the toluene hybrid solution on the substrate before the spinning process produced a random reorganization and a deposition of the inorganic material on the surface of the substrate regardless of the employed solvent atmosphere. This “time-effect” behavior was emphasized when the solution was left steady for a long period before the deposition (the volatility of the toluene is 1.2 greater than water).

3.7.3 A new tool for improving the lateral order of neat and hybrid materials: *Rapid Solvent Annealing* method

The best way to solve this “time-effect” drawback seemed to reduce the time period of exposition of the hybrid solution to the solvent vapors.

A novel methodology of *Rapid Solvent Annealing* (*RSA*, see the schematic representation of Figure 3.36a), never used so far for the obtainment of thin nanocomposite films, was employed here. This procedure consists in the introduction of a flow of solvent vapors directly into the sealed spin-coater chamber. This method permitted to cover a great range of values of relative humidity in a few seconds and was demonstrated to work efficiently both on neat and hybrid thin films. The digital hygrometer was put inside the sealed chamber in order to measure as function of time every two seconds the values of temperature and relative humidity, as reported in Figure 3.36b in the case of water annealing. The variation of R.H.% was monitored first without the presence of the SEO or hybrid solutions on the plate of the spin-coater then in presence of the sample thus confirming the reproducibility of the process for each kind of used solvent. In this way it was possible to establish the amount of time needed to reach a given value of R.H.% before of starting the spin-coating process.

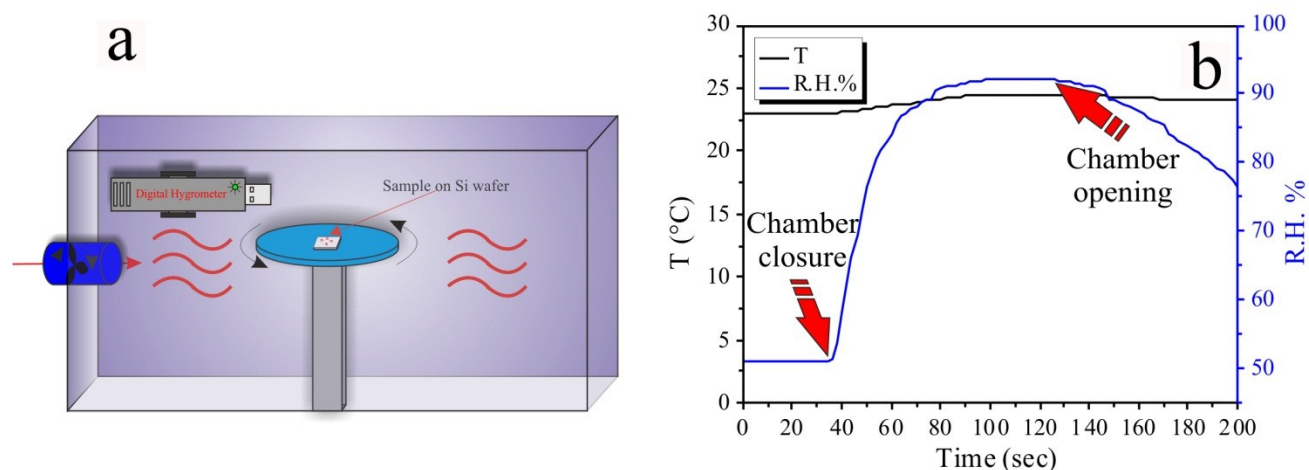


Figure 3.36: Schematic illustration (a) of the sealed solvent annealing chamber containing the organic or hybrid solutions deposited on the substrate on the top of the plate and the digital hygrometer. The solvent vapors were directly flowed into the sealed chamber. In (b) the change in R.H.% and T is reported during the entire process. After 40'' that the spin-coater chamber was sealed, water vapors were introduced into the chamber, and opened after 120'' after reaching an increase of ~40% R.H.

The second step consisted to observe if thin films of PS-*b*-PEO, that underwent to *RSA*, could further improve their morphological order previously achieved using the slow solvent

annealing technique (hence it will be renamed for brevity *SSA*: slow solvent annealing). FESEM images of Figure 3.37a-c are relative to SEO solutions that experienced different atmospheres for only 20'' of exposure to the solvent vapors: acetone, toluene or the mixed solvent composed by water and toluene (1:1 vol/vol).

The FESEM images of Figure 3.37a-c are relative to a surface area of $4\mu\text{m}\times 4\mu\text{m}$ allowing to appreciate the effect of RSA with different solvents on the morphology of the neat copolymer in the long range. Identical images have been indeed obtained by scanning the whole surface of thin films $1\text{cm}\times 1\text{cm}$. At a first glance the water/toluene atmosphere led a dramatic enhancement of the lateral order. Once again the Voronoi constructions helped to quantify the degree of the improvement of the long-range order. In Figure 3.37d-f the Voronoi diagrams performed on an area of $1\mu\text{m}\times 1\mu\text{m}$ are reported, for acetone, toluene and water/toluene *RSA*, respectively.

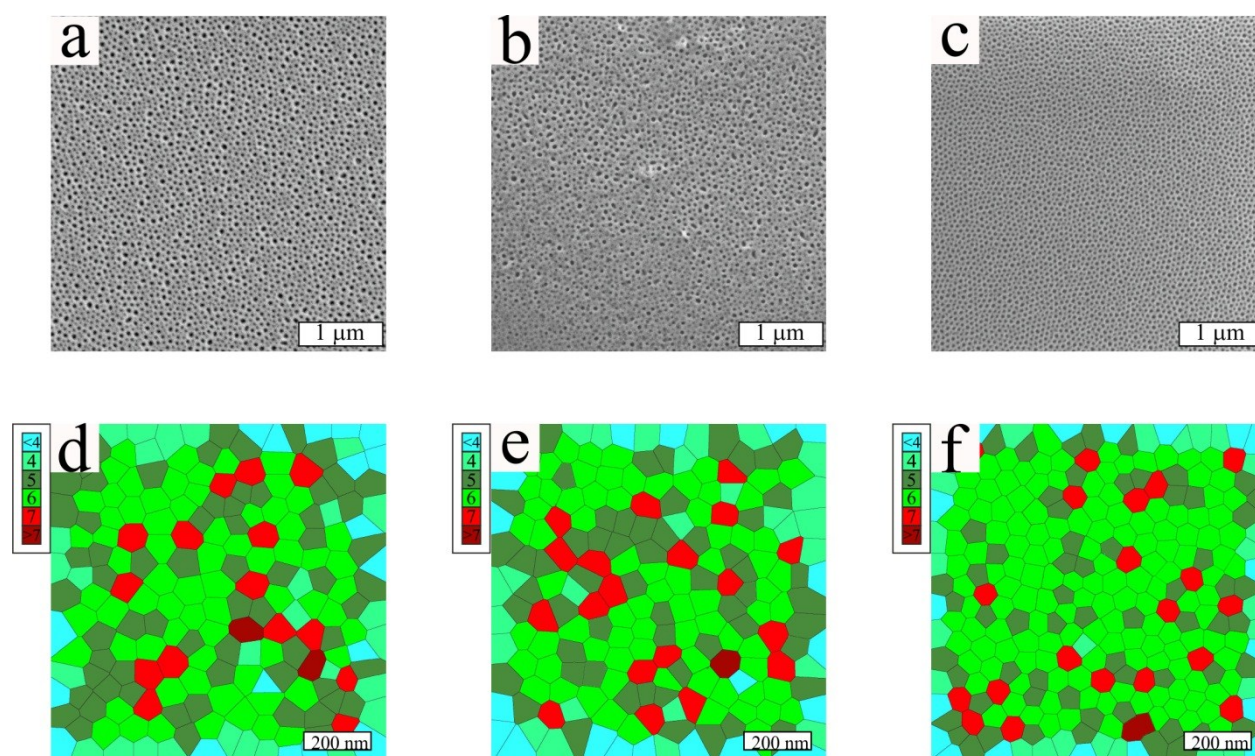


Figure 3.37: FESEM images of the neat SEO thin films spin-coated at 2500 rpm at room temperature after experiencing acetone (15 R.H.%) (a), toluene (22 R.H.%) (b) or water/toluene (60 R.H.%) (c) *RSA* annealing for 20''. The corresponding Voronoi constructions over $1\mu\text{m}\times 1\mu\text{m}$ squares are reported (d-f). On the top left of each image is depicted a legend highlighting the correspondences between colors and number of the side of the polygons.

The percentage of hexagons was 44% for acetone annealing, 49% after the toluene treatment and 70% when the vapor of the mixed solvent constituted by water and toluene was used for the rapid solvent annealing. Once again it was confirmed that the water/toluene annealing has

generated the best benefits for the lateral order of thin films of neat PS-*b*-PEO, as happened with the slower solvent annealing process.

The water/toluene *RSA* has constituted a good procedure to enhance the lateral order of the neat copolymer, as it appears in the bar diagram of Figure 3.38 where the percentage of hexagons achieved with the water/toluene mixed solvent and toluene by *SSA* and *RSA* is compared with that achieved with the untreated sample.

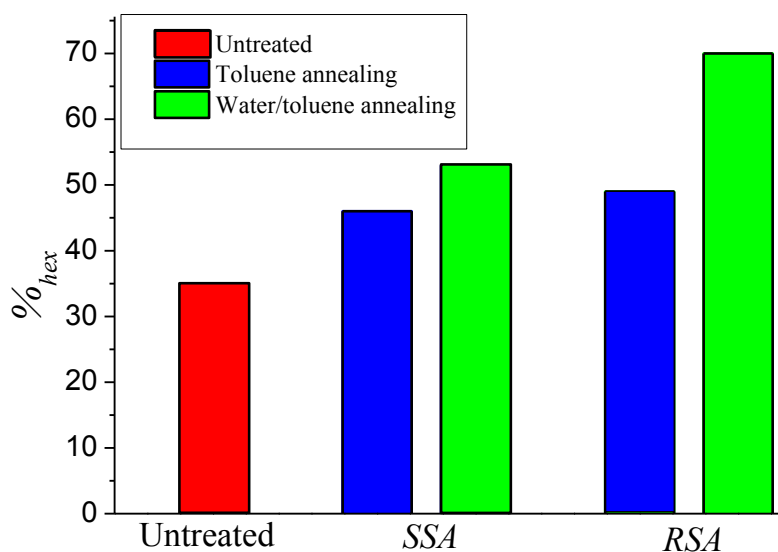


Figure 3.38: Bar diagrams depicting the percentage of hexagons counted with the Voronoi diagrams obtained from the untreated SEO (red bar), after toluene (blue bars) and water/toluene (green bars) *SSA* (Slow Solvent Annealing) and *RSA* (Rapid Solvent Annealing).

The third step was to evaluate the efficiency of the water/toluene *RSA* on the hybrid sample containing the 40 mol% of titanium precursor. In Figure 3.39a-c the FESEM images of the unannealed hybrid sample, of the water/toluene rapid solvent annealed sample (45 R.H.%) before and after the heat-treatment at 600°C for 4h are reported. The demonstration that a real improvement of long-range order was achieved came from the Voronoi analysis of images. The percentage of hexagons was doubled from 30% in the case of the unannealed sample to 60% for the thin film of the hybrid nanocomposite that has experienced water/toluene *RSA* for few seconds.

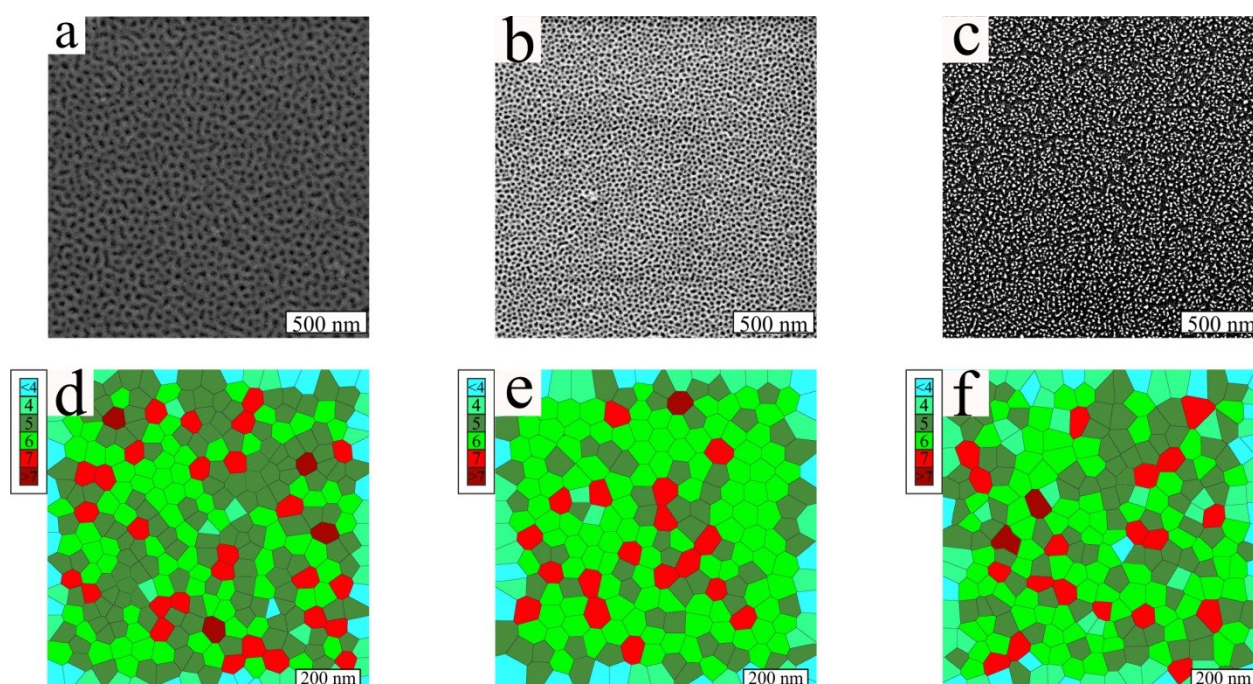


Figure 3.39: FESEM images of the hybrid SEO thin films containing 40 mol% of TTIP spin-coated at 2500 rpm at room temperature (a), after experiencing water/toluene *RSA* for 20'' (45 R.H.%) (b) and its corresponding heat-treated sample at 600°C for 4h (c). The relative Voronoi constructions of $1\mu\text{m}\times 1\mu\text{m}$ are reported (d-f). On the top left of each image is depicted a legend highlighting the correspondences between colors and number of the side of the polygons.

A good enhancement was achieved also on the heat-treated sample that derived from the hybrid thin film that experienced the water/toluene atmosphere. In the case of the heat-treated sample obtained from the untreated hybrid thin film (Figure 3.22e) it was not even possible to draw a Voronoi diagram because of the substantial ground noise of the image. For the *RSA* heat-treated sample a Voronoi construction of the image was possible obtaining a value for the percentage of hexagons equal to 40%.

The employment of this novel solvent annealing technique on the hybrid thin films has permitted to preserve quite well the pseudo-hexagonal order achieved with the neat sample also in the case of the heat-treated material. A further evidence that confirm the preservation of the sizes of the hybrid material derived from the dimensional analysis of Figure 3.40a,b.

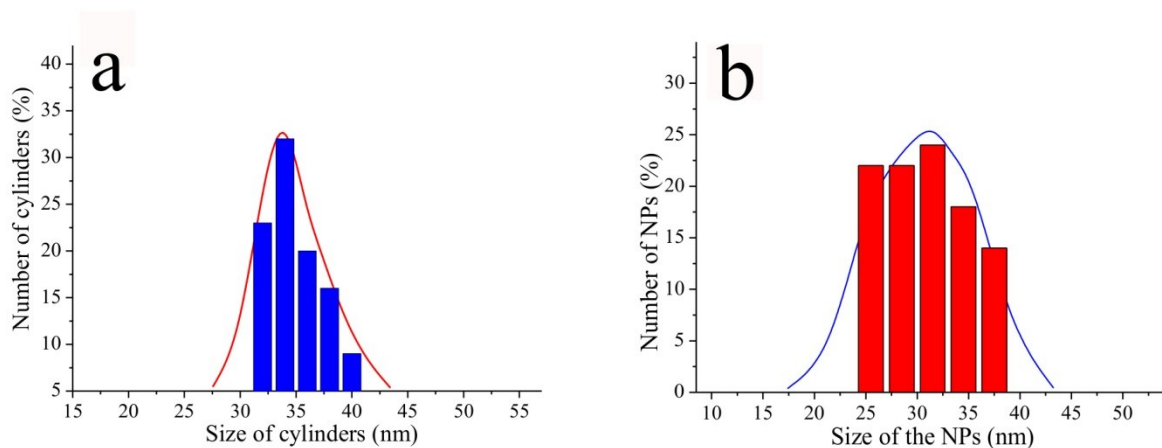


Figure 3.40: Bar diagrams representing the distribution of the size of cylinders (a) and TiO₂ nanoparticles (b) with their fitting curves calculated from FESEM images of Figure 3.39 b and c respectively.

The average size of the diameter of the top section of the PEO block in the organic/inorganic material was of 35 nm (Figure 3.40a). Although the thin film was subjected to an high temperature treatment the size of the resulting anatase nanoparticles was of 31 nm (see Figure 3.40b). This stimulating result represent an evident proof attesting that the PEO block acted properly as “host” toward the “guest” titania network that essentially retained its same dimensions.

3.8 Preparation of hybrid and heat-treated PS-*b*-PEO/Nb₂O₅ thin films

The reproducibility of the procedure that has led to the development of TiO₂/SEO hybrid thin films has been exploited changing the inorganic component of our nanocomposites. A precursor of the same class of the TTIP has been employed for this purpose: the niobium (V) ethoxide. As in the case of titanium oxide the formation of amorphous Nb₂O₅ and the obtainment of a crystalline inorganic network by heat-treatment were obtained following the same preparation procedure described in Paragraph 2.6.

In the early 90's transition metal oxides, e.g. oxides of tungsten (WO₃), molybdenum (MoO₃) and vanadium (V₂O₅) have been extensively investigated as electrochromic devices in the form of thin film adhering to a conducting substrate. Among them, niobium oxide⁸⁸ thin film prepared by the sol-gel process showed optimum electrochromic properties and higher coulombic efficiency.

More recently niobium oxide thin films produced by means of the sol-gel process has been used for the long-term success of skeleton implants such as artificial hip or knee joints as stable compound between the biomaterial and the surrounding tissue.⁸⁹ Because of its extremely high corrosion resistance and thermodynamic stability, Nb₂O₅ has demonstrated to be a promising material for application as an oxide coating for metallic implants.

The Nb₂O₅ has been employed also as photocatalysts.⁹⁰ A key point was the obtainment of mesoporous materials because of their special porous structures and considerable surface areas. These mesoporous structures were found to be active photocatalysts for photocatalytic hydrogen production.

Compared with the low activity of the bulk Nb₂O₅ powder, the mesoporous Nb₂O₅ catalysts showed superiority in photocatalytic activity mostly due to a low recombination rate of the photo-excited electrons and holes. This result assumed a significant value on improving the quantum efficiency of photocatalytic water splitting.

The most recent literature continued to show interest to the achievement of niobium oxide NPs with precise size. A surfactant-modified sol-gel process⁹¹ was employed to synthesize crystalline mesoporous Nb₂O₅ nanoparticles that possessed monomodal pore size distribution with uniform porous structure and exhibited UV lightresponding capability.

As previously performed on the titania sol-gel powders the characteristics of the niobium oxide xerogels have been studied by XRD measurements at different temperatures. The xerogel was obtained from the evaporation of the isopropanol solution containing niobium ethoxide and water (in a molar ratio 1:1) and was performed at different temperatures (up to 700°C).

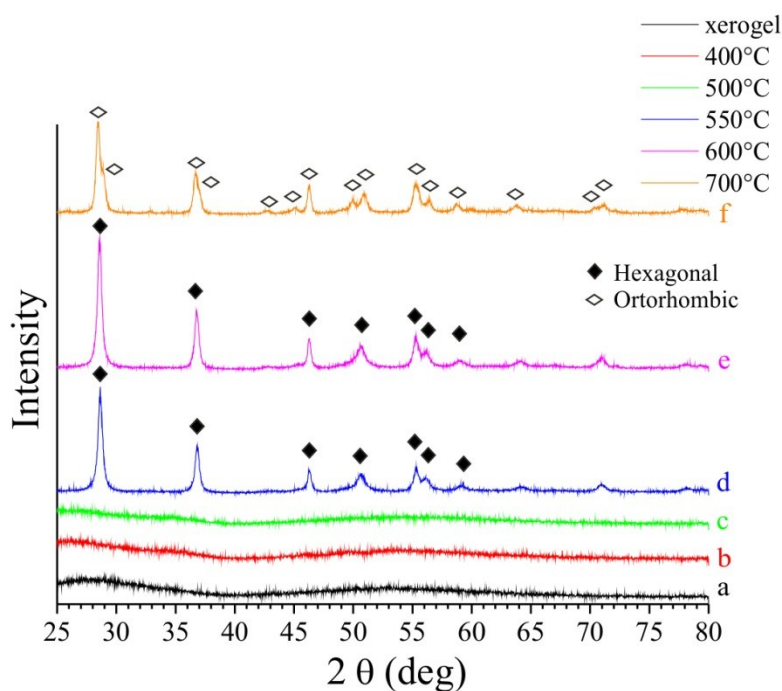


Figure 3.41: X-ray powder diffraction patterns of Nb_2O_5 powders heat-treated at different temperatures for 4 h in consecutive steps.

After heating at 500 °C, the sample remained amorphous (curve c of Figure 3.41). Upon heating at 550 °C the Nb_2O_5 crystallized in the hexagonal form (curve d of Figure 3.41). At 700 °C transformation of hexagonal form into the orthorhombic phase was observed (curve f of Figure 3.41).⁹²

The obtainment of SEO hybrid thin films by spin coating at 2500 rpm for 30 s at room temperature on Si wafers with increasing amount of niobium precursor (n Nb ethoxide/ n PEO m.u. = 1 mol%, 2.5 mol%, 10 mol%, 40 mol%, 80 mol%) was monitored by FESEM morphological analysis shown in Figures 3.42a-e.

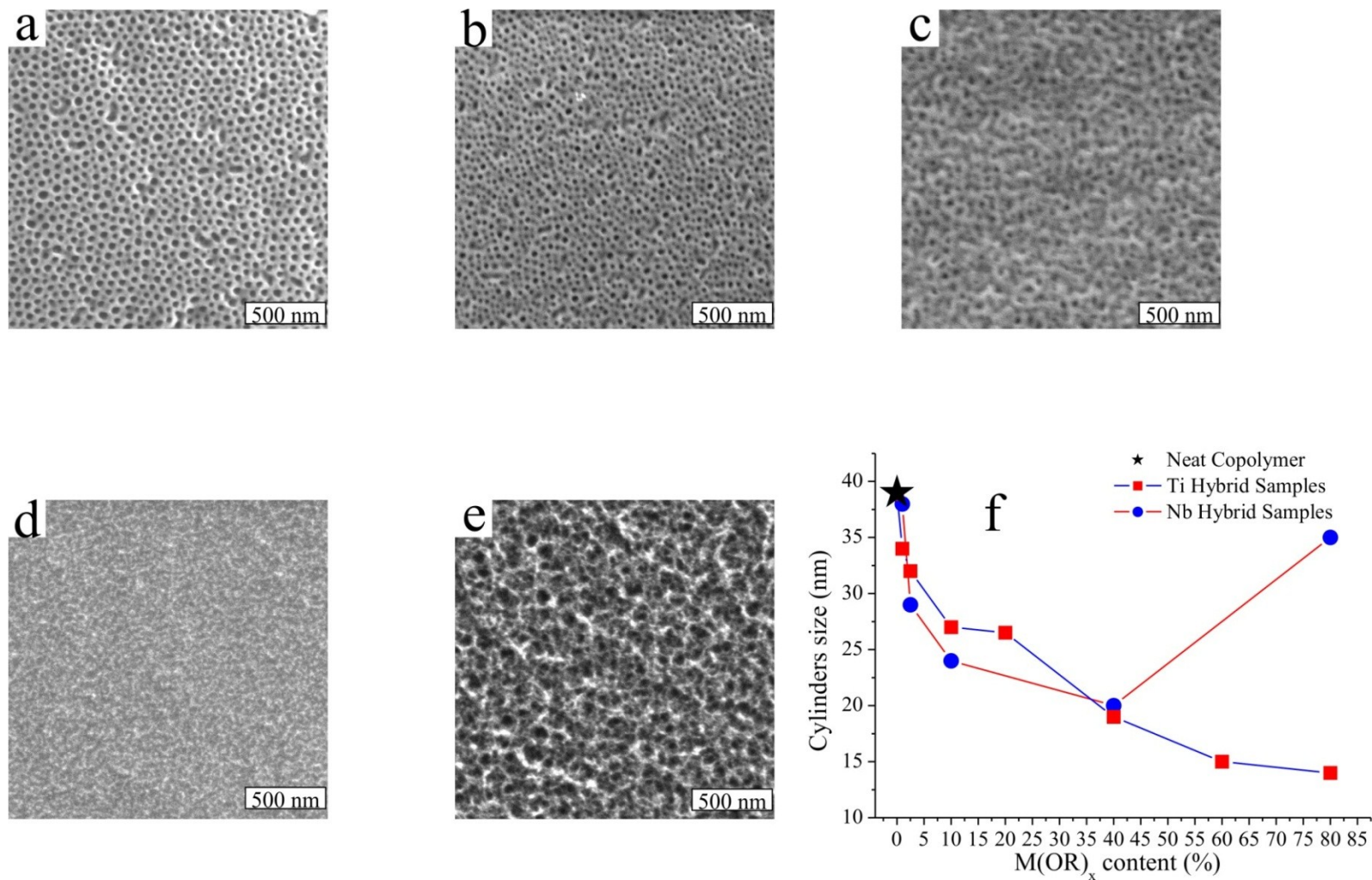


Figure 3.42: FESEM images ($2\mu\text{m} \times 2\mu\text{m}$) of the hybrid samples obtained by spin coating at 2500 rpm at room temperature loaded with increasing amounts of the sol-gel containing the Nb₂O₅ precursor which correspond to different values of Nb:PEO molar ratio [a) 1 mol%, b) 2.5 mol%, c) 10 mol%, d) 40 mol%, e) 80 mol%]. The values of the diameter (D) of the neat SEO and of the hybrid samples with different contents of Ti and Nb precursor are reported in f.

As depicted in Figure 3.42f the diameter of the top section of the cylinders of PEO loaded with the niobium ethoxide decreased up to sample containing 40 mol% of the alkoxide precursor. The last sample that contained the greatest niobium ethoxide loading (80 mol%) exhibited an inversion of that trend with D equal to 35 nm. The inorganic network was deposited mainly on the top of the surface of the organic template as reported in the FESEM image of Figure 3.42e. Probably the Nb precursor concentration was so elevated that the inorganic oxide polymerization took place principally outer of the PEO domains.

After the obtainment of the hybrid materials the next step was the achievement of ordered Nb₂O₅ NPs. The hybrid nanocomposites were annealed at 600°C at a rate of 2 °C min⁻¹ and were kept at that temperature for 4 h to be sure of the complete removal of the PS-*b*-PEO. Niobium pentoxide bright nanoparticles were clearly distinguished for all the compositions (Figure 3.43a-e) standing up on the surface of the substrate reminiscent of the morphology of the hybrid nanostructures.

The diameter of the nanoparticles originated from the sample containing 1 mol% of niobium precursor was 15.6 nm. With increasing content of Nb ethoxide all the heat-treated samples presented a progressively greater diameter of the NPs (see Figure 3.43f).

Once again this result can be interpreted comparing the values of D of the PEO domains that accommodated the inorganic oxides before their removal by heat-treatment and the diameter of the niobia NPs with increasing content of alkoxide precursor

Comparing the two curves relative to the hybrid and heat-treated Nb₂O₅/SEO samples it is apparent that the evolution of the size of the inorganic network is strictly related to the dimension of the PEO affine domains that were completely filled with 10 mol% of Nb alkoxide (D of PEO = 24 nm, D of the NPs = 26.5 nm). For the samples containing the 40 mol% and especially the 80 mol% of Nb precursor a very dense Nb₂O₅ weave was detected and the pseudo-hexagonal arrangement achieved for the other samples was gradually lost. This behavior was due on the one hand to the cosolvent effect/loss of crystallinity of the PEO domains that brought to a worsening of the lateral order, on the other to the high concentration of Nb₂O₅ precursor that induced an incipient formation of the metal oxide network before being accommodated into the hydrophilic domains. The diameter of the Nb₂O₅ NPs was smaller than the corresponding titania NPs for both 40 and 80% samples (D of Nb₂O₅ NPs = 28 and 33 nm; D of TiO₂ NPs = 16 and 17 nm).

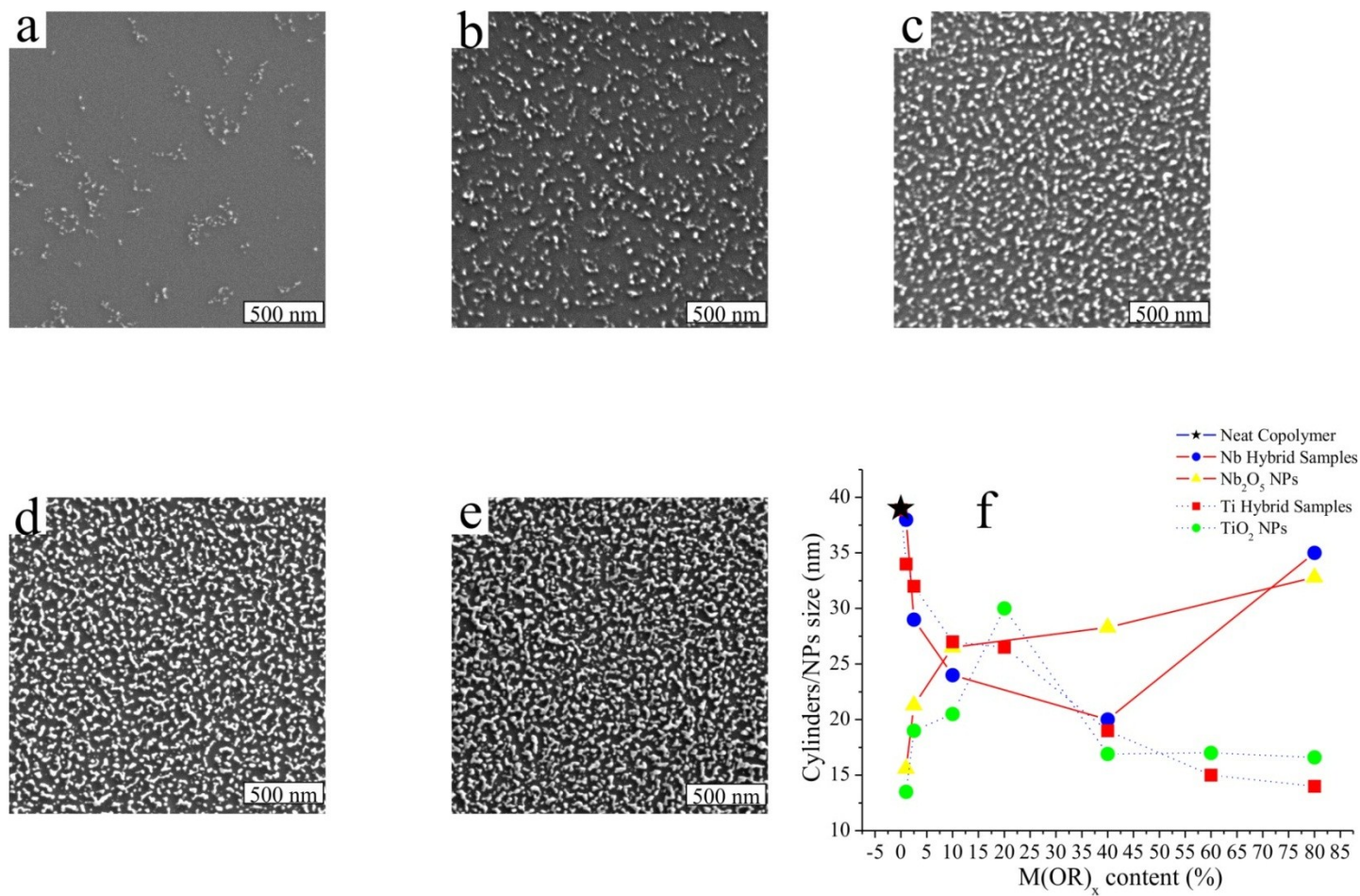


Figure 3.43: FESEM images ($2\mu\text{m} \times 2\mu\text{m}$) of the heat-treated (600°C at a rate of 2°C min^{-1} for 4) hybrid samples obtained by spin coating at 2500 rpm at room temperature loaded with increasing amounts of the sol-gel containing the Nb₂O₅ precursor which correspond to different values of Nb:PEO molar ratio [a) 1 mol%, b) 2.5 mol%, c) 10 mol%, d) 40 mol%, e) 80 mol%]. The values of the diameter (D) of the neat SEO, of the hybrid samples with different contents of alkoxide precursor and of Nb₂O₅/TiO₂ NPs are reported in f.

A FTIR study of the solutions of PS-*b*-PEO in toluene, of Ti and Nb alkoxides and of the hybrid solution with increasing amounts of loaded metal oxide precursor has been developed in order to understand their behavior and to evaluate the size differences between the two hybrid and heat-treated systems discussed just above .

Figure 4.44 shows the normalized FTIR spectra of neat SEO, TTIP and Nb (V) ethoxide and of the hybrid TiO₂ or Nb₂O₅/SEO. nanocomposites. In Table 3.9 the band assignments and their relative intensities are reported.

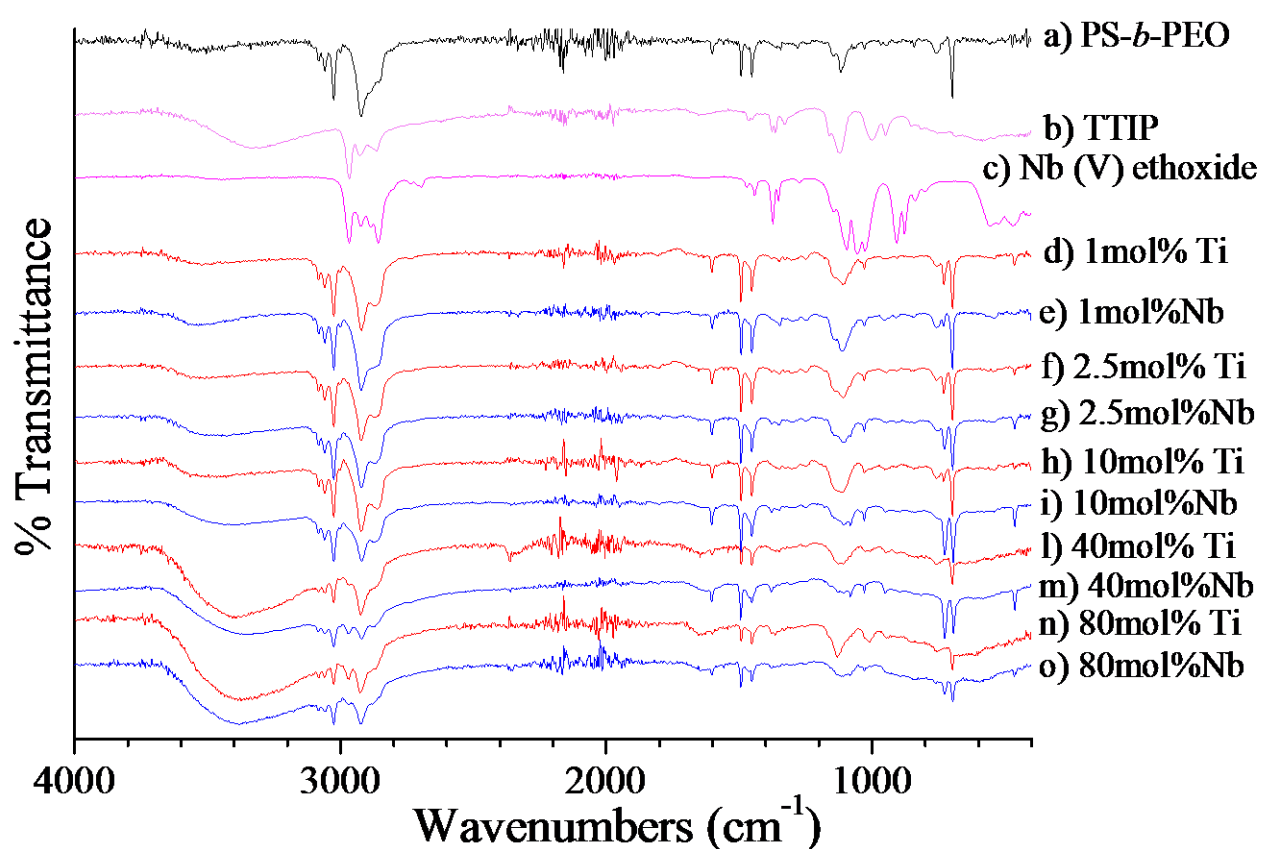


Figure 3.43: FTIR spectra relative to the PS-*b*-PEO solution (1 wt% in toluene), TTIP, Nb(OEt)₅ and the isopropanol/toluene SEO/TTIP and SEO/Nb (V) ethoxide solutions containing increasing amount of inorganic precursor (1 mol%, 10 mol%, 40 mol%, 80 mol%). FTIR spectra have been normalized for the band at 3025 cm⁻¹ (a, c-o spectra) and at 2968 cm⁻¹ (b,c spectra).

Table 3.9: FTIR infrared bands and corresponding assignments of PS-*b*-PEO, TTIP, Nb(OEt)₅ and of the hybrid samples.

PS- <i>b</i> -PEO bands (cm ⁻¹)	Assignments ^a	Hybrid samples bands (cm ⁻¹)	Assignments ^a
3026-2924	v (C-H)vs	3710-3169	v (Ti-OH)b
1600-1472	v (Phenyl ring) s	3026-2924	v (C-H)vs
1118	v (C-O) m	1600-1472	v (Phenyl ring) s
756-698	oop δ (C-H) m-s	1378	δ (CH ₂ ,CH ₃)w
Nb (V) ethoxide bands (cm⁻¹)		1120	v (C-O) m-w
2967-2858	v (C-H)vs	729-698	oop δ (C-H) m-w
1440-1373	δ (CH ₂ ,CH ₃)m-s	463	v (Ti-O-Ti)m-w
1055	v (C-O) vs		
557-470	v (Nb-O)s		
TTIP bands (cm⁻¹)			
3340	v (Ti-OH)b		
2968-2863	v (C-H)vs		
1458-1369	δ (CH ₂ ,CH ₃)w-m		
1054	v (C-O) vs		
633	v (Ti-O)b		

^a Relative intensities: w, weak; m, medium; s strong; vs, very strong.

The metal oxide precursors spectra showed stretching and bending vibrations related to the -CH₂ and -CH₃ of their alkoxide groups [v (C-H) at ~ 2967-2860 cm⁻¹; δ (CH₂, CH₃) ~ 1450-1370 cm⁻¹]. A very strong band attributed to the stretching of the C-O bond appeared at ~ 1055 cm⁻¹ whereas at lower frequencies were present bands relative to M-O bonds [557-470 cm⁻¹ for v (Nb-O) and 633 cm⁻¹ for v (Ti-O)].

The PS-*b*-PEO and the hybrid samples spectra showed a characteristic band between 3026 and 2924 cm⁻¹ relative to the stretching of the alkyl groups [v (C-H)], followed by the styrene ring stretches at 1600-1472 cm⁻¹ and the ring CH out-of-plane deformation (756-698 cm⁻¹). The medium v C-O band centered at 1118 cm⁻¹ was more and more weak with increasing

loading of sol-gel precursor.⁹³ This estimation coupled with the appearance for the hybrid samples of a large broad band between 3710–3169 cm^{-1} (attributed to stretching vibrations of Ti–OH groups, also present for TTIP) and an increasingly strong band for increasing precursor loadings assigned to the stretching of the M–O–M (M= Ti or Nb) bond at 463 cm^{-1} were evidences of the generations of the inorganic metal oxide network.

In the case of the nanocomposites, the associated hydroxyl group band of the precursor shifts to lower frequencies with increasing sol–gel contents. This fact suggested that the OH groups of the metal oxide networks interacted by hydrogen bonding with the PEO domain of the block copolymer, as also suggested by Li et al for TiO_2/PCL nanocomposites⁹⁴ and by Gutierrez et al for TiO_2/SEO .⁵⁹

In any case comparing each pair of samples containing the same percentage of the two metal oxide precursors the broad [ν (M–OH)] band was always shifted to lower frequencies for the $\text{Nb}_2\text{O}_5/\text{SEO}$ nanocomposites. Consequently the interactions by hydrogen bonds between the niobium pentoxide network and the PEO domains increased comparing to the TiO_2/SEO nanocomposites. This behavior was probably related to a faster kinetic of the sol-gel reaction of the niobium alkoxide that could be related to a greater charge to radius ratio⁹⁵ for Nb (V) than Ti(IV) and a smaller steric hindrance of the ethoxide groups than the isopropoxide ones.

Bibliography of Chapter III

1. Grulke, E. A., J. Brandup, and E. H. Immergut. *Polymer Handbook* **1999** Wiley, New York.
2. Muller A.J., Balsamo V., Arnal M.L., Jakob T., Schmalz H., Abetz V. *Macromolecules* **2002**, *35*, 3048-3058
3. Chen, H.; Hsiao, S.; Lin, T.; Yamauchi, K.; Hasegawa, H.; Hashimoto, T. *Macromolecules* **2001**, *34*, 671.
4. Chen, H.; Wu, J.; Lin, J. *Macromolecules* **2001**, *34*, 6936.
5. Lheritier J., Chauvet A., Masse J., *Thermochim. Acta* **1994**, *241*, 157.
6. Sun Z., Kim D.H., Wolkenhauer M., Bumbu G.G., Knoll W., Gutmann J.S., *Chem. Phys. Chem.* **2006**, *7*, 370-378.
7. (a) Chen W., Li C.Y., Zheng J.X, Huang P., Zhu L., Ge Q., Quirk R.P., Lotz B., Deng L., Wu W., Thomas E.L., Cheng S.Z.D., *Macromolecules* **2004**, *37*, 5292-5299. (b) Zhu, L.; Cheng, S. Z. D.; Calhoun, B. H.; Ge, Q.; Quirk, R.P.; Thomas, E. L.; Hsiao, B. S.; Yeh, F.; Lotz, B. *Polymer* **2001**, *42*, 5829.
8. Trent J.S., Sceinbeim J.I., Couchman P.R., *Macromolecules* **1983**, *16*, 589-598.
9. Diebold U., *Surf. Sci. Rep.* **2003**, *48*, 53-229.
10. C.N. Satterfield, *Heterogeneous Catalysis in Industrial Practice*, 2nd ed., McGraw-Hill, New York, **1991**.
11. Biener J, Wang J., Madix R.J., *Surf. Sci.* **1999**, *442*, 47.
12. Guo Q., Lee S., Goodman D.W. *Surf. Sci.* **1999**, *437*, 38.
13. M. Sambì, G. Sangiovanni, G. Granozzi, F. Parmigiani *Phys. Rev. B* **1996**, *54*, 13464.
14. Haller G.L., Resasco D.E., *Adv. Catal.* **1989**, *36*, 173.
15. Dulub O., Hebenstreit W., Diebold U. *Phys. Rev. Lett.* **2000** *84*, 3646.
16. Ando M., Kobayashi T., Haruta M. *Catal. Today* **1997**, *36*, 135.
17. Fujishima A., Honda K. *Nature* **1972**, *238*, 37.
18. Lo W.J., Chung Y.W., Somorjai G.A. *Surf. Sci.* **1978** *71*, 199.
19. Rajeswar K., *J. Appl. Electrochem.* **1985**, *15*, 1.
20. Mills A., Davies H.R., Worsley D. *Chem. Soc. Rev.* **1993**, *22*, 417.
21. Maness P.-C, Smolinski S., Jacoby W.A. *Appl. Environ. Microbiol.* **1999**, *65*, 4094.
22. Paz Y., Luo Z., Rabenberg L., Heller A. *J. Mater. Res.* **1995** *10*, 2842.
23. Poulìos I., Spathis P., Tsoumparis P. *J. Environ. Sci. Health* **1999**, *34*, 1455.

24. Sakai H., Baba R., Hashimoto K., Kubota Y., Fujishima A., *Chem. Lett.* **1995**, *24*, 185.
25. *Gas Sensors*; Sheveglieri, G., Ed.; Kluwer Academic Publishers: Dordrecht, 1992.
26. Dutta P.K., Ginwalla A., Hogg B., Patton B.R., Chwieroth B., Liang Z., Gouma P., Mills M., Akbar S., *J. Phys. Chem.* **1999** *103*, 4412
27. Phillips L.G., Barbano D.M., *J. Dairy Sci.* **1997**, *80*, 2726
28. Hewitt J., *Cosmet. Toiletries* **1999** *114*, 59.
29. Selhofer H., *Vacuum Thin Film* **1999**, 15.
30. Campbell S.A., Kim H.-S., Gilmer D.C., He B., Ma T., Gladfelter W.L., *IBM J. Res. Devlop.* **1999**, *43*, 383.
31. Matsumoto Y., Shono T., Hasegawa T., Fukumura T., Kawasaki M., Ahmet P., Chikyow T., Koshihara S., Koinuma H., *Science* **2001** *291*, 854.
32. Bonhote P., Gogniat E., Grätzel M., Ashrit P.V., *Thin Solid Films*, **1999** *350*, 269.
33. Barteau M.A., *J. Vac. Sci. Technol. A* **1993**, *11*, 2162.
34. Grant F.A., *Rev. Mod. Phys.* **1959**, *31*, 646.
35. Samsonov G.V., *The Oxide Handbook* **1982** IFI/Plenum Press, New York.
36. Diebold U., Specimen treatment: preparation of metal compound materials (mainly oxides), in: C.A. Czanderna, C.J. Powell, T.E. Madey (Eds.), *Specimen Handling, Treatments, Beam Effects and Depth Profiling*, vol. 4, **1999**.
37. Ramamoorthy M., Vanderbilt B., *Phys. Rev. B* **1994**, *49*, 16721.
38. Zangwill A., *Physics at Surfaces*, Cambridge, **1988**.
39. Vittadini A., Selloni A., Rotzinger F.P., Grätzel M., *Phys. Rev. Lett.* **1998**, *81*, 2954.
40. Hoyer P., *Langmuir* **1996**, *12*, 1411.
41. Liu S.M., Gan L.M., Liu L.H., Zhang W.D., Zheng H.C., *Chem. Mater.* **2002**, *14*, 1391.
42. Burnside S.D., Shklover V., Barbe C., Comte P., Arendse F., Brookes K., Grätzel M., *Chem. Mater.* **1998**, *10*, 2419.
43. Zhu Y.C., Ding C.X., *Nanostruct. Mater.* **1999**, *11*, 427.
44. Iida M., Sasaki T., Watanabe M., *Chem. Mater.* **1998**, *10*, 3780.
45. Yin Y., Lu Y., Gates B., Xia Y. *Chem. Mater.* **2001**, *13*, 1146.
46. Schüth F., *Chem. Mater.* **2001**, *13*, 3184.
47. Yang P., Zhao D., Margolese D.I., Chmelka B.F., Stucky G.D., *Nature* **1998**, *396*, 152.
48. Cheng Y., Gutmann J.S., *J. Am. Chem. Soc* **2006**, *128*, 4658-4674.

49. Cullity B.D., *Elements of X-ray Diffraction*, **1978**, Addison-Wesley, Reading, MA.
50. Liu X., *Powder Technol.* **2012**, *224*, 287-290.
51. Wang S.F., Gu F., Lu M.K., Song C.F., Liu S.W., Xu D., Yuan D.R.; *Mat. Res. Bull.* **2003**, *38*, 1283–1288.
52. S. Musić, M. Gotić, M. Ivanda, S. Popović, A. Turković, R. Trojko, A. Sekulić, K. Furić, *Mat. Sci. Eng. B* **1997**, *47*, 33–40.
53. Dobrescu G., Crişan M., Zaharescu M. Ionescu N.I., *Mater. Chem. Phys.* **2004**, *87*, 184-189.
54. Kim D.H., Sun Z., Russell T.P., Knoll W., Gutmann J.S., *Adv. Funct. Mater* **2005**, *15*, 1160-1164.
55. Seo Y., Kim M.W., Ou-Yang D.H., Peiffer D.G., *Polymer* **2002**, *43*, 5629.
56. Jeong U., Ryu D.Y., Kho D.H., Lee D.H., Kim J.K, Russell T.P., *Macromolecules* **2003**, *36*, 3626-3634.
57. Krause S., in *Polymer Blends*, Paul D.R. and Newman S., Eds. (Academic Press, New York, **1978**), vol. 1, pp. 16–113.
58. Robeson L., in *Polymer Compatibility and Incompatibility*, Solc K., Ed. (MMI Press Symposium Series, Harwood Academic, New York, **1982**), vol. 2, pp. 177–211.
59. Gutierrez J., Tercjak A., Garcia I., Peponi L. Mondragon I., *Nanotechnology* **2008**, *19*, 155607.
60. Templin M., Franck A., Du Chesne A., Leist H., Zhang Y., Ulrich R., Schädler V., Wiesner U., *Science* **1997**, *278*, 1795.
61. Yeh S-W., Wei K-H., Sun Y-S., Jeng U-S., Liang K.S., *Macromolecules* **2003**, *36*, 7903-7907.
62. Zhou C-H., Zhao X-Z., Yang B-C., Zhang D., Li Z-Y., Zhou K-C., *J. Colloid Interf. Sci.* **2012**, *374*, 9-17.
63. Sung Y-M., Lee J-K., Chae W-S., *Crystal Growth & Design* **2006**, *6*, 805-808.
64. Sung Y-M., Lee Y-J., Lee S-M., *J. Cryst. Growth* **2004**, *267*, 312-316.
65. Hamley I.W., *Prog. Polym. Sci.* **2009**, *34*, 1161-1210.
66. Fukunaga K., Elbs H., Magerle R., Krausch G., *Macromolecules* **2000**, *33*, 947–53
67. Kim S.H., Misner M.J., Xu T., Kimura M., Russell T.P., *Adv. Mater.* **2004**, *16*, 226–31.
68. Kim S., Briber R.M., Karim A., Jones R.L., Kim H.C., *Macromolecules* **2007**, *40*, 4102–5.

69. Niu S., Saraf R.F., *Macromolecules* **2003**, *36*, 2428–40.
70. Kim S.H., Misner M.J., Yang L., Gang O., Ocko B.M., Russell T.P., *Macromolecules* **2006**, *39*, 8473–9.
71. Chen Y., Huang H., Hu Z., He T., *Langmuir* **2004**, *20*, 3805–8.
72. Tokarev I., Krenek R., Burkov Y., Schmeisser D., Sidorenko A., Minko S., *Macromolecules* **2005**, *38*, 507–16.
73. Blanks R.G., Prausnitz J.M., *Ind. Eng. Chem. Fund.* **1964**, *3*, 1.
74. Chen S-A., *J. Appl. Polym. Sci.* **1971**, *15*, 1247–1266.
75. Chen Y., Huang H., Hu Z., He T., *Langmuir* **2004**, *20*, 3805–3808.
76. Grozea C.M., Li I.T.S., Grozea D., Walker G.C., *Macromolecules* **2011**, *44*, 3901-3909.
77. Bang J., Kim B.J., Stein G.E., Russell T.P., Li X., Wang J., Kramer E.J., Hawker C.J., *Macromolecules* **2007**, *40*, 7019-7025.
78. Berg, M. D. *Computational Geometry: Algorithms and Applications*, 2nd rev. ed.; Springer: Berlin, **2000**.
79. Segalman R.A., Hexemer A., Kramer E.J., *Macromolecules* **2003**, *36*, 6831-6839.
80. Hammond M.R., Sides S.W., Fredrickson G.H., Kramer E.J., *Macromolecules* **2003**, *36*, 8712-8716.
81. Park S., Lee D.H., Xu J., Kim B., Hong S.W., Jeong U., Xu T., Russell T.P., *Science* **2009**, *323*, 1030-1033.
82. Xu J. Russell T.P., Ocko B.M., Checco A., *Soft Matter* **2011**, *7*, 3195-3919.
83. Lin E. K., Gast A. P., *Macromolecules* **1996**, *29*, 4432-4441.
84. Zheng, J. X., Xiong H., Chen W. Y., Lee K., Van Horn R. M., Quirk R. P., Lotz B., Thomas E. L., Shi A.-C., Cheng S. Z. D., *Macromolecules* **2006**, *39*, 641-650.
85. Huang W., Luo C., Zhang J., Yu K., Han Y., *Macromolecules* **2007**, *40*, 8022-8030.
86. Yang P., Han Y., *Macromol. Rapid Commun.* **2009**, *30*, 1509-1514.
87. Sasaki T., Miyazaki A., Sugiura S., Okada K., *Polym. J.* **2002**, *34*, 794.
88. Ohtani B., Iwai K., Nishimoto S., Inui T., *J. Electrochem. Soc.* **1994**, *141*, 2339-2442.
89. Velten D., Eisenbarth E., Schanne N., Breme J., *J. Mater. Sci-Mater. M.* **2004**, *15*, 457-461.
90. Chen X. Yu T., Fan X., Zhang H., Li Z., Ye J., Zou Z., *Appl. Surf Sci.* **2007**, *253*, 8500-8506.
91. Sreethawong T., Ngamsinlapasathian S., Yoshikawa S., *Mater. Lett* **2012**, *78*, 135-138.

92. Paulis M., Martín M., Soria D.B.; Díaz A., Odriozola J.A., Montes M., *Appl. Catal. A-Gen.* **1999**, *180*, 411-420.
93. Kobayashi M., Nakaoki T., *Macromolecules* **1989**, *22*, 4377-4382.
94. Li R., Nie K., Shen X., Wang S., *Mater. Lett.* **2007**, *61*, 1368-1371.
95. Khairou K.S., Al-Gethami W.M., Hassan R.M., *J. Membrane Sci.* **2002**, *209*, 445-456.

CHAPTER IV

BCP/TiO₂ hybrid and heat-treated materials as soot sensors

4.1 Conductivity for soot sensing

It is well-known that aerosol particles have a significant influence on the climate, environment, and human health.¹ The source of an aerosol is multiple and can be of natural and anthropogenic origin. Subtypes of atmospheric particle matter (see Figure 4.1), also known as particulate matter (PM), include suspended particulate matter (SPM), respirable suspended particle (RSP; particles with diameter of 10 micrometres or less), fine particles, and soot.

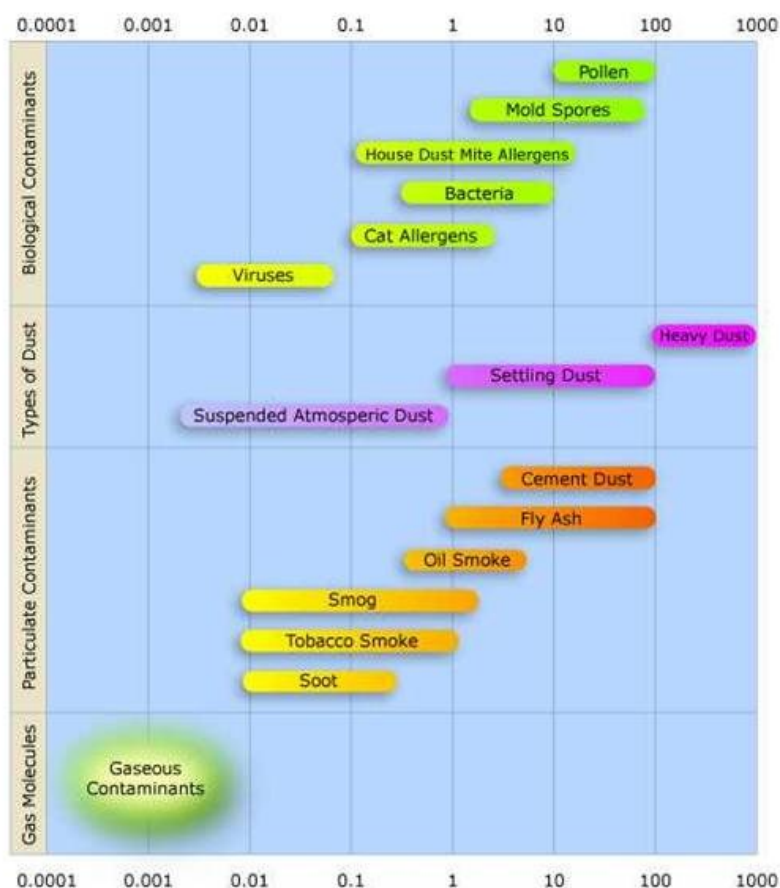


Figure 4.1: Diagram showing the size distribution in micrometres of various types of atmospheric particulate matter. It also shows the different types of particulates in the atmosphere

Especially in urban areas, soot nanoparticles, emitted by diesel engines (commonly referred to as Diesel Particulate Matter, or DPM), pose a health risk.^{2,3} Particles smaller than 100 nanometers can pass through cell membranes and migrate into other organs, including the brain. It has been suggested that particulate matter can cause similar brain damage as that found in Alzheimer patients. Particles emitted from modern diesel engines are typically in the size range of 100 nanometers (0.1 micrometer). In addition, these soot particles also carry carcinogenic components like benzopyrenes adsorbed on their surface. It is becoming increasingly clear that the legislative limits for engines, which are in terms of emitted mass, are not a proper measure of the health hazard. One particle of 10 μm diameter has approximately the same mass as 1 million particles of 100 nm diameter, but it is clearly much less hazardous, as it probably never enters the human body — and if it does, it is quickly removed.

Only in 2008 the European Parliament enacted new directives (2008/50/EC) regarding the emission of PM_{10} and $\text{PM}_{2.5}$ and adopted a proposal for new legislation limiting the exhaust emissions of engines installed in heavy duty vehicles.

Upcoming regulations for vehicle emissions require the removal of particulate emissions from diesel engines. For that reason, trapping systems and exhaust after-treatment technologies are currently under investigation. In practice, ceramic wall-flow diesel particle filters (DPF) have been generally enforced to reduce mass as well as particle number with a filtration efficiency up to 97%.⁴ Because of increasing back-pressure, the DPF has to be regenerated periodically by gasification of the deposited soot. The efficiency of the regeneration step is affected by the oxidation reactivity of the deposited soot, which mainly depends on the microstructure of the soot particles.⁵ In order to reduce energy consumption of the filter regeneration step, the formation of highly reactive soot would be an advantage. Since DPFs can be damaged by thermal and mechanical forces, an on-board control is necessary for premature detection of a malfunction of DPF systems. Thus cheap and reliable tools are demanded to detect and analyze soot particles online. Nowadays there are several standard techniques available for soot analysis. To get a detailed knowledge about the oxidation/gasification of soot, usually thermo-analytical methods are used. Gasification kinetics are measured by thermo-gravimetric analysis (TGA) or by temperature-programmed oxidation (TPO).⁶ This is achieved by determining either the mass loss of the sample (TGA) or the gasification products by mass spectrometry or infrared spectroscopy (TPO). For investigation of the soot structure, usually high-resolution transmission electron microscopy (HRTEM) is applied, but for routine analysis this is too demanding.⁵ An alternative to the imaging of the structure by HRTEM are

advanced X-ray diffraction (XRD) methods. These scattering techniques allow detailed information about structure and chemical composition in a nanoscale range.⁷ A very promising and currently used technique for a rapid, robust, and nondestructive determination of the soot structure is Raman spectroscopy. In combination with an optical microscope, Raman microspectroscopy (RM) provides a structural characterization of the carbonaceous compounds by a vibrational fingerprint spectra with a spatial resolution in the micrometer range.⁸⁻⁹ The characteristic position, the width and the intensity of the peaks, i.e., G (graphite) and D (defect), etc., supply information about the graphite-like and amorphous carbon as well as impurities in the sample¹⁰ and can also be connected to the oxidation behavior of soot.¹¹ Moreover a wide range of online and in situ techniques for particle detection and characterization are available. An application which uses the detection of positively charged particles, formed by the photoelectric effect, is the aerosol photoemission (APE) sensor. The APE measures the mass concentration of particulate matter and the effect is strongly influenced by the surface properties of the particles, due to the different work-functions of the coating materials like polyaromatic hydrocarbons (PAH).¹² Laser-induced incandescence (LII) can be either used to determine soot mass or the size distribution by measuring the radiation of the particles, heated by a short laser pulse.¹³ A photoacoustic soot sensor (PASS) was used by Grob et al.¹⁴ recently, which was based on the absorption of modulated light by the soot particles. The absorbed energy was heating the particle and led to a thermal expansion, which created a modulated acoustic wave with the frequency of the modulation of the light source. The intensity of the modulation was proportional to the absorbed energy. The advantage of the PASS is the very low detection limit of around $2 \mu\text{g m}^{-3}$ and its temporal response in the order of one second.¹⁵ Concerning the high costs, the energy demand, and the geometrical dimension of the described techniques, some developments of new detection methods are done especially for the DPF on-board monitoring. Beside some ideas about optical and discharge sensors, it seems that the most promising are conductometric soot sensors. Their main advantages are the simple principle, low costs, and especially their small dimension, which make them suitable for on-board monitoring of particulate matter emissions of diesel engines. There are a few different developments published, which show that these sensors can be suitable for particulate emission control.¹⁶⁻¹⁷ All of them are using the signal response of resistance decrease between interdigital electrodes, due to the deposition of soot particles, whereas the particle sampling methods of the published developments varies. In this study we discuss the

fabrication and the employment of a conductometric soot sensor and the impact of TiO₂ inorganic oxide on the conductivity of carbonaceous materials.

4.2 Conductometric soot sensor: experimental setup

The typology of sensors used to investigate the effect of soot particles between electrodes is illustrated in Figure 4.2. The SEO/TiO₂ hybrid solutions with different contents (10 and 40 mol%) of titania precursor (step 1) or the isopropanol/toluene 0.0125 M TTIP solution (step 1') were spin-coated at 2500 rpm for 30 seconds at room temperature onto the side of the Si wafers (Siltronix ; 10 mm x 10 mm x 500 μm) with a non-conductive SiO₂ layer of 250 nm thickness. The so-obtained thin films were heat-treated at 600°C (2°C/min for 4 hours) to remove the organic matrix and obtain the anatase crystalline form.

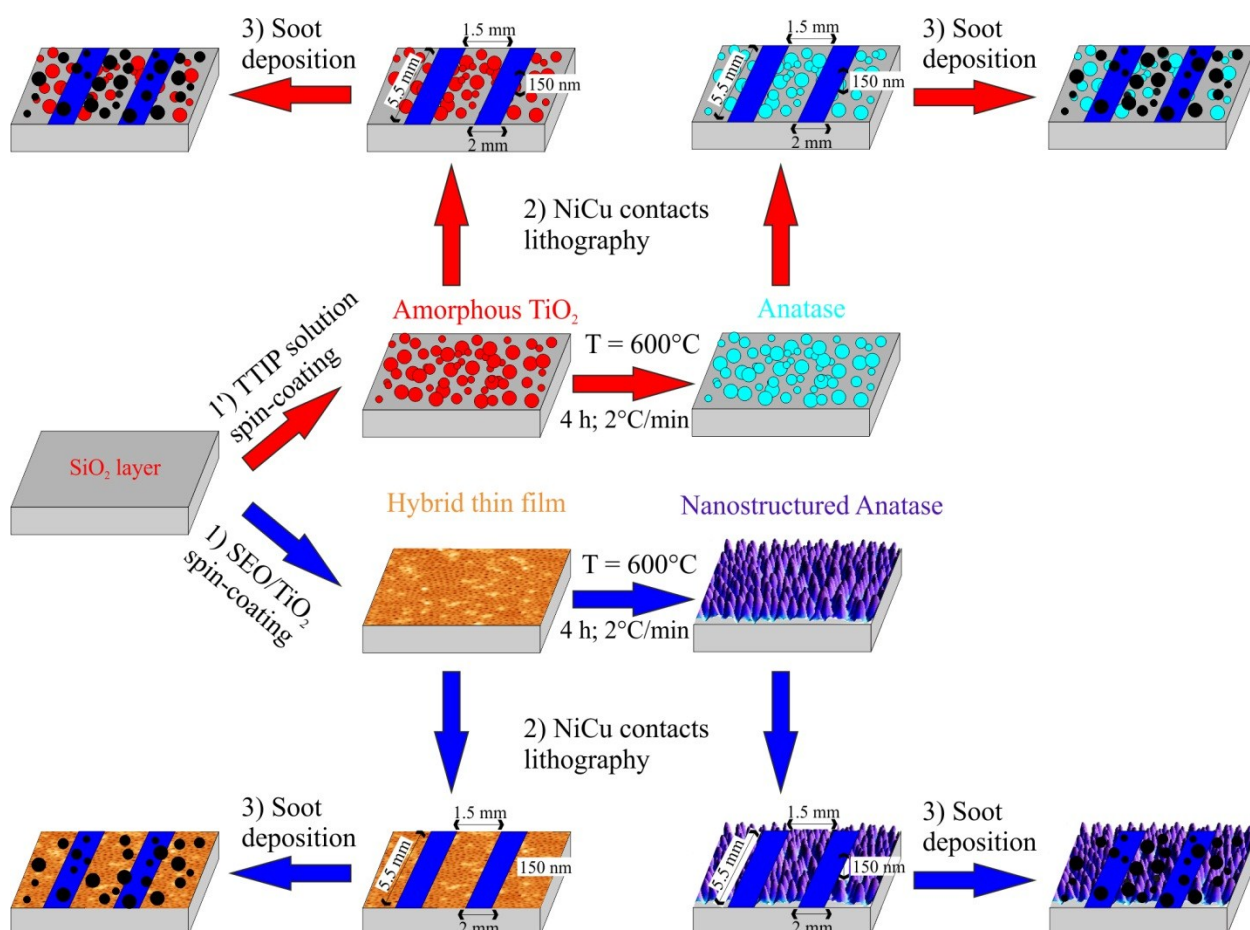


Figure 4.2: SEO/TiO₂ or 0.0125 M TTIP precursor solution were spin-coated at 2500 rpm at room temperature as thin films onto a Si/SiO₂ substrates (step 1,1') and then heat-treated at 600°C for 4 h. Ni-Cu contacts were deposited by sputtering on the specimens (step 2). Soot nanoparticles were deposited on the surface of the contacted samples (step 3).

Two Ni-Cu contacts were deposited by sputtering on the nanostructured thin films according to a parallel electrodes geometry depicted in step 2 of Figure 4.2. Soot NPs were deposited on the Ni-Cu contacted samples as last stage (step 3).

4.2.1 Soot deposition

Soot nanoparticles were produced using a flat atmospheric pressure laminar premixed flames at the Combustion Research Institute of Naples (in collaboration with Ing. Mario Commodo and Dr. Patrizia Minutolo) whose combustion conditions can be easily varied.¹⁸ The very simple fluid-dynamics allows processes to be followed along the flame axis to obtain kinetics data. Modeling can be performed using detailed kinetic schemes containing hundreds of species and thousands of reactions. Fuel-rich premixed hydrocarbon flames exhibit a typical luminous structure: a blue region close to the burner due to the large formation of OH radicals in the flame front followed by an almost transparent region and downstream by a zone with intense yellow-orange luminosity due to soot particles incandescence emission. This zone becomes more evident as the C/O ratio of the fuel-air mixture is increased. The transparent region is observed in flames of aliphatic hydrocarbons, but vanishes for an aromatic fuel because the yellow-orange zone overlaps with the blue zone.

The flame luminosity structure is well described by the elastic laser light scattering along the flame axis. Figure 4.3 reports the scattered light signal intensity along the flame axis of a C/O = 0.77 ethylene/air flame with a cold-gas flow velocity of 10 cm/s which is here taken as a test case.¹⁹⁻²⁰

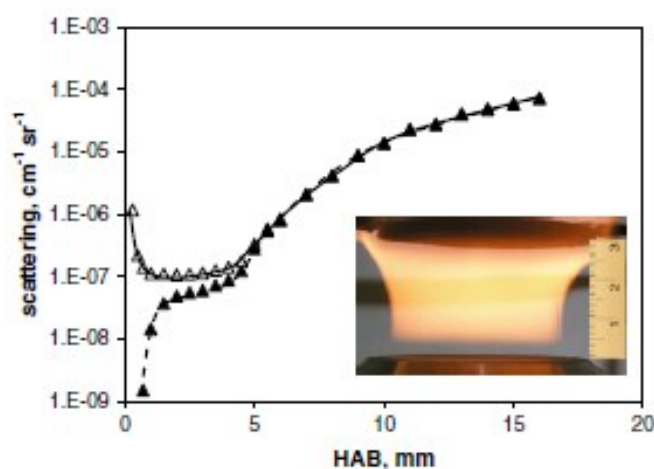


Figure 4.3: Scattered light signal intensity at 266 nm (Δ) measured along the flame axis of a slightly-sooting, C/O = 0.77, ethylene/air flame with a cold gas flow velocity of 10 cm/s. \blacktriangle represents the scattering in excess to gaseous species.¹⁸

A strong scattering signal is detected at the exit of the burner; it decreases moving away from the burner exit up to a minimum value followed by a plateau region and a strong scattering region downstream. The decrease of the scattering signal is due to the increase of the flame temperature in the region of the intense blue luminosity, the plateau region corresponds to the transparent region and the strong increase of the scattering signal corresponds with the yellow-orange luminosity. Scattering signal can be attributed to gas and condensed phases on the basis of the extinction spectra. The spectrum measured in the blue region of the flame shows a UV signal which decays at increasing wavelength and vanishes at about 300 nm. Moving downstream from the flame location, the UV signal increases and some absorption in the visible starts to be detected. The visible absorption becomes significant at higher flame heights in the yellow-orange region. Figure 4.4 shows typical extinction spectra measured in the $C/O = 0.77$ ethylene flame at two locations (HAB: height above the burner), namely 4 mm, in the transparent region downstream of the flame zone (Figure 4.4 – upper part) and 8 mm, in the yellow-orange zone (Figure 4.4 –lower part).

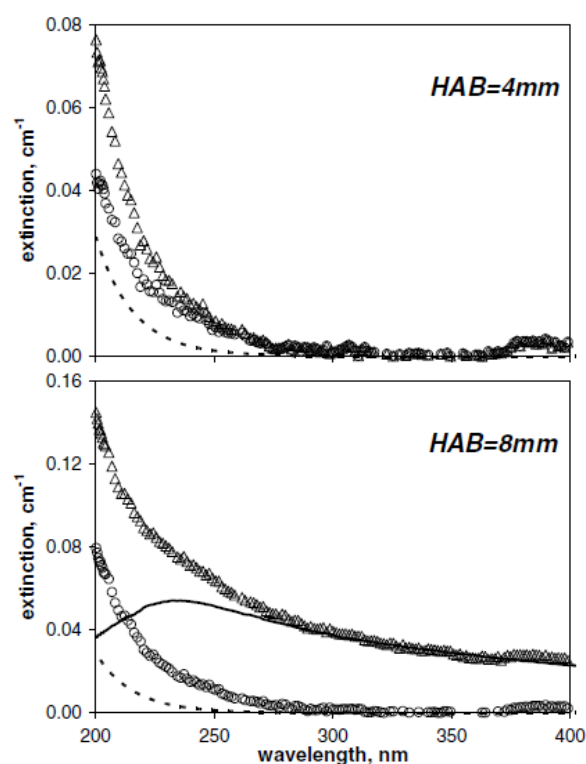


Figure 4.4: Extinction spectra measured at 4 mm (upper) and 8 mm (lower) from the burner outlet in a slightly-sooting, $C/O = 0.77$, ethylene/air flame with a cold gas flow velocity of 10 cm/s. Δ represents the measured data; dashed lines are the contribution of CO_2 and H_2O to the extinction spectrum; continuous line is the typical absorption spectrum of soot; \circ represents the extinction subtracted by the contribution of soot, CO_2 and H_2O .¹⁸

The UV absorption in the range 200-250 nm can be attributed to H₂O and CO₂ molecules which have been found to exhibit strong absorption at high temperature.²¹⁻²²

Figure 4.4 reports as dashed lines the contribution of CO₂ and water molecules to the absorption spectra estimated from gas concentrations predicted by kinetic modeling and estimated absorption cross sections at flame temperatures. The absorption in the visible range reported in the lower part of Figure 4.4 is due to soot particles. In the UV the contribution of soot particles to absorption can be estimated from the typical absorption spectrum of soot measured on a quartz disk reported as a thin line in the Figure 4.4. By subtracting the contribution of gaseous products and soot absorption from the spectra of Figure 4.4 there is still extra absorption in the UV which has to be attributed to other UV-absorbing, visible-transparent molecules/particles. It is interesting to note that the spectral behavior of the excess absorption in the UV remains quite unchanged in the two flame locations reported; it shows strong absorption in the UV which decays at increasing wavelength and vanishes at about 300 nm.

In our study the employed C/O ratio was 0.85 (HAB = 15mm) which produced soot nanoparticles ranging from tens to hundreds of nanometers. This has been measured from the AFM height image of Figure 4.5a. The size of soot NPs were very similar to the carbonaceous nanoparticles at the exhaust of a diesel vehicle as reported in Figure 4.5b.

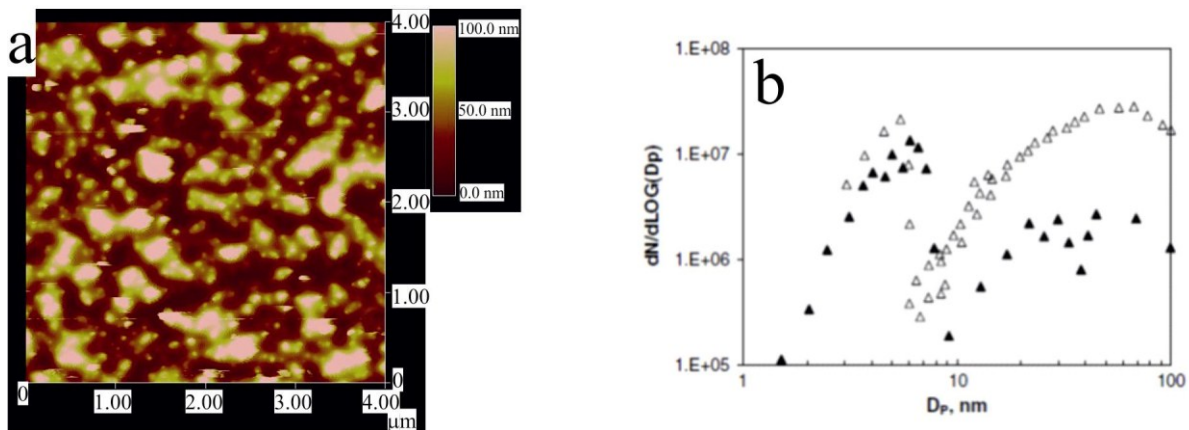


Figure 4.5: a) AFM height image of the soot deposited on a clean Si wafer using a premixed flame (C/O ratio = 0.85, HAB = 15mm); b) Particle size distribution measured by AFM (▲) and DMA (Δ) at the exhaust of a diesel vehicle.¹⁸

The height of the soot nanoparticles of figure 4.5a ranged from 150 to 250 nm and the arithmetic average value of roughness R_a was 23.6 nm.

Particles were sampled via thermophoresis by rapidly inserting the substrate into the flame. Several insertions (*number of insertions*) were performed for each substrate in order to increase the amount of particles samples. Indeed, this procedure permitted to accumulate on the same sample increasing amounts of soot until a change in conductivity can be detected. Also a spectroscopic analysis was performed in order to obtain a correspondence between the number of insertions and the amount of the deposited soot. The measure of the absorbance of the carbonaceous materials for any successive deposition has allowed to calculate the thickness l of the deposited material using eq.1 and 2:

$$A = \varepsilon l c = \frac{l \alpha}{2.303} \quad (1)$$

$$\alpha = \frac{4\pi\kappa}{\lambda} \quad (2)$$

with A representing the absorbance, ε the molar absorption coefficient, l the thickness of the deposited soot, α the absorption coefficient, κ the imaginary part of the refractive index and λ the wavelength of absorption at 532 nm.

Assuming as soot density the value $\rho = 1.8 \text{ g/cm}^3$ it was possible to calculate the mass per unit area ($\mu\text{g/cm}^2$).²³

Several measurements of absorbance were recorded for increasing soot depositions on different samples spin-coated at 2500 rpm at room temperature on corning 7059 barium borosilicates (SEO/10 mol% and 40 mol% TiO_2 , their corresponding heat-treated samples at 600°C for 4 h, the 0.0125 M TTIP solution and its corresponding heat-treated sample at 600 °C for 4h) and on the corning glass itself. These measurements helped understanding if the nature of the sampling surface could affect the interaction properties with respect to the soot particles. An increasing number of insertions with *insertion step* = 5 was performed to deposit particles on the different specimens.

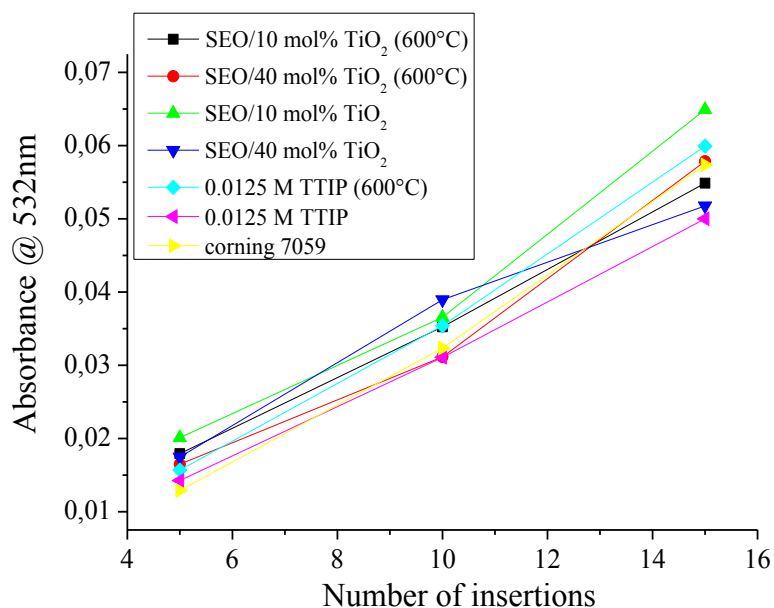


Figure 4.6: Absorbance plots in function of increasing number of insertions on the sole corning 7059, thin films of the hybrid and heat-treated samples containing a Ti/PEO m.u. molar ratio of 10 and 40 mol% , the isopropanol/toluene solution containing 0.0125 TTIP M before and after heat-treatment at 600°C for 4h spin-coated on corning 7059 at 2500 rpm for 30 seconds at room temperature.

Since the values of absorbance, as depicted in the graph of Figure 4.6, for the various depositions on the different samples were very similar, there is no preferential interaction between the specimens and the soot. The small variations of absorbance for each number of insertions could be ascribed to pressure fluctuations in the cold gas flows feeding the flame that was otherwise controlled by means of mass flow-meters.

4.2.2 Electrical Measurements

The electric transport measurements have been carried out when increasing amounts of soot were deposited by increasing number of insertions on the patterned samples (that in the following we define as “sensors”). The values of absorbance of a clean corning glass loaded with the same number of insertions have been measured simultaneously to quantify properly the amount of deposited carbonaceous material on the sensors.

The two-probe technique was used to measure the dc conductivity of the samples within the area included between electrodes. The measurements have been carried out at the Physics Laboratories of the University of Naples “Federico II” (in collaboration with Dr. Carmela Bonavolontà). From the current-voltage characteristics (I-V) the electrical resistance values for each sample have been estimated. It was validated that the voltage-current characteristic was Ohmic in nature, as reported in Figures 4.7-10.

At the beginning, soot depositions on the sole Si/SiO₂ wafer were carried out. It could be noted, as depicted from the I/V curves of Figure 4.7, that in this case there is not a change in conductivity for any amount of deposited soot.

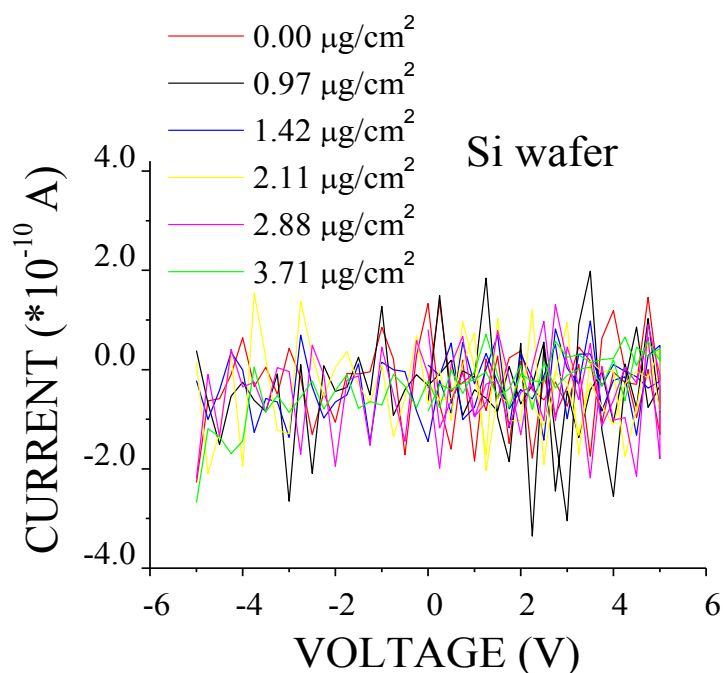


Figure 4.7: I/V graphs obtained for successive deposition of carbonaceous materials (C/O = 0.85) on Si/SiO₂.

An appreciable change of conductivity resulted after the deposition of 1.45 µg/cm² on the sample where the isopropanol/toluene solution 0.0125 M TTIP was spin-coated on Si/SiO₂ wafer at 2500 rpm at room temperature. The same behavior was detected for the corresponding heat-treated (at 600°C for 4h) 0.0125 M TTIP sample (see Figures 4.8a,b). Moreover, hysteresis phenomena for the latter two samples at high values of deposited soot (2.66 and 3.20 µg/cm²) are present. This result could be addressed to heating effects produced probably by the presence of a uniform thick layer of carbonaceous material.

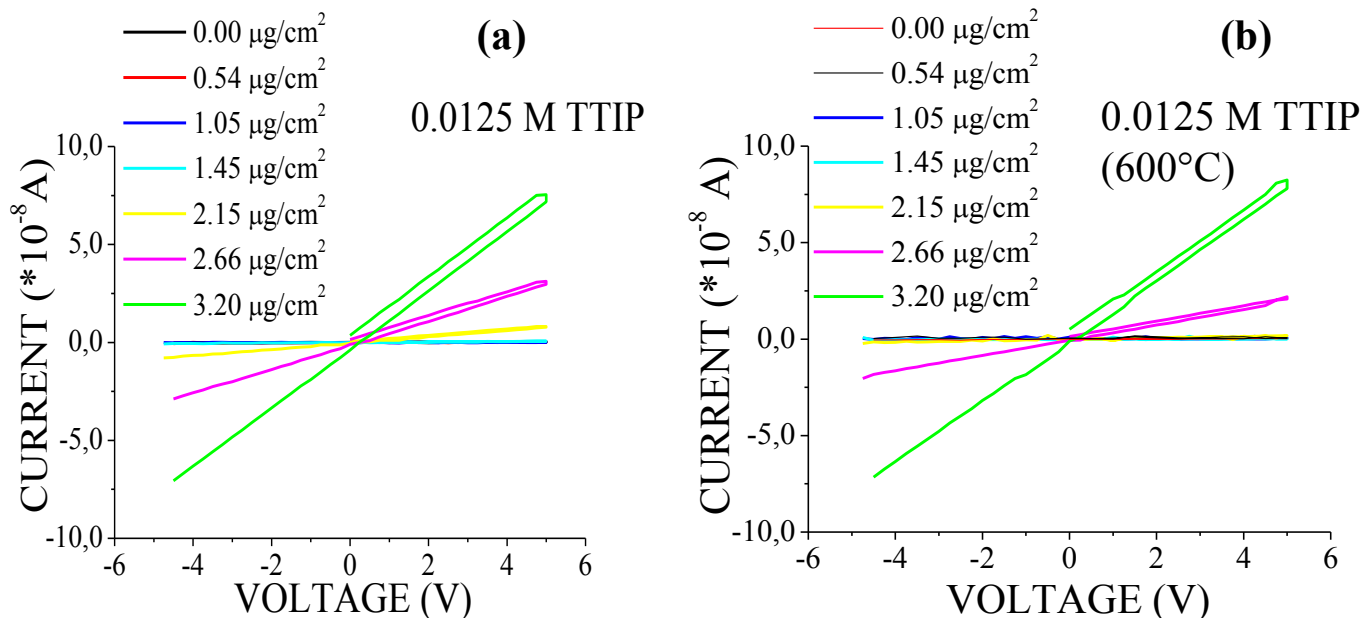


Figure 4.8: I/V graphs obtained for successive deposition of carbonaceous materials ($C/O = 0.85$) on thin films of the isopropanol/toluene solution 0.0125 M TTIP before (a) and after heat-treatment at 600°C for 4h (b).

However, the hybrid thin films containing 10% and 40 mol% of titania precursor showed a slower activation process that corresponded to a tangible change of conductivity. These two hybrid sensors started to conduct when 2.11 $\mu\text{g}/\text{cm}^2$ were deposited on their surface as reported in Figures 4.9a,b.

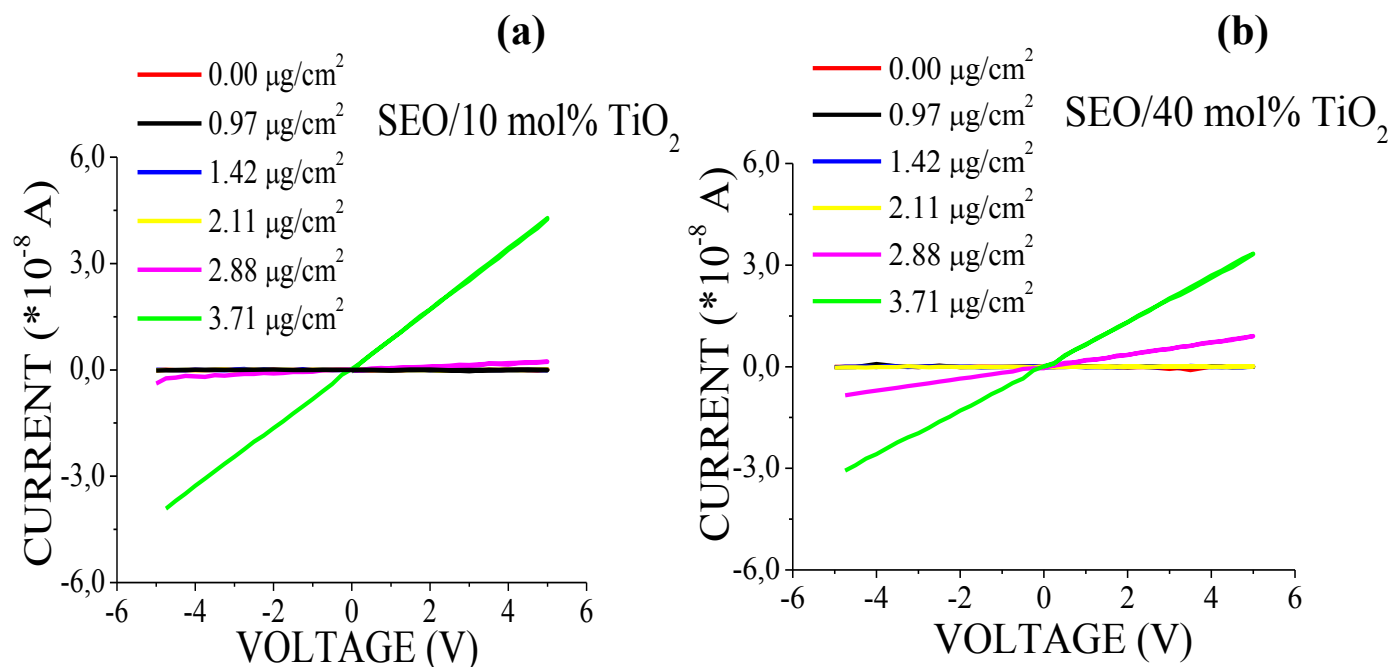


Figure 4.9: I/V graphs obtained for successive deposition of carbonaceous materials ($C/O = 0.85$) on thin films of the hybrid samples containing a Ti/PEO m.u. molar ratio of 10 mol% (a) and 40 mol% (b).

Their corresponding heat-treated samples (600°C for 4h) were activated after 1.45 $\mu\text{g}/\text{cm}^2$ of deposited soot showing a more sensitive behavior (see Figures 4.10a,b) if it is compared to their hybrid counterparts.

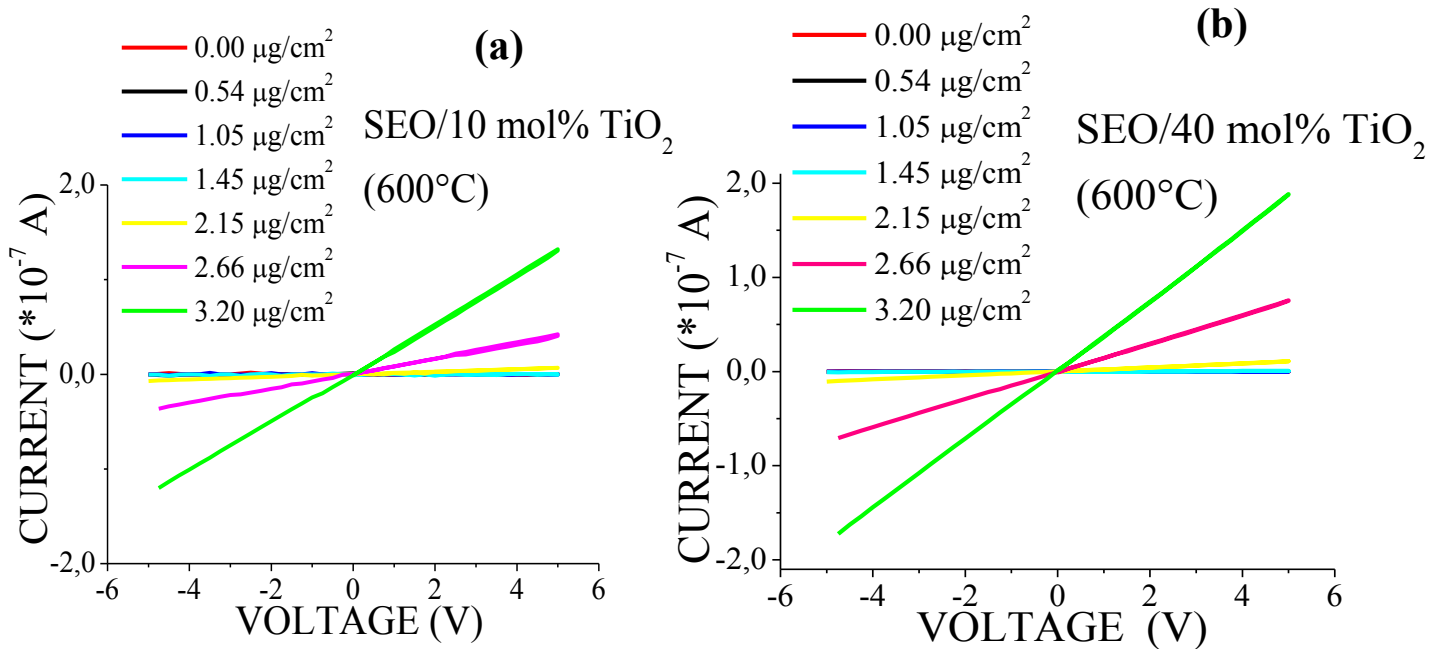


Figure 4.10: I/V graphs obtained for successive deposition of carbonaceous materials ($C/O = 0.85$) on thin films of the heat-treated (600°C at a rate of $2\text{ }^\circ\text{C min}^{-1}$ for 4h) hybrid samples containing a *Ti/PEO m.u.* molar ratio of 10 mol% (a) and 40 mol% (b).

The values of resistance as function of soot amount for all the samples are summarized in Figure 4.11. The inorganic heat-treated thin films have an activation threshold at 1.45 $\mu\text{g}/\text{cm}^2$ rather below the hybrid sensors that give an appreciable change of electrical conductivity after the deposition of 2.11 $\mu\text{g}/\text{cm}^2$. However these systems are much more sensitive with respect to the only Si/SiO₂ wafer which reaches values of resistance of the order of 10^4 - $10^5\text{ M}\Omega$ only after large soot loadings.

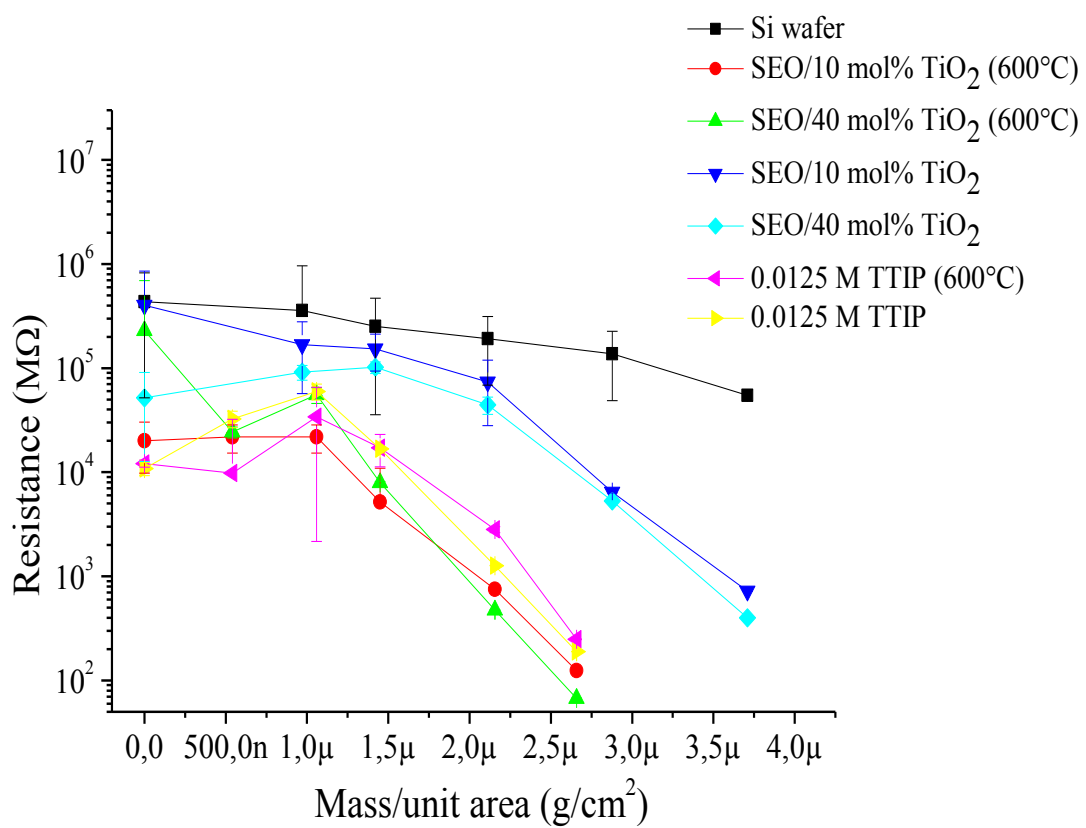


Figure 4.11: Electrical resistance vs the mass per unit area of the deposited soot.

A stepwise decrease of the resistance at a critical concentration p_c suggests that an infinite soot percolative network has been formed through the matrix. The critical concentration is located around 1.45–2.11 mg/cm². For depositions above p_c , the trend can be described by the scaling law:²⁴⁻²⁶

$$\sigma \propto (p-p_c)^t \quad (1)$$

This so-called percolation theory assumes a cluster formation of conductive and nonconductive clusters in the sample. With increasing amounts of the conductive compound, the probability of physical conducting pathways through the sample increases.

However, the percolation theory does not take into account the morphology of the aggregates of the conductive and nonconductive compounds, which influence the physical contact between the two phases. Another point is that conductance only occurs due to a physical contact between conducting aggregates in the percolation network. Therefore, thermal fluctuation-induced tunnelling can be a mechanism, which allows the conduction of electrons through insulating gaps.¹⁴ It has been shown that such a system can be described by a single junction where the conductivity σ is related to the gap w :²⁷

$$\sigma = \exp(-2\chi w) \quad (2)$$

whereas:

$$\chi = (2mV(T)/\hbar)^{1/2} \quad (3)$$

depends on the charge carrier mass m and the temperature dependent barrier height $V(T)$.

If the soot dispersion in the insulating matrix is homogeneous, the composite conductivity at a given temperature can be described by the behavior of a single tunnel junction, and the gap width can be assumed to be $w \propto p^{-1/3}$.^{28,29}

The expected linear relation between $\ln\sigma$ and $p^{-1/3}$ (expressed in our case as a mass per unit area) is shown in Figure 4.12, suggesting that tunneling conduction may be present in our samples.

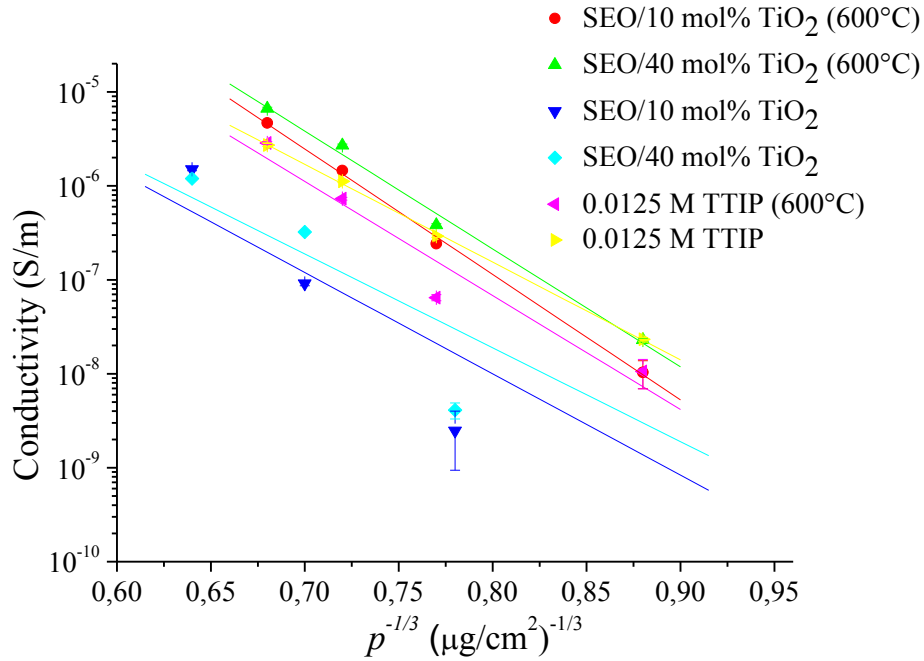


Figure 4.12: Logarithm of the conductivity σ dependent on the inverse of the cubic root of the mass per unit area of soot p for the hybrid and heat-treated (600°C for 4h) thin films obtained by spin coating at 2500 rpm at room temperature containing 10 mol% and 40 mol% of TiO₂ and thin films obtained by spin coating a 0.0125 M TTIP solution at 2500 rpm at room temperature and then heat-treated (600°C for 4h).

The standard deviation of the linear fits showed that the tunneling conduction was verified especially for the inorganic samples [SEO/10 mol% and 40% TiO₂ (600°C) and 0.0125 M TTIP] with the exception of 0.0125 M TTIP thin film heat-treated at 600°C. The hybrid thin films, instead, showed a relevant deviation from the linearity.

However, since the morphology of thin films obtained from a 0.0125 M TTIP solution (at room temperature and after heat treatment) is not controllable for the absence of a self-assembly matrix, the condition of the tunneling conduction could be not reproducible.

Table 4.1: Standard deviation calculated from the linear fits of Figure 4.12 for different samples

Sample	Standard deviation
SEO/10 mol% TiO ₂ (600°C)	0.06135
SEO/40 mol% TiO ₂ (600°C)	0.11417
0.0125 M TTIP	0.03234
0.0125 M TTIP (600°C)	0.32151
SEO/10 mol% TiO ₂	0.75281
SEO/40 mol% TiO ₂	0.71569

This behavior was probably related to the nature of the different samples. When $1.45 \mu\text{g}/\text{cm}^2$ (p_c) were deposited on the heat-treated thin films containing the 10 mol% and 40 mol% of TiO₂ (see Figure 4.13a) the soot could penetrate the titania “nanostalagmites” that acted as tunnel junction between the isolated carbonaceous material. However when the same loading was deposited on their corresponding hybrid samples (as reported in Figure 4.13b) the percolation paths were interrupted because the soot could not penetrate the organic matrix.

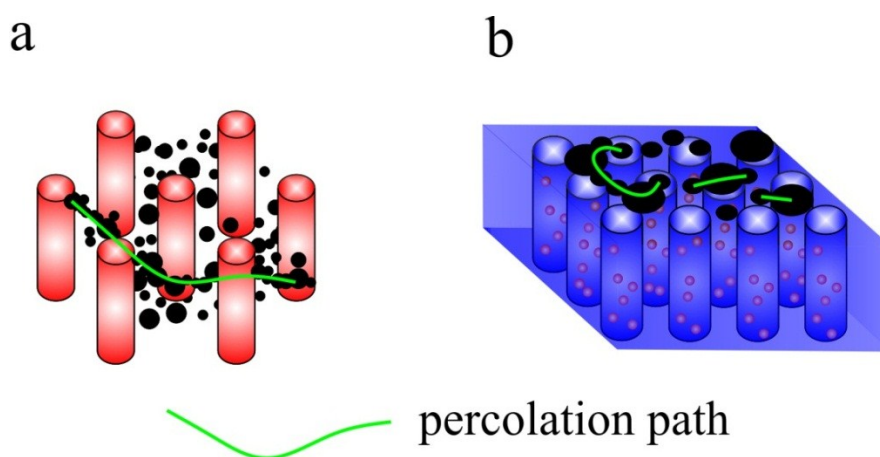


Figure 4.13: Percolation paths enabled after $1.45 \mu\text{g}/\text{cm}^2$ of soot deposition on the heat-treated thin films that presented titania nanostalagmites (a) on their surface and on the hybrid thin films with the same content of TiO₂ precursor.

Bibliography of Chapter IV

1. Bernstein J. A., Alexis N., Barnes C., Bernstein I. L., Nel A., Peden D., Diaz-Sanchez D., Tarlo S. M., Brock Williams P., *J. Allergy Clin. Immunol.* **2004**, *114*, 1116–1123.
2. Sydbom A., Blomberg A., Parnia S., Stenfors N., Sandström T., Dahlen S., *Eur. Respir. J.* **2001**, *17*, 733–746.
3. Lighty J. S., Veranth J. M., Sarofim A. F., *J. Air Waste Manage. Assoc.* **2000**, *50*, 1565–1618.
4. Johnson T., *SAE Int. J. Fuels Lubr.* **2008**, *1*, 68–81.
5. Müller J. O., Su D. S., Jentoft R. E., Wild U., Schlögl R., *Environ. Sci. Technol.* **2006**, *40*, 1231–1236.
6. Stanmore B. R., Brilhac J. F., Gilot P., *Carbon* **2001**, *39*, 2247–2268.
7. Maricq M. M., *J. Aerosol Sci.* **2007**, *38*, 1079–1118.
8. Rosen H., Novakov T., *Nature* **1977**, *266*, 708–710.
9. Knauer M., Carrara M., Rothe D., Niessner R., Ivleva N. P., *Aerosol Sci. Technol.* **2009**, *43*, 1–8.
10. Ferrari A. C., Robertson J., *Phys. Rev. B* **2000**, *61*, 14095–14107.
11. Schmid, J., Grob B., Niessner R., Ivleva N. P., *Anal. Chem.* **2011**, *83*, 1173–1179.
12. Niessner R., *J. Aerosol Sci.* **1986**, *17*, 705–714.
13. Hofeldt D. L., *Soc. Autom. Eng. [Spec. Publ.] SP* **1993**, *SP-957*, 33–45.
14. Grob B., Schmid J., Ivleva N.P., Niessner R., *Anal. Chem.* **2012**, *84*, 3586–3592.
15. Beck H. A., Niessner R., Haisch C., *Anal. Bioanal. Chem.* **2003**, *375*, 1136–1143.

16. Hagen G., Feistkorn C., Wiegärtner S., Heinrich A., Brüggemann D., Moos R., *Sensors* **2010**, *10*, 1589–1598.
17. Malik A., Abdulhamid H., Pagels J., Rissler J., Lindskog M., Nilsson P., Bjorklund R., Jozsa P., Visser J., Spetz A., *Aerosol Sci. Technol.* **2011**, *45*, 284–294.
18. D’Anna A., *Proceedings of the Combustion Institute* **2009**, *32*, 593–613.
19. D’Alessio A., D’Anna A., Gambi G., Minutolo P., *J. Aerosol Sci.* **1998**, *29*, 397.
20. Minutolo P., Gambi G., D’Alessio A., Carlucci S., *Atmos. Environ.* **1999**, *33*, 2725.
21. Jensen J., Guettler R.D., Lyman J.L., *Chem. Phys. Lett.* **1997**, *277*, 356.
22. Joutsenoja T., D’Anna A., D’Alessio A., Nazzaro M.I., *Appl. Spect.* **2001**, *55*, 130.
23. Choi M. Y., Mulholland G. W., Hamins A., Kashiwagi T., *Combust. Flame* **1995**, *102*, 161-169.
24. Clerc J. P., Giraud G., Laugier J. M., Luck J., *M. Adv. Phys.* **1990**, *39*, 191–309.
25. McLachlan D. S., Blaszkiewicz M., Newnham R. E., *J. Am. Ceram. Soc.* **1990**, *73*, 2187–2203.
26. Stauffer D., Aharony A., *Perkolationstheorie: Eine Einführung*, Wiley-VCH: Weinheim, Germany, **1995**.
27. Sichel E.K., Gittleman J.I., Sheng P., *Carbon Black Polymer Composites*, edited by E. K. Sichel (Dekker, New York, **1982**), Chap. 2, p. 51.
28. Ezquerro T.A., Kulescza M., Baltá Calleja F.J., *Synth. Met.* **1991**, *41*, 915-920.
29. Connor M. T., Roy S., Ezquerro T. A., Baltá-Calleja F. J., *Phys. Rev. B* **1998**, *57*, 2286–2294.

CHAPTER V

Conclusions

The research activity of the present thesis work was dedicated to the preparation of nanostructured organic/inorganic hybrid and inorganic materials, by a novel synthetic strategy that combines the bottom-up approach of the sol-gel technique, which is versatile and cheap, and the property of block copolymers to form ordered nanostructures by self-assembly. These nanocomposites have been obtained as thin films and their morphological characterization has been performed over large macroscopic surfaces. The achievement of a long range order at nanometer scale over macroscopic surfaces has been fundamental not only from a point of view of the basic knowledge but also to enlarge the application field of these materials. In the literature examples of nanocomposite materials obtained with a synthetic approach analogous to the one discussed here have been reported. However, the results were not promising for applications due to the lack of nanostructural organization over a large area. This is due to the intrinsic difficulties to combine the sol-gel process protocol with the self-assembling ability of block copolymers. Therefore combining the nanostructuring ability of BCPs with the crosslinking reactions of metal oxide precursor via sol-gel technique is still a challenge.

Special attention has been devoted toward the set-up of methods to achieve well reproducible nanostructured metal oxide substrates, namely TiO₂ or Nb₂O₅ resorting to the combination of these two procedures: self-assembly from BCP and sol-gel technique.

Polystyrene-*b*-poly(ethylene oxide) (PS-*b*-PEO) with molecular mass 136 kDa and the volume fraction (ϕ) of PEO block equal to 23% was employed as *host* matrix. This ensured the formation of cylindrical nanostructures characterized by hexagonal arrangement of PEO cylinders oriented with axes perpendicular to the film surface inside the PS matrix.

The preparation method of the thin hybrid films has been devised by mixing a solution of the metal oxide precursor to the BCP solution and the successive spin coating. The spin-coating technique was employed in order to control the roughness and the thickness of the film tuning the spinning speed of the rotating plate.

The amphiphilic nature of the BCP allowed selective inclusion of the metal oxides, and its precursors inside the PEO cylindrical domains.

The dimensional analysis performed on FESEM, TEM and AFM images indicated that the increase of the inorganic content in the hydrophilic domains brought a progressive diminution of the diameter of the cylinders.

The so-obtained nanocomposites were then annealed at 600 °C at a rate of 2 °C min⁻¹ and were kept at that temperature for 4 hours to eliminate completely the organic matrix. An hexagonal crystalline array of TiO₂ or Nb₂O₅ nanoparticles was obtained reminiscent of the nanostructure of hybrid nanocomposites.

The size of the titania or niobia NPs and the coverage density of the substrate mimicked the dimensions of the PEO affine block before its removal.

Since NPs motifs are reminiscent of the long range order achieved by BCP alone, procedures to improve this order in the hexagonal packing of PEO cylinders have been attempted. The “solvent annealing” technique has been used to enhance the order of the neat and hybrid samples.

According to the literature the relative humidity (R.H.%) and the development of a fast procedure are the key parameters for the achievement of an innovative and effective solvent annealing process that was able to reduce the morphological defects at long range scale. Many efforts have been done in this study to develop a novel single step method for film deposition/solvent annealing process that could work properly on both neat PS-*b*-PEO copolymer and the hybrid nanocomposites.

The novel methodology of Rapid Solvent Annealing (*RSA*) developed here, that consisted in the introduction of a flow of solvent vapors directly into the sealed spin-coater chamber, permitted to cover a great range of values of relative humidity in a few seconds and demonstrated to work efficiently both on neat and hybrid thin films.

The Voronoi constructions (its algorithm has been devised expressly for this study) have been employed to quantify the amount of the improvement of long-range order.

Lastly the hybrid and heat-treated thin films containing TiO₂ NPs have been tested for the soot detection by measurements of conductivity.

The current problematic of the emission of soot nanoparticles in the urban areas represents a challenge for the scientific community that is developing new detection methods.

The most promising are conductometric soot sensors. Their main advantages are the simple principle, low costs, and especially their small dimension.

In this study the titania thin films have been employed as conductometric sensors and demonstrated to work properly for the detection of carbonaceous materials (PM 0.1 and 0.01). These systems are very promising and their development will bring to the detection of smaller soot NPs meeting the requirements of the last directives of the European Parliament that only recently has realized how hazardous to the health are PM 2.5, PM 0.1 and PM 0.01.

Appendices

A.1 Histogram of depth values of an hybrid heat-treated sample with 10 mol% TTIP

The average values of the heights of TiO₂ nanostalagmites (~ 11 nm of Figure 1a) of a hybrid SEO system heat treated at 600 °C containing 10 mol% TTIP are reported in Figure 1b.

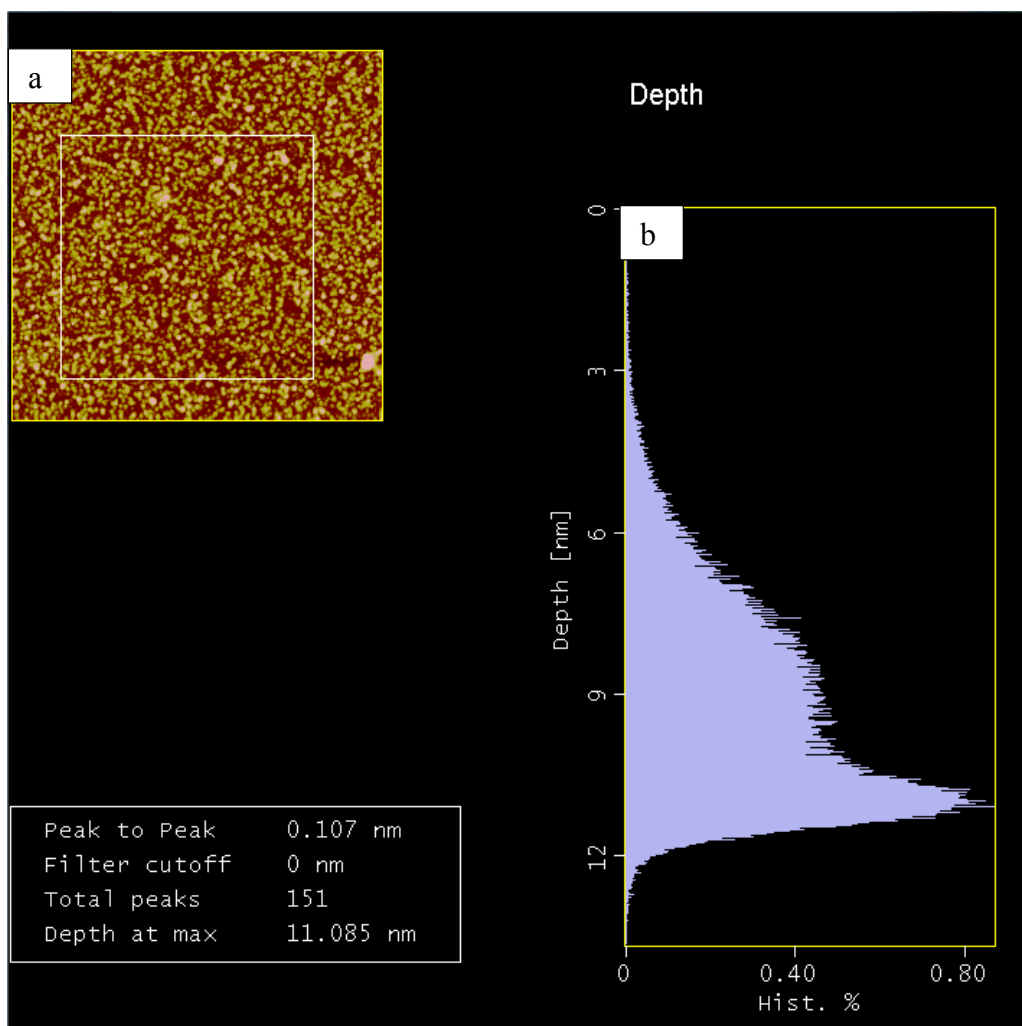


Figure 1: AFM image ($2\mu\text{m} \times 2\mu\text{m}$) of the heat-treated (600°C at a rate of 2°C min^{-1} for 4h) hybrid sample loaded with 10 mol% of TiO₂ precursor (a) and the histogram of the values of depth (b) obtained on the same image. AFM image was collected using a Digital Instruments Nanoscope IIIA in collaboration with Dr. Giovanni Ausanio at the Physics Laboratories of the University of Naples “Federico II”.

A.2 FESEM images of thin films of neat SEO solvent annealed directly in the spin-coater chamber at different values of R.H.%

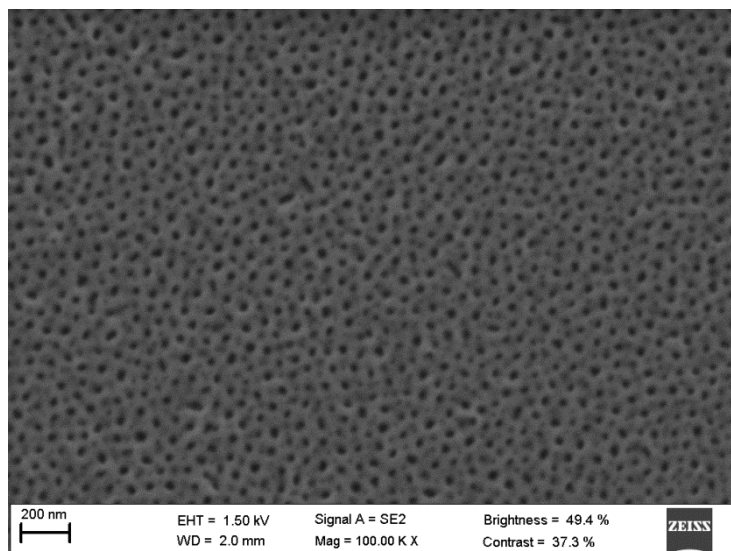


Figure 2: FESEM images of thin films of neat SEO obtained by spin-coating at 2500 rpm at room temperature after toluene annealing (42 R.H.%) in the sealed spin-coater chamber.

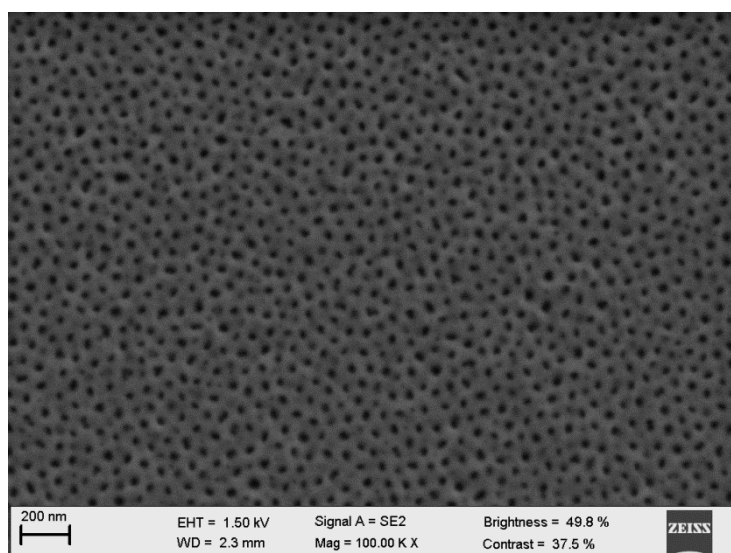


Figure 3: FESEM images of thin films of neat SEO obtained by spin-coating at 2500 rpm at room temperature after toluene annealing (46 R.H.%) in the sealed spin-coater chamber.

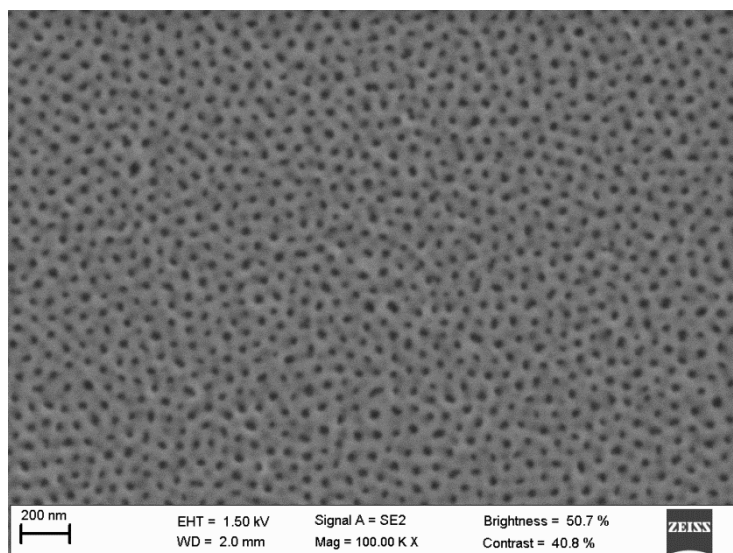


Figure 4: FESEM images of thin films of neat SEO obtained by spin-coating at 2500 rpm at room temperature after water/toluene annealing (41 R.H.%) in the sealed spin-coater chamber.

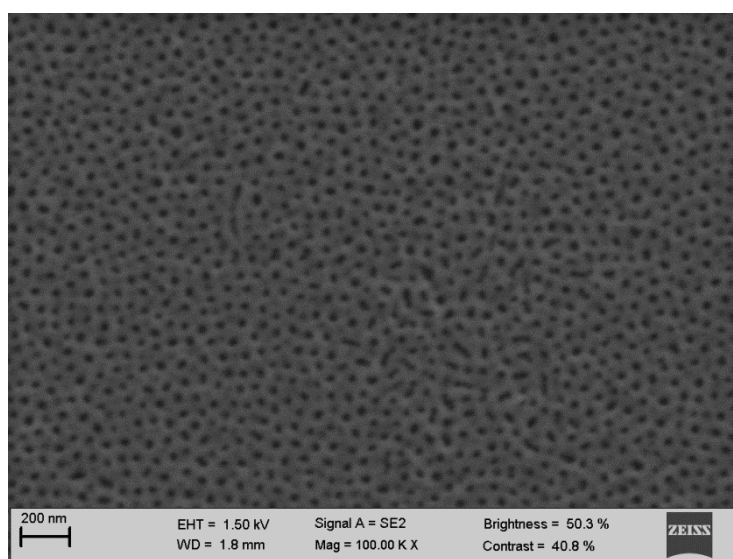


Figure 5: FESEM images of thin films of neat SEO obtained by spin-coating at 2500 rpm at room temperature after water/toluene annealing (52 R.H.%) in the sealed spin-coater chamber.

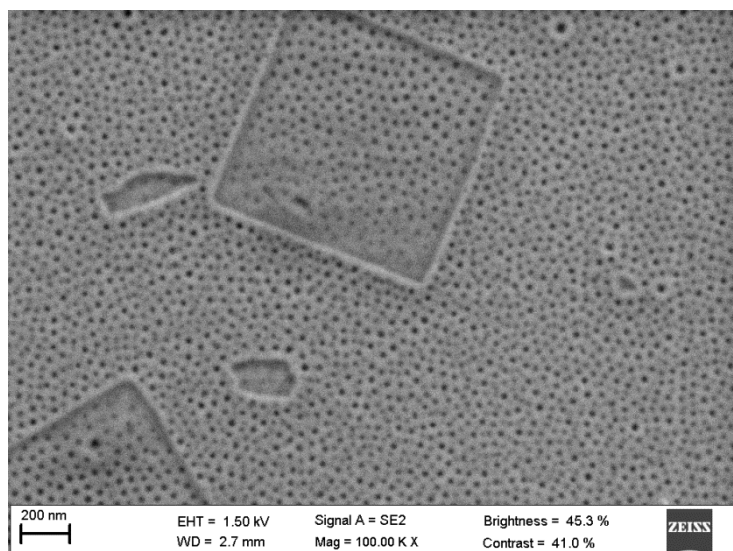


Figure 6: FESEM images of thin films of neat SEO obtained by spin-coating at 2500 rpm at room temperature after water annealing (47 R.H.%) in the sealed spin-coater chamber.

A.3 FESEM images of thin films of neat SEO, hybrid SEO/TTIP samples obtained by *Rapid Solvent Annealing* performed in the sealed chamber at different values of R.H.% during spin-coating

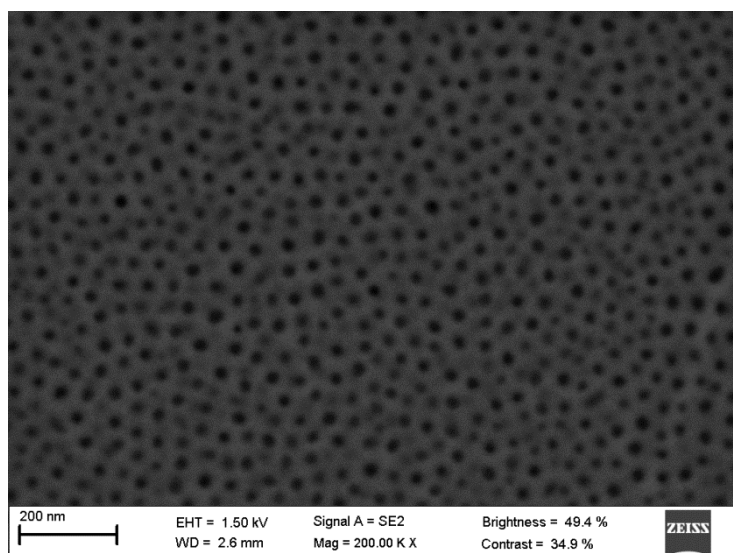


Figure 7: FESEM images of thin films of neat SEO obtained by spin-coating at 2500 rpm simultaneously to acetone annealing (8 R.H.%) at room temperature in the sealed spin-coater chamber.

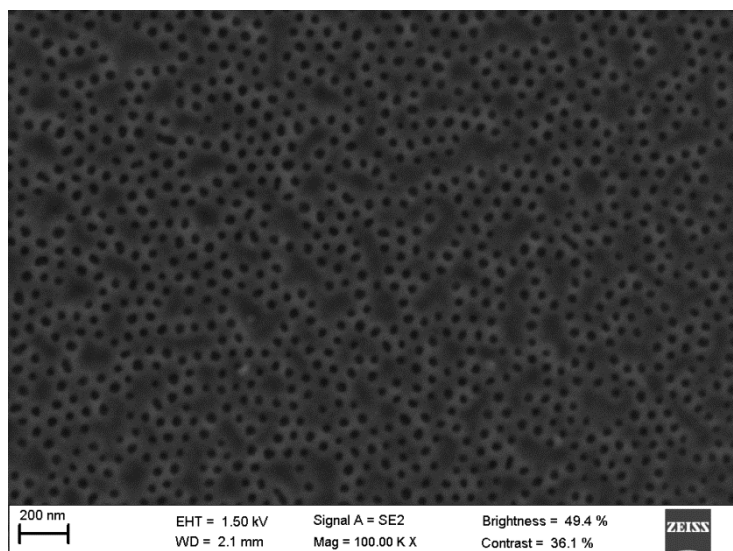


Figure 8: FESEM images of thin films of neat SEO obtained by spin-coating at 2500 rpm simultaneously to toluene annealing (17 R.H.%) at room temperature in the sealed spin-coater chamber.

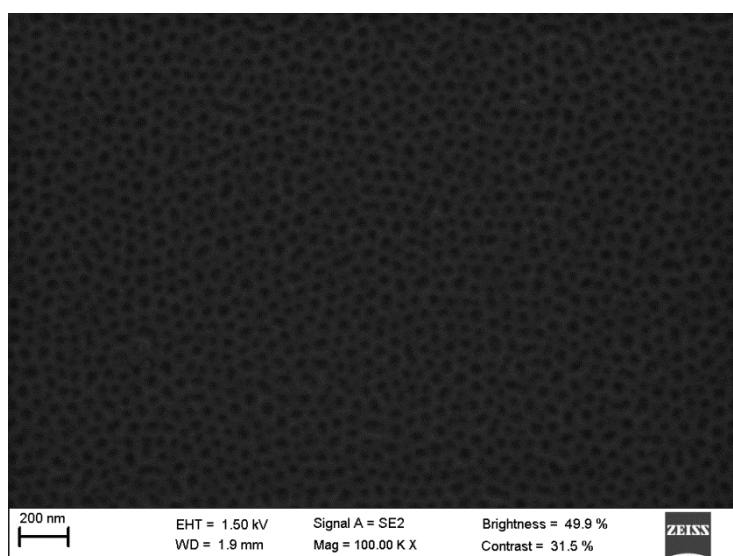


Figure 9: FESEM images of thin films obtained by spin coating a SEO toluene solution containing 40 mol% TTIP at 2500 rpm simultaneously to water/toluene annealing (38.5 R.H.%) at room temperature in the sealed spin-coater chamber.

A.4 FESEM image of thin films of hybrid SEO/TTIP samples obtained by *Rapid Solvent Annealing* performed in the sealed chamber at different values of R.H.% during spin-coating and then heat treated at 600 °C.

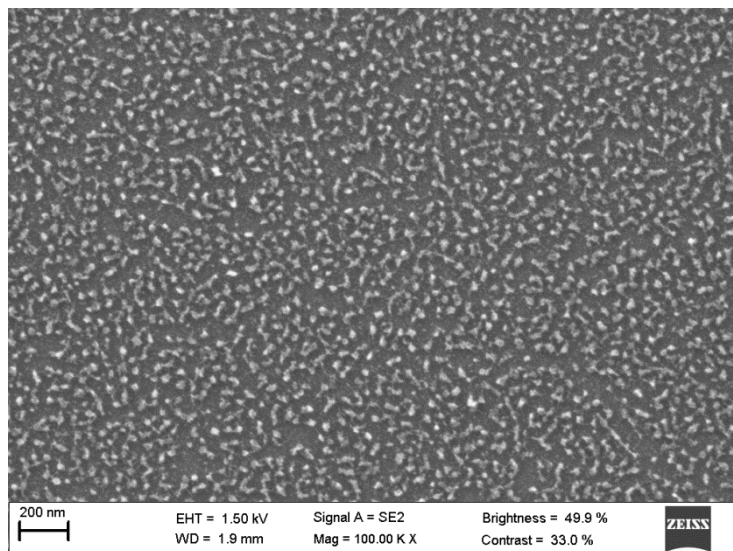


Figure 10: FESEM images of thin films obtained by heat treatment (at 600 °C for 4 h) after spin coating a SEO toluene solution containing 40 mol% TTIP at 2500 rpm simultaneously to water/toluene annealing (38.5 R.H.%) at room temperature in the sealed spin-coater chamber.